Development of High-efficiency and Sustainable Back Contact Solar Cells

Chen, N.

DOI
10.4233/uuid:28cb2308-d63e-44ec-b785-326c0c4d12c5

Publication date
2023

Document Version
Final published version

Citation (APA)
Chen, N. (2023). *Development of High-efficiency and Sustainable Back Contact Solar Cells*. [Dissertation (TU Delft), Delft University of Technology]. https://doi.org/10.4233/uuid:28cb2308-d63e-44ec-b785-326c0c4d12c5

Development of High-efficiency and Sustainable Back Contact Solar Cells

Ning CHEN

陈宁

Development of High-efficiency and Sustainable Back Contact Solar Cells

Dissertation

for the purpose of obtaining the degree of doctor
at Delft University of Technology
by the authority of the Rector Magnificus prof.dr.ir. T.H.J.J. van der Hagen
chair of the Board for Doctorates
to be defended publicly on
Friday 8 September 2023 at 12:30 o'clock

by

Ning CHEN

Master of Engineering in Electronics and Communication Engineering,
Shanghai Jiao Tong University, China
born in Yulin (Shaanxi), China

This dissertation has been approved by the promotors.

Composition of the doctoral committee:

Rector Magnificus	chairperson
Prof.dr.ir. O. Isabella	Delft University of Technology, promotor
Prof.dr. M. Zeman	Delft University of Technology, promotor
Independent member:	
Prof.dr. I.M.F. Gordon	Delft University of Technology / IMEC, Belgium
Prof.dr. R. Schlatmann	HTW Berlin, Germany
Prof.dr.ir. A.H.M. Smets	Delft University of Technology
Dr. D. Muñoz	INES, France
Prof.dr. P. Palensky	Delft University of Technology, reserve member
Other members:	
Dr. V. D. Mihailetchi	ISC Konstanz, Germany

Keywords: photovoltaic, silicon solar cells, back contact, cut losses, edge recombination, copper metallization

Printed by: Ipskamp Printing

Front & Back: Designed by N. Chen, a prototype of bifacial back contact solar module with copper printed half-cut cells from this research.

ISBN: 978-94-6384-462-8

An electronic version of this dissertation is available at
`http://repository.tudelft.nl/`.

Contents

Summary

The issue of climate change, including global warming, poses a significant challenge to our planet. In response to this challenge, the Paris Agreement was signed, which aims to limit the rise in global temperatures to well below 2 °C and pursue efforts to limit it even further to 1.5 °C. Photovoltaic energy is the key to achieving this target.

This dissertation focuses on improving the efficiency and sustainability of interdigitated back contact (IBC) solar cells. A special emphasis is also placed on cost and reliability. IBC cells and modules utilized in this study are based on ZEBRA technologies, which were developed at ISC Konstanz and implemented using processes and equipment that are comparable to those employed in conventional solar cells, such as Al-BSF and PERC. A detailed discussion of the process and history can be found in Chapter 2.

To improve the efficiency of back contact solar cells and modules, this thesis focus on the reduction of edge recombination. In advanced module fabrication, cut cells are used to reduce series losses and increase module efficiency. However, the cutting process may also introduce new cut edges and result in power losses. The edge recombination losses become significant when cells are cut into smaller pieces to be assembled into modules. The losses under low light intensity are reduced to an even greater extent. IBC solar cells can be cut through different doped regions to reduce losses. Through simulations and experimental measurements, it is found that the cut losses can be reduced by cutting through the back surface field rather than through the emitter. In the case of a 23% cell is cut into 1/3 pieces, the efficiency can be increased by 1.2%$_{\text{rel}}$ under standard 1-sun testing conditions, compared to cutting through the emitter. Under low light intensity of 0.25-sun, the improvement is around 2.4%$_{\text{rel}}$. Results are detailed in Chapter 4, which also includes analysis of additional losses due to laser damage using pFF analysis, and confirmation of FF losses through Suns–V_{oc} and PL measurements.

Furthermore, the edge recombination can be reduced by an additional passivation step. Chapter 5 explores the use of Nafion polymer for edge passivation in n-type IBC solar cells to reduce edge recombination. The effectiveness of different edge types and cutting techniques are evaluated, with thermal laser separation (TLS) or mechanical cleaving found to enable good repassivation. On 1/4-cut M2 size (156.75 mm × 156.75 mm) IBC cells with two emitter edges, efficiency is improved by over 0.3%$_{\text{abs}}$, but not with BSF edges. Real-world stability is evaluated through industry standard testing of 1000 hours under damp heat conditions (85 °C, 85% relative humidity). The tests reveal stable repassivation in EVA encapsulants but not in POE.

The second part of this thesis is dedicated to addressing the challenge of improving sustainability in solar cells. As solar energy grows into a major energy source, sustainability has become a challenge. One of the key concerns in this regard is the high usage of silver in silicon solar cells, which has led researchers to explore the use of copper metallization as a more sustainable and cost-effective alternative. In this study, a screen printed copper paste was used as a conductive layer for IBC cells to replace the majority of silver usage. The cells were designed and printed using two layers - a thin fire-through silver paste was printed first, followed by copper paste applied as fingers and busbars. Remarkably, the copper paste printed cells achieved the same level of efficiency as the reference fully silver paste printed cells, with both groups achieving average efficiencies of 23%. The copper paste replaced most of the silver usage in the cells, leading to a silver consumption of only 4.5 mg W^{-1}. In addition to efficiency improvements, reliability and stability were examined. The damp heat stress test (85 °C, 85% relative humidity) of 1000 hours showed no degradation in V_{oc} and pFF. Moreover, under more severe test conditions - a thermal stress test under 200 °C for 1000 hours - the V_{oc} of copper cells only degraded by $0.5\%_{\mathrm{rel}}$, and pFF only by $0.3\%_{\mathrm{abs}}$. The results convincingly demonstrate that Cu diffusion into Si bulk from a screen printed paste can be prevented, and that the screen printed copper paste has the potential to replace most of the silver used for metallization in industrial cell concepts. These findings are presented in Chapter 6.

In addition to focusing on improving efficiency and sustainability, another significant aspect of this study is the rigorous testing of reliability. The experimental and characterization details are explained in Chapter 3.

Overall, this thesis contributes to the development of sustainable and efficient back contact solar cells in two approaches. The first approach involved improving the efficiency of cut cells and modules by addressing cut edge recombination. Through cutting through the BSF regions of IBC cells, cut losses were reduced and this approach has already been implemented in the production line. Edge losses were further addressed by studying edge passivation using Nafion polymer, which resulted in efficiency gain, and stability was proven in EVA encapsulate. This finding has the potential for industrial application with further engineering work. The second approach focused on improving cost and sustainability through the use of copper metallization. Screen printing using copper paste was investigated as a simple solution, leading to the production of high-efficiency back contact solar cells with a silver usage of only 4.5 mg W^{-1}. In addition, the cells showed excellent reliability results. The screen printed copper process demonstrated promising potential for industrial application.

Samenvatting

De huidige klimaatverandering, waaronder de opwarming van de aarde, vormt een significante uitdaging voor onze planeet. Als antwoord op deze uitdaging, is het 'Akkoord van Parijs' getekend. Het akkoord heeft als doel om de wereldwijde temperatuurstijging tot onder de 2 °C te limiteren en streeft om het zelfs nog verder te limiteren tot 1,5 °C. Photovoltaische energie is de manier om dit doel te bereiken.

Dit proefschrift richt zich op het verbeteren van de efficiëntie en duurzaamheid van interdigitated back contact (IBC) zonnecellen. Een extra na nadruk is gelegd op kosten en betrouwbaarheid. De in dit onderzoek gebruikte IBC cellen en modules zijn gebaseerd op ZEBRA technologieën, deze zijn ontwikkeld bij ISC Konstanz en geïmplementeerd met behulp van processen en apparatuur die vergelijkbaar zijn met die van conventionele zonnecellen, zoals Al-BSF en PERC. Een gedetailleerde (beschrijving) discussie van het proces en de geschiedenis in te vinden in hoofdstuk 2.

Om de efficiëntie van de back contact zonnecellen en -modules te verbeteren, richt dit proefschrift zich op het reduceren van randrecombinatie. Bij geadvanceerde module ontwikkeling worden gesneden cellen gebruikt om serieverliezen te verminderen en efficiëntie van de module te verhogen. Het snijproces kan echter ook weer nieuwe snijranden introduceren en dit leidt tot vermogensverliezen. De randrecombinatie wordt significant als cellen in kleinere stukken worden gesneden, om tot modules te worden geassembleerd. Bij een lage lichtintesiteit worden de verliezen nog verder verminderd. IBC zonnecellen kunnen door verschillende gedoteerde delen gesneden worden om verliezen te verminderen. Uit simulaties en experimentele metingen, is gebleken dat de snijverliezen beter gereduceerd kunnen worden door te snijden door het back surface field dan door de emitter. In geval van een cel van 23% efficiëntie, gesneden door het back surface field in 1/3 stukken, kan de efficiëntie met 1,2%$_{\text{rel}}$ verhoogd worden in standaard test condities met 1 zon, ten opzichte van een door de emitter gesneden cel. Bij een lage lichtintensiteit van 0,25 zon is de verbetering ongeveer 2,4%$_{\text{rel}}$. De resultaten worden gedetailleerd beschreven in hoofdstuk 4, daarnaast bevat het hoofdstuk een analyse van bijkomende verliezen door laserschade met behulp van een pFF-analyse, en bevestiging van FF-verliezen door Suns–V_{oc} en PL-metingen.

Verder kan de randrecombinatie nog verminderd worden door een extra passiveringsstap. Hoofdstuk 5 onderzoekt het gebruik van Nafion polymeer als randpassivering om de randrecombinatie in n-type IBC zonnecellen te verminderen. De effectiviteit van verschillende rand types en snij technieken wordt geevalueerd, waarbij thermische laserscheiding (TLS) of mechanisch klieven goede repassivatie mogelijk blijken te maken. Op 1/4-gesneden M2-formaat (156,75 mm x 156,75 mm) IBC cellen met twee emitterranden, wordt de efficiëntie met meer dan 0,3% verbeterd, maar niet met BSF-randen. De werkelijke stabiliteit is geëvalueerd aan de hand van industriële standaardtests van 1000 uur onder vochtige omstandigheden (85 °C, 85% relatieve vochtigheid). De tests tonen een stabiele repassivatie in EVA-kapsels, maar niet in POE.

Het tweede deel van dit proefschrift is gewijd aan de uitdaging om de duurzaamheid van zonnecellen te verbeteren. Nu zonne-energie uitgroeit tot een belangrijke energiebron, is duurzaamheid een uitdaging geworden. Een van de belangrijkste zorgen is het hoge gebruik van zilver in silicium zonnecellen. Om deze reden hebben onderzoekers het gebruik van kopermetallisatie onderzocht, als een duurzamer en kosteneffectiever alternatief. In deze studie werd een gezeefdrukte koperpasta gebruikt, als geleidende laag voor IBC cellen om het merendeel van het zilvergebruik te vervangen. De cellen werden ontworpen en gedrukt met twee lagen. Eerst werd een dunne, doorzichtige zilverpasta gedrukt, gevolgd door koperpasta die als vingers en busbars werd aangebracht. Opmerkelijk genoeg behaalden de met koperpasta bedrukte cellen hetzelfde rendement als de volledig met zilverpasta bedrukte referentiecellen, waarbij beide groepen een gemiddeld rendement van 23% behaalden. De koperpasta verving het grootste deel van het zilvergebruik in de cellen, wat leidde tot een zilververbruik van slechts 4,5 mg W^{-1}. Naast efficiëntieverbeteringen werden ook de betrouwbaarheid en stabiliteit onderzocht. De test met vochtige hitte (85 °C, 85% relatieve vochtigheid) van 1000 uur toonde geen degradatie van de V_{oc} en de pFF. Onder strengere testomstandigheden - een thermische stresstest bij 200 °C gedurende 1000 uur - verminderde de V_{oc} van de kopercellen slechts met 0,5$\%_{\text{rel}}$ en de pFF slechts met 0,3$\%_{\text{abs}}$. De resultaten tonen overtuigend aan dat koperdiffusie in Si bulk van een zeefdrukpasta kan worden voorkomen, en dat de zeefdruk koperpasta het potentieel heeft om het grootste deel van het zilver dat wordt gebruikt voor metallisatie in industriële celconcepten te vervangen. Deze bevindingen worden gepresenteerd in hoofdstuk 6.

Naast aandacht voor verbetering van de efficiëntie en duurzaamheid is een ander belangrijk aspect van deze studie het rigoureus testen van de betrouwbaarheid. De experimentele en karakteriseringsdetails worden toegelicht in hoofdstuk 3.

In het algemeen draagt dit proefschrift bij aan de ontwikkeling van duurzame en efficiënte zonnecellen met backcontact in twee benaderingen. De eerste benadering betrof het verbeteren van de efficiëntie van doorgesneden cellen en modules, door het aanpakken van recombinatie aan de snijrand. Door het doorsnijden van de BSF-gebieden van IBC-cellen werden snijverliezen verminderd en deze aanpak is al geïmplementeerd in de productielijn. Randverliezen werden verder aangepakt door onderzoek naar randpassivering met behulp van Nafion-polymeer, wat resulteerde in efficiëntiewinst, en de stabiliteit werd bewezen in EVA-kapsels. Deze bevinding heeft potentie voor industriële toepassing met verdere technische werkzaamheden. De tweede benadering was gericht op het verbeteren van de kosten en de duurzaamheid door het gebruik van kopermetallisatie. Zeefdrukken met koperpasta werd onderzocht als een eenvoudige oplossing, die leidde tot de productie van zonnecellen met hoog rendement en een zilververbruik van slechts 4,5 mg W^{-1}. Bovendien vertoonden de cellen uitstekende betrouwbaarheidsresultaten. Het gezeefdrukte koperproces toonde een veelbelovend potentieel voor industriële toepassing.

Nomenclature

Abbreviations

a-Si	Amorphous silicon
Ag	Silver
Al	Aluminium
ALD	Atomic layer deposition
APCVD	Atmospheric pressure chemical vapor deposition
AR	Aspect ratio
BB	Busbar
BSF	Back surface field
BSG	Borosilicate glass
c-Si	Crystalline silicon
COO	Cost of ownership
CTM	Cell-to-module
Cu	Copper
Cz-Si	Czochralski silicon
DH	Damp heat
ECA	Electrically conductive adhesive
EL	Electroluminescence
EVA	Ethylene vinyl acetate
FSF	Front surface field
GW	Gigawatt
i-PERC	Industrial passivated emitter and rear contact
IBC	Interdigitated back contact
ITRPV	International technology roadmap for photovoltaic

IV	Current voltage
L&C	Laser and cleave
LCOE	Levelized cost of electricity
mono-Si	Monocrystalline silicon
PCB	Printed circuit board
PECVD	Plasma-enhanced chemical vapor deposition
PERC	Passivated emitter and rear cell
PL	Photoluminescence
POE	Polyolefin elastomer
PSG	Phosphosilicate glass
QE	Quantum efficiency
SDE	Saw damage etching
SHJ	Silicon heterojunction
SSE	Single side etching
TC	Thermal cycling
TLS	Thermal laser separation
TOPCon	Tunnel oxide passivating contact
TW	Terawatt

Symbols

η	Efficiency
E_a	Activation energy
FF	Fill factor
J_{sc}	Short-circuit current density
pFF	Pseudo fill factor
V_{oc}	Open-circuit voltage

1

Introduction

"This Agreement, in enhancing the implementation of the Convention, including its objective, aims to strengthen the global response to the threat of climate change, in the context of sustainable development and efforts to eradicate poverty, including by: (a) Holding the increase in the global average temperature to well below 2 ° C above pre-industrial levels and pursuing efforts to limit the temperature increase to 1.5 ° C above pre-industrial levels, recognizing that this would significantly reduce the risks and impacts of climate change..."

— Paris Agreement, Article 2, 2015

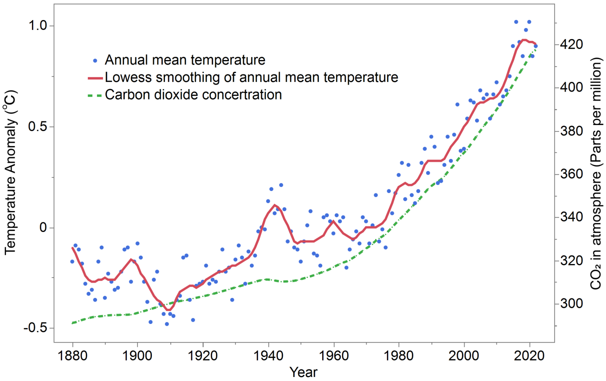

Figure 1.1: Changes in global temperature and CO_2 levels between 1880 and 2022. The mean temperature for each year is represented by the blue points, while the red line indicates locally weighted scatterplot (Lowess) smoothing. The CO_2 data is averaged on a yearly basis shown in green dashed lines. Temperature data source: NASA's Goddard Institute for Space Studies (GISS) [3]. CO_2 Data source (1880-1958): NASA/GISS [3]. CO_2 data source (1959-2022): NOAA (National Oceanic and Atmospheric Administration, USA) [4].

1.1. Climate change and Paris Agreement

In this century, climate change poses a major challenge to humanity. Climate change was identified through various indicators, including concentrations of CO_2, global temperatures, sea levels, arctic sea ice, ice sheets, and glaciers [1]. At first, there was optimism that climate change could be attributed to natural fluctuations. However, scientific evidence has since confirmed the reality of climate change and global warming [2].

In 2015, 196 parties to the United Nations agreed on the Paris Agreement in order to control climate change. As stated at the beginning of this chapter, one of the main targets is: “Holding the increase in the global average temperature to well below 2 °C above pre-industrial levels and pursuing efforts to limit the temperature increase to 1.5 °C above pre-industrial levels, recognizing that this would significantly reduce the risks and impacts of climate change”.

Despite increased awareness and efforts to address climate change, it remains an ongoing issue. As illustrated in Figure 1.1, the global temperature has increased by approximately 1.0 °C since pre-industrial times, as of 2022. Moreover, current measurements of atmospheric carbon dioxide (CO_2) levels, taken at the Mauna Loa Observatory in Hawaii, indicate concentrations of around 420 ppm.

The most recent Emission Gap Report (2022) indicates that time is running out for us to achieve our target of limiting global temperature increase to 1.5 °C, and that the "climate crisis calls for rapid transformation of societies" [5]. To meet the target, rapid, deep, and sustained reduction actions are needed. For example, the Intergovernmental Panel on Climate Change (IPCC) recommends that global greenhouse gas emissions should peak before 2025 (at the latest) and then be reduced by 43% by 2030, while methane emissions should be reduced by approximately a third [6].

The energy supply sector is the primary source of global greenhouse gas emissions, accounting for approximately 35% of emissions worldwide (data from 2010) [7]. To re-

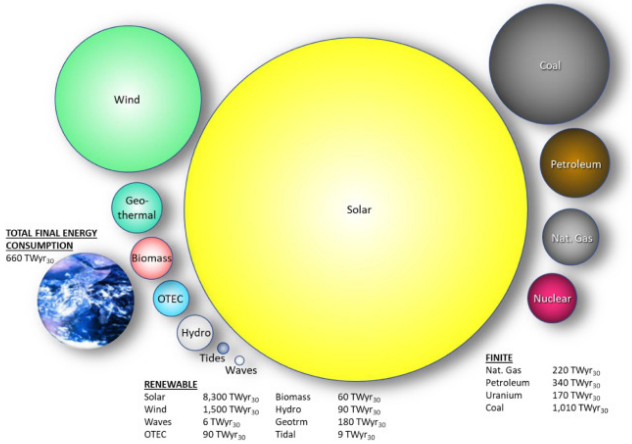

Figure 1.2: Assured energy reserves for both finite and renewable resources for the next 30 years; the earth image represent the energy demands over the same period. Reproduced with permission [9]. Copyright Elsevier (2022).

duce greenhouse gas emissions, it is essential to switch to decarbonized energy sources. This can be achieved by increasing the share of zero carbon energy, phasing out unabated coal and gas production, improving grids, storage, and electricity management, and ensuring reliable access to energy [5].

1.2. PV is the solution

Fortunately, solar energy has the potential to meet global energy requirements. Solar energy can be utilized for various applications, including generating electricity through photovoltaic (PV) cells and heating water or air for industrial and residential use. Of these applications, PV is especially promising, as it has the potential to contribute significantly to a fully renewable and environmentally friendly world, as stated in a study by Hoffmann et al. [8]. As illustrated in Figure 1.2, solar energy has the capacity to meet the global energy demand by 12 times over the next 30 years. In a scenario of full electrification, solar energy has the potential to satisfy global energy needs by a factor of 27 [9].

Solar energy is primarily utilized to generate electricity, which is achieved through the use of solar cells that convert sunlight directly into electrical energy via the photovoltaic effect. Figure 1.3 illustrates the fundamental principles of a solar cell [10]. In Figure 1.3(a), the absorption of a photon in a semiconductor is illustrated, which is the underlying physics behind the photovoltaic effect. E_C is the conduction band, E_V is the valence band, and E_G is the band gap. Bandbap is the energy difference between the valence band and conduction band, i.e., $E_G = E_C - E_V$. Absorption is the first step in the conversion of photon energy to electric energy. Semiconductors can absorb photons with an energy (E_{ph}) equal to or greater than the band gap energy (E_G), thereby generating electron-hole pairs. The energy from the absorbed photon is transferred to the electron-hole pairs as chemical energy. when $E_{ph} > E_G$, the rest of the energy is thermal-

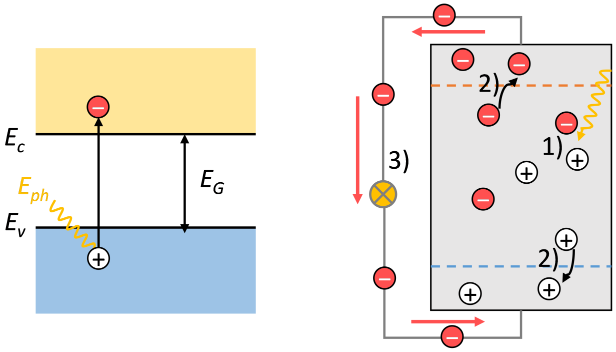

(a) (b)

Figure 1.3: Principles of solar cells. (a) Absorption of light in a band gap diagram. (b) A simple model of a solar cell. Figures adapted from [10].

ized.

The photovoltaic effect in solar cells involves a series of steps, illustrated in Figure 1.3(b). First, photon energy is converted into electrical energy through the generation of electron-hole pairs, as described previously. Second, the photogenerated charge carriers must be separated to prevent recombination. This is achieved using semipermeable membranes (typically made from n-type and p-type materials) on both sides of the absorber. The membranes allow electrons and holes to reach them before recombination occurs. Third, the photogenerated charge carriers are collected at the terminals of the cell (electrodes) and create a voltage. When an external circuit is connected, the carriers can flow through the circuit, resulting in the conversion of chemical energy into electrical energy.

After extensive research and development efforts by both laboratories and industry, photovoltaic technology has improved significantly and can now meet the criteria to serve as a major energy source. In its World Energy Outlook 2020 report, the International Energy Agency (IEA) referred to solar power as the new king of the global electricity market[11].

1.3. Opportunities and challenges for PV

To achieve the target of the Paris Agreement of limiting global warming to 2 °C, or even 1.5 °C, it is estimated that 70 TW of PV installations will be required by 2050. According to Verlinden et al. [12], PV production needs to increase rapidly and reach a stable annual production of 3 TW/year by 2035. However, as of 2022, the current capacity of PV is only 268 GW [13]. It is estimated that the capacity will reach 1 TW/year by 2030 and eventually reach multi-TW. During this transition, the "new king" faces both opportunities and challenges.

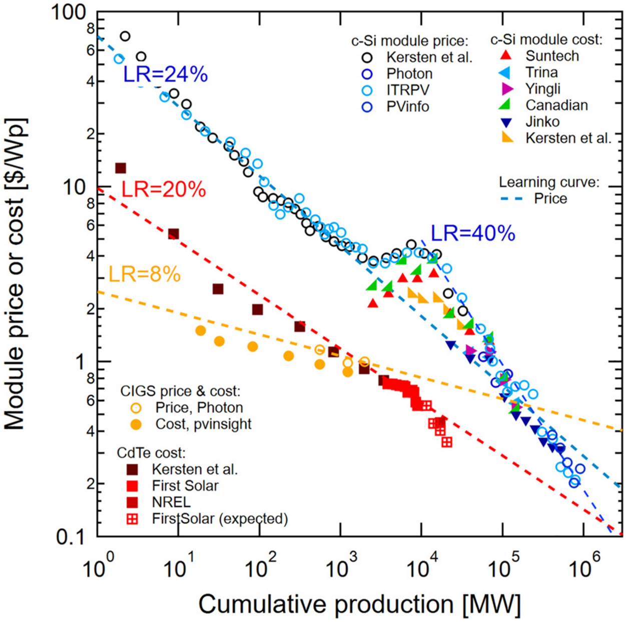

Figure 1.4: Module price versus cumulative production. The module cost has a learning rate of around 24%. In the last years (from 10GW production), the learning rate is 40% [16]. Reproduced with permission. Copyright John Wiley & Sons Ltd (2022).

1.3.1. Further improvements in efficiency, cost, and reliability

For solar cells and solar modules, power conversion efficiency, cost-effectiveness, and reliability are the most important factors.

The theoretical limit for single junction silicon solar cells is around 30%, while the current world record for silicon solar cells is 26.8% [14]. Despite this, the current efficiency of industrial cells is between 22-25%, with modules ranging from 20-23%. This suggests that there is still significant potential to improve the efficiency of both cells and modules.

The second important topic for solar cells and modules is cost. The price of solar modules is a crucial metric in this regard and, in recent years, it has experienced a substantial decrease. The average selling price of modules has decreased at an average learning rate (LR) of approximately 24. 1% according to ITRPV. In 2021, the module price was approximately 0.24 USD/watt peak (Wp) [15], and this cost continues to decrease with increasing production volume, as illustrated in Figure 1.4. As the production volume reaches multi-TW, module costs are expected to close to 0.1 USD/Wp with current LR around 40%.

The third topic is the reliability of solar modules. Solar modules, particularly silicon solar modules, have demonstrated their durability not only in the laboratory but also through extensive real-world usage. Presently, solar modules carry a product warranty ranging from 10 to 25 years, with a performance warranty of 25 to 30 years. The typical power degradation rate is between 0.5 and 1% per year, resulting in 80% of the original

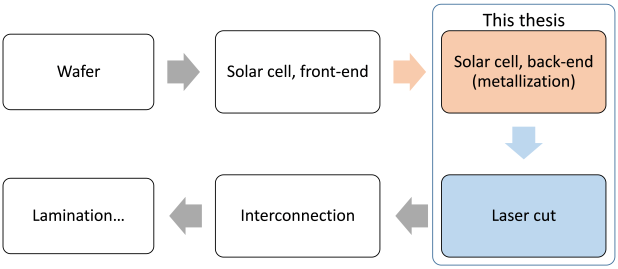

Figure 1.5: Research areas of this thesis, along with the positions of the processes of the solar cells and solar modules

power of the module remaining at the end of the performance warranty period. The long warranty makes solar modules one of the most reliable electrical products on the market today. When developing new technologies, reliability should be considered throughout the entire research and development process.

1.3.2. Last but not least, sustainability

As the transition to the TW era approaches, the sustainability of materials used in solar cells is a growing concern. Several materials, such as silicon, aluminum, copper, and silver, have been evaluated for their sustainability [12, 17–22]. Among them, silver has emerged as a major concern for silicon solar cells, not only because of its high cost but also because of its sustainability. To maintain the demand for silver within a sustainable range, a silver learning rate of 30% has been suggested by Hallam et al. [19]. The silver-less or silver-free metallization approaches are now hot topics in both research and industry.

1.4. Aim and outline of the thesis

The main goal of this thesis is to develop high-efficiency and sustainable back contact solar cells. The back contact technologies employed here are based on ISC Konstanz's ZEBRA IBC cells and modules. ZEBRA IBC solar cells have been under development for several years, showcasing remarkable features such as cost-effectiveness, high-efficiency, and reliability, and are currently being mass-produced. The efficiency and sustainability of these solar cells are significantly influenced by the metallization and cutting processes. The research focuses specifically on the metallization and laser cutting process, as shown in Figure 1.5, to further improve the efficiency and sustainability of the ZEBRA IBC cells / modules.

The first part of this thesis focuses on the significance of laser cutting processes and edge recombination. Laser cutting is employed between the stages of cell fabrication and module fabrication for ZEBRA cells. The laser cutting process significantly impacts edge recombination, which is known as cut losses, and ultimately affects the efficiency of both cells and modules. However, cut losses are often ignored because IV measurements are made on full cells and there are no IV measurements after laser cutting. Hence, improving the laser cutting process can boost overall efficiency by reducing cut and edge losses, leading to higher cell efficiency, and minimize cell-to-module losses, resulting in higher module efficiency.

The second part of this thesis focuses on the metallization process. Because of the use of precious metals, metallization directly impacts both the efficiency and cost of solar cells. In standard ZEBRA cells, silver is used for metallization. This thesis evaluates copper metallization for IBC cells in order to reduce costs and improve sustainability. Specifically, screen printing was selected because of its low cost and wide application in industry.

The following is an outline of this thesis:

- Chapter 1: Introduction to solar energy and its role in mitigating climate change.
- Chapter 2: The chapter summarizes the structures and process flows of industrial solar cells. It provides an overview of industrial silicon solar cell technologies, with a particular emphasis on the back contact cell and module technologies used in this thesis.
- Chapter 3: Experimental setup and characterization techniques used in this thesis, including laser cutting and various cell cutting techniques, screen printing technology, and characterization tools and methods.
- Chapter 4: Investigation and implementation of low cut-loss technologies for IBC solar cells. This chapter explores cut losses in IBC solar cells and proposes methods to reduce them.
- Chapter 5: Utilizing edge passivation to enhance solar cell and module efficiency. The use of Nafion polymer to passivate cut edges and improve cell and module efficiency is discussed in this chapter.
- Chapter 6: Enhancing the sustainability of IBC cells through copper paste metallization. This chapter evaluates the use of copper paste through screen printing, resulting in a notable decrease in silver usage.
- Chapter 7: Conclusions and future outlook of this thesis.

2

IBC cell and module technologies

Abstract

This chapter is divided into three parts. The first part provides a review of the progress made in industrial solar cells, with an emphasis on process flows and cell structures. These structures include Al-BSF (aluminum back surface field), PERC (passivated emitter and rear cell), and passivating contact solar cells. The technology of silicon solar cells has matured in the past two decades, and efficiency, cost, and reliability are now well established. A solid foundation has been laid for the next generation of solar cells as a result of these advances. The second part of the chapter summarizes IBC cell and module technologies that are relevant to this thesis. Current materials and equipment can be used to produce cost-effective, high-efficiency IBC cells and modules. In light of historical and recent trends, IBC cells with passivating contacts are likely to become the next and final dominant structure for single-junction solar cells prior to the advent of silicon tandems. Finally, the challenges and opportunities associated with IBC cells are discussed. One way to improve their efficiency is to reduce edge recombination losses. In addition, replacing silver with copper could increase the sustainability of IBC cells.

2.1. Silicon solar cell technologies, from past to now

Since the invention of the first practical solar cell in the 1950s in Bell Laboratories, silicon solar cells have become the most widely used technology in the photovoltaic industry. In the year 2021, 174 GW solar modules were installed, with crystalline silicon accounting for 95 percent of the market. Thin-film technologies contribute around 5%, including CdTe (mainly from First solar), amorphous silicon (a-Si) and copper indium gallium selenide (CIGS) solar cells [23].

In recent years, several new technologies have emerged, notably perovskites. There are, however, challenges with perovskite solar cells in terms of stability, industrialization, etc. The results of a recent study show that perovskite solar modules must have both high efficiency and long-term stability in order to compete with silicon modules. In 2030, a perovskite solar module should have an efficiency of 20% with a lifetime of at least 36 years, or an efficiency of 25% with a lifetime of at least 21 years; these numbers can be reduced if light and flexible substrates can be used [24]. Achieving high levels of efficiency and stability comparable to silicon solar cells in a relatively short period of time poses significant challenges for perovskite and other solar cell technologies. Therefor, it is expected that crystalline silicon cells will retain their position as the prevailing technology in the field of solar energy for the upcoming decade.

For photovoltaic cell technologies, the top four important indicators are:

- Power conversion efficiency of cells and modules. The efficiency of commercial monocrystalline silicon solar cells ranges from 22% to 25%, and the efficiency of module ranges from 20% to 23%.

- Reliability. It is common for silicon solar module suppliers to provide performance warranties of 15 to 25 years. Compared with their initial values, the modules still retain 80% to even 90% of their output power after 25 years. On-site and laboratory tests have demonstrated the long-term reliability and stability of silicon solar modules.

- Cost, which includes calculation from different perspectives. For example, the production related costs like cost of ownership (COO), capital expenditure (capex) which include the cost of building the factory and cost of equipment [25], and levelized cost of electricity (LCOE). Manufacturing companies are more concerned with COO and capex, while utility-scale companies are more concerned with LCOE.

- A final consideration is sustainability, especially when it comes to production of Terawatt (TW) yearly, as material availability becomes a major concern.

Silicon solar cell technology can meet the first three requirements and it can meet the last requirement to a considerable extent. This is why silicon solar cells dominate the market today. To meet the long-term sustainable requirement as a primary energy source, silicon solar cell technology must be further developed.

In this thesis, the focus is on both high-efficiency and sustainable back contact cell technology. The first topic is efficiency. For solar cells/modules, power conversion efficiency is the most important metric. This section discusses silicon solar cell technology from the past to the future, focusing on the cell structure and industrial process flow.

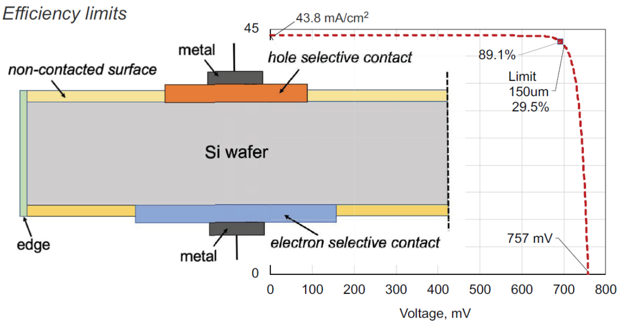

Figure 2.1: Schematic structure of a solar cell and the IV curve, from [30]. The efficiency of silicon solar cell is limited to around 29.5% with the parameters listed in the figure.

In silicon solar cells, the efficiency limits can be summarized by the Shockley–Queisser limit, also known as the detailed balance limit. For a single junction silicon solar cell, the efficiency is limited to 30% (energy gap of 1.1 eV) considering only radiative recombination loss [26]. By considering Auger combinations and incorporating various measurement data, the theoretical upper limit of efficiency has been determined to range from 29.4% to 29.8% [27–29]. An illustration of a schematic silicon solar structure with efficiency limits is shown in Figure 2.1[30]. This figure shows the main limits at different locations: 1) non-contacted surface passivation; 2) hole selective contact; 3) electron selective contact; 4) silicon wafer; and 5) edge. A real solar cell also suffers efficiency losses from imperfect light trapping (including metal shadowing) and resistance losses.

Since its invention, silicon solar cells have been developed by both industrial companies as well as research institutes and universities. Solar cells were pushed to their limits in terms of efficiency. Records for solar cell efficiency are listed in different charts or tables. The efficiency chart from National Renewable Energy Laboratory (NREL) [31], and efficiency table from journal *Progress in Photovoltaics* [32] are two famous examples. Currently, the highest silicon solar cell efficiency on a large-area wafer is 26.81% achieved by LONGi [14].

In mass production, solar cell efficiency is limited by many factors, such as cell structure, process flow, equipment availability, materials availability, and cost. The efficiency of production lines is much lower than the record efficiency, however, has been improved significantly in the last few years. The incredible advancements have been personally witnessed by the author of this thesis. Starting from my early days as a fresh graduate in 2008, when a multi-Si Al-BSF cell with an efficiency of approximately 15%, to the present year of 2023, where a mono-Si PERC cell boasting an efficiency of around 23%, and passivating contact cells have achieved efficiencies surpassing 24%. It is worth reviewing the evolution of cell technologies in the past, learning from them, and preparing for the next generation of solar cells.

The industrial silicon solar cell technologies are reviewed in the following paragraphs. These paragraphs summarize the past technology, Al-BSF; the current technology, PERC; and the passivating contact cells, including their structures and manufacturing processes.

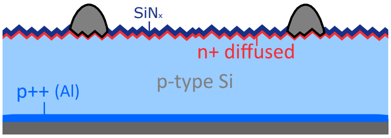

Figure 2.2: Schematic structure of an aluminium back surface field (Al-BSF) solar cell

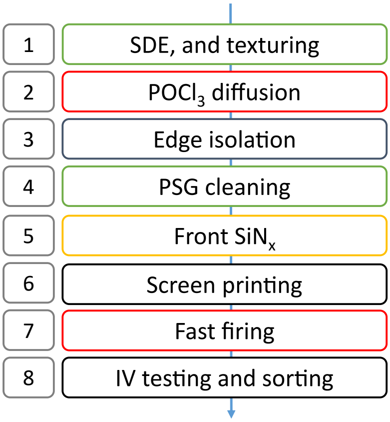

Figure 2.3: Process flow of an Al-BSF cell. Wet chemical processes are in green, high temperature processes are in red, vacuum processes are in yellow, and other processes are in black.

2.1.1. Al-BSF cells, 2000s to ~2016

Since early of 2000s, the industry has used aluminum back surface field (Al-BSF) structure in silicon solar cells to improve the rear passivation. Cells of this type are called Al-BSF cells. The schematic structure of an Al-BSF cell is shown in Figure 2.2. In the cell, p-type silicon wafers are used as substrates. The front side is textured, diffused by phosphorus (n+), and typically passivated with SiN$_x$. At the rear side, the wafer are printed with Al. The Al-BSF cells are benefit from the rear light reflecting, and p++ back surface field passivation which is formed by Al-Si alloy.

The Al-BSF solar cell was first described in 1973 [33], but with a complex/costly process flow. In industry, Al-BSF cells are made using a simple process. The process flow of Al-BSF solar cells is shown in Figure 2.3.

1. First, p-type wafers are etched to remove saw damage, and then textured in chemical solutions (to improve absorption of light). For mono-Si, alkaline solutions such as KOH or NaOH are used [34]; for multi-Si, acidic solutions such as the HF/HNO$_3$ mixture are used [35]. After texturing, a cleaning step is required. Laboratories use high-cost semiconductor cleaning processes such as RCA clean [36] and IMEC clean [37]. In industrial lines, HCl and HF are typically used for cleaning.
2. After texturing and cleaning, the wafers are diffused in a tube furnace using POCl$_3$ as diffusion source at 800 to 900 °C [38]. Other methods such as inline diffusion [39, 40], APCVD [41], and ion implantation [42] were evaluated, but were not became mainstream methods. POCl$_3$ diffusion remains the best option for n+ doping

considering the diffusion uniformity, throughput and cost.

3. Ideally, wafers should be diffused only on one side. In reality, diffusion occurs around the edges of the wafers and to the rear of the wafers. Edge isolation is required to separate the rear n+ from the front p+ emitter. As early as 2008, plasma etching or laser edge isolation was used in mass production (the latter involves laser edge isolation prior to IV testing)[43, 44]. Since 2008, wet chemical isolation has become widely used in industry, and it has proven to be more effective than dry etching, particularly when it can be performed in inline equipment and in conjunction with the following chemical cleaning process. Dannenberg et al. [45] have published a review article on the history of edge isolation.
4. After edge isolation, an HF cleaning step is performed to remove the phosphosilicate glass (PSG) of the wafers, with either inline or batch equipment. As mentioned, this step can be combined with the edge isolation step if inline wet chemical methods are used.
5. The next step is to deposit a SiN_x layer on the front. The SiN_x layer is used as both a passivation layer and an anti-reflection coating (ARC) layer by plasma enhanced chemical vapour deposition (PECVD) [46–48].
6. Metallization is achieved by screen printing. Wafers are printed with Ag paste on the rear side to serve as soldering pads, Al paste on the rear side to serve as Al-BSF, and Ag paste on the front side to serve as fingers and busbars. After each printing step, a low temperature (200 to 300 °C) drying is performed.
7. Final step is fast firing, also known as co-firing. Wafers are fired at a peak temperature of 750 to 850 °C in an inline firing furnace. As a result of the firing step, the front side Ag is contacted with n+ doped silicon[49], and the rear side Al diffused into silicon to form p+ Al-BSF [50]. After firing, the Ag and Al pastes also become highly conductive.
8. The final step is IV testing, which is usually conducted using a solar simulator to determine the electrical parameters of the final cells. A sorting process is also performed by solar cells based on their efficiency and current, in preparation for their manufacture as modules.

In comparison to other cell structures, Al-BSF cells have a simple process flow and relatively high efficiency, making them the dominant cell structure on the market. The development of Al-BSF cells was mainly focused on, 1) The development of materials, starting with silicon wafers and extending to materials used in the production of solar cells. From low lifetime multi-Si wafers to mono-like multi-Si wafers[51] to mono-Si wafers. Improvements have been made to the materials used in solar cells, particularly the silver paste. The Ag paste was improved to contact lightly doped emitter. Due to paste development, high sheet resistance emitters were successfully introduced to the cell process [52, 53]. In the texturing process, additives were added to improve the lifetime of the texturing bath, as well as to reduce the cleaning stains. 2) The development of equipment contributed to the introduction of new processes into mass-production. There were new processes and equipment introduced, such as inline chemical edge isolation. The printing of fine lines was improved by the use of screens, printers, and pastes in order to minimize the loss due to metal shading. A print-on-print technique was developed for printing fine fingers with a high aspect ratio [54]. Screen printing is summa-

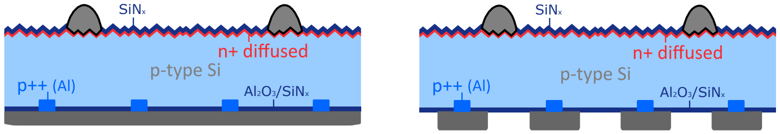

Figure 2.4: Schematic structures of passivated emitter rear contact (PERC) solar cell. Left: a monofacial PERC solar cell; right: a bifacial PERC solar cell.

rized in the next chapter. 3) The design and processing of solar cells were also improved. Texturing was developed for multi-Si wafers with low reflectance, e.g. black silicon [55]. Optimizing diffusion and passivation to improve the short wavelength response (or the blue response, from 300 nm to 500 nm). The selective emitter (SE) technology was developed, which utilized a heavily doped n++ region to ensure the contact between silicon and the n++ region, while using a lightly doped n+ region to improve the blue response [56]. In the later development of PERC cells, SE technology became a standard process. Busbar number was increased from 2 to 5, which reduced silver usage and improved cell efficiency (less lateral resistance loss). Multi-BB module technology has been developed to achieve high efficiency for both solar cells and modules [57].

Using Al-BSF cell structure, cell efficiency of 20.1% [58] and 20.3% [59] were reported. In a well optimized cell, the main recombination is the recombination from the Al-BSF at the rear [60]. The efficiency of Al-BSF solar cell is limited to around 20% in mass production. A better rear passivation is necessary to further increase solar cell efficiency, which leads to the deployment of PERC cells.

2.1.2. PERC, ~2016 to present (2023)

Since about 2016 to 2017, PERC solar cells have become a mainstay of the photovoltaic industry. The structure of a monofacial and a bifacial PERC cell are shown in Figure 2.4.

In addition to using p-type wafers, PERC solar cells also feature textured front sides and n+ diffusion on their front sides. The main difference between PERC cells and Al-BSF cells is that PERC cells are locally passivated on the rear side. Instead of full Al-BSF, local Al-BSF is used and the rest area is passivated by Al_2O_3 and capped with SiN_x. In mass production, the structure change boosts the efficiency from 20% to 23% (by the end of 2022). Another important feature of the PERC cells is the bifaciality, shown in Figure 2.4 (right). By screen printing Al fingers, instead of full area, the PERC cells become bifacial and are known as “PERC+” named by researchers of the ISFH [61]. The PERC+ became a game changer for bifacial PV applications [62, 63].

The PERC cell structure was invented in 1980s [64, 65], and it took over two decades for introducing PERC to mass production. A simple process flow is used in the current industrial PERC (i-PERC) cells. Figure 2.5 illustrates the process flow of i-PERC solar cells. Based on Al-BSF cells, the i-PERC's process flow is quite similar to that of Al-BSF. However, process recipe changes or equipment upgrades are needed. The i-PERC cell process includes following steps.

1. First, saw damage etching (SDE), texturing, and cleaning. Batch wet chemistry equipment became popular as mono-Si wafers were used in PERC instead of multi-Si wafers.

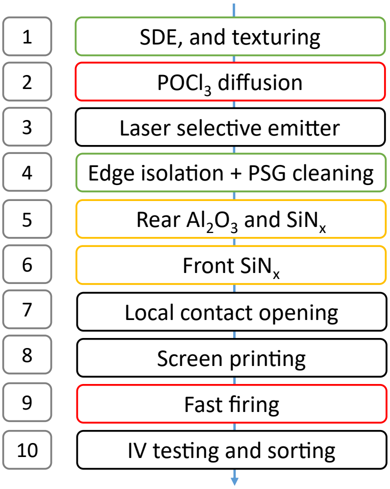

Figure 2.5: Process flow of an i-PERC cell. Wet chemical processes are in green, high temperature processes are in red, vacuum processes are in yellow, and other processes are in black.

2. The $POCl_3$ diffusion is used for PERC in the same manner as Al-BSF cells. The low-pressure $POCl_3$ diffusion (LP-$POCl_3$) furnace replaced the atmospheric pressure tools in the i-PERC era [66]. With LP-$POCl_3$ diffusion, uniformity of diffusion and throughput are improved. Further, the $POCl_3$ diffusion recipe has been changed since PSG is used for selective emitter doping by laser.
3. Selective emitter via laser doping has become a standard process in i-PERC cells. In Al-BSF cells, the process was optional, and various SE techniques were evaluated [56]. Laser doping won out over other SE techniques.
4. Edge isolation and PSG cleaning have been updated from Al-BSF era. Since the time of Al-BSF, chemical edge isolation has been the dominant technique. Additionally, single side etching (SSE) is now the standard process for PERC cells. Because the rear side passivation of PERC cells is sensitive to surface topography, process optimization and equipment improvement were required to achieve rear side polishing for PERC cells [67, 68].
5. The rear Al_2O_3 passivation is the new process for PERC cells. It is optional to perform an annealing or oxidation step before Al_2O_3 deposition, to enhance Al_2O_3/SiN_x passivation. Several materials and processes were evaluated prior to the success of Al_2O_3. The first PERC cell was passivated with thermally grown SiO_2 [69]. However, the thermally grown SiO_2 requires high processing temperatures (typically > 900 °C). The high temperatures can degrade the bulk minority carrier lifetime, especially when low grade multi-Si wafers were used at the beginning of PERC era. Alternatively, SiO_x can be grown at low temperatures. Centrotherm, for example, developed PECVD based SiO_x (SiNO) for i-PERC [70]. Another candidate is SiN_x, which is a mature technology that was developed during the development of Al-BSF cells. However, due to the high positive charge fixing, SiN_x passivation on the rear side is not perfect known as parasitic shunting [71].

Al_2O_3 was introduced for its excellent passivation on p+ doped silicon. The excellent surface passivisation due to the high negative charge fixing and low interface defect density [72]. Different methods can be used to deposit Al_2O_3, including: 1) Atomic layer deposition (ALD). The high speed ALD technology, also referred to as spatial ALD, was developed to meet the high throughput demands of the solar cell industry [73]. It was two Dutch companies - SoLayTec and Levitech - that contributed to the first commercialization of spatial ALD. 2) PECVD is another option, including direct and remote methods. Roth & Rau (acquired by Meyer Burger) is the primary provider of microwave-remote PECVD equipment [74]. There are several companies that provide direct PECVD equipment, including Centrothem. PECVD has the advantage that the following SiN_x can be deposited. This simplifies the production process. 3) Al_2O_3 can also be deposited by other methods. It includes, for example, APCVD [75], reactive ion sputtering [76], inductively coupled plasma (ICP) PECVD [77], Plasma-enhanced (PE) ALD [78], and even screen printing [79]. A recent study shows that PEALD is also being used in mass production [80].

6. The fabrication of SiN_x is usually carried out by PECVD. As with Al-BSF cells, PERC uses similar technology and equipment.
7. Lasers are used to open local contacts before screen printing. The laser becomes the most efficient method for ablation compared to other methods such as etching paste [81].
8. The screen printing process was optimized for PERC cells, including: 1) Better alignment for SE and double printing. As of 2018, alignment accuracy was between 10 and 15 μm ($\pm 3\sigma$). 2) Bifacial PERC cells can be easily made by changing full-area Al printing into Al fingers. 3) Multi-BB applications and interconnection processes are now in mass production.
9. Similar fast firing equipment is used as in the Al-BSF process, except for two differences. 1) Al paste firing recipe optimized for local Al-BSF formation. Many studies have been conducted on the local Al-BSF formation mechanism [82], and particularly on how to resolve the void issue [83]. 2) After firing, additional equipment was added. Hydrogenation tools using light or current injections was used to enhance the passivation of the cells [84]. By using a light injection at elevated temperature in an inline firing furnace, boron-oxygen related degradation (BO-LID) can be mitigated [85, 86].
10. IV and sorting are similar to Al-BSF cells, but with more advanced features. IV testing should be conducted with a long pulse duration (usually greater than 100 ms) or with more advanced methods to avoid the effects of capacitance on high-efficiency solar cells [87]. Additionally, electroluminescence (EL) was introduced in the production line for better quality control. EL was used in the labs for many years, [88] for detecting defects of contacting, passivation and wafer cracks etc. Until mass-production of PERC cells, EL became the industrial standard for solar cells. Offline EL inspection was used at first, then inline EL which integrated with IV testing [89]. In addition, the finished cells are subjected to an automatic color sorting process performed by cameras.

In summary, i-PERC is derived from Al-BSF cells in terms of its process and struc-

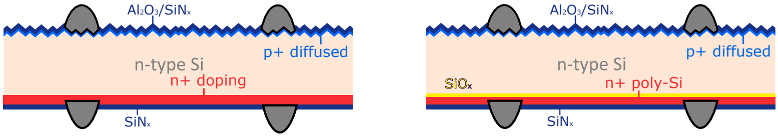

Figure 2.6: Schematic structures of an n-PERT (left) and an i-TOPCon solar cell (right).

ture. As i-PERC can be manufactured using most of the same equipment and processes as Al-BSF cells, this ensures a smooth and cost-effective transition. In addition, many developments were made to boost the efficiency of PERC cells. As a part of the transition, the silicon wafer was also changed from multi-Si to mono-Si. The efficiency gain between Al-BSF and PERC cells is greater for mono-Si wafers than for multi-Si wafers. Mono-Si wafers and PERC technology are mutually beneficial from the transition.

As a result of its advanced passivation technique as well as its simple and low-cost process flow, PERC has won the PV market. By 2022, the efficiency of PERC cells is around 23%, and the efficiency of PERC modules is 20% to 21%. In addition, PERC cells can be bifacial at no extra cost (if not at a lower cost). At the module level, PERC modules have a bifaciality of approximately 70%. In an optimized installation, power gain can be as high as 30% [62].

2.1.3. Passivating contact cells

The surface passivation of PERC cells is excellent, except for the metal contact region. In order to further enhance efficiency, the metal contact area needs to be well passivated with low contact resistance. Currently, passivating contact cells are becoming more popular and gaining market share, and this technology is expected to dominate the market in the near future. There are two types of cells used in mass production, namely TOPCon (Tunnel Oxide Passivated Contact) cells using doped polysilicon and SHJ (Silicon heterojunction) cells using doped amorphous silicon for charge carrier selection. Passivating contact cells using doped polysilicon have different names, such as POLO from ISFH, TOPCon from Fraunhofer ISE, monoPoly from SERIS, and TOUCAN from ISC. Among them, TOPCon is widely used to represent passivating contact cells using doped polysilicon.

As a continuation of previous silicon solar cells with a high temperature feature, TOPCon structure and processing are discussed in this thesis. SHJ cells are based on low-temperature processes (typically below 200 °C). Compared to traditional silicon solar cells, the process temperature is lower and the equipment is quite different. A brief discussion of SHJ cell process will be presented in the following section.

Figure 2.6 illustrates the structure of the industrial TOPCon (i-TOPCon) cell, as well as its ancestor the n-type Passivated Emitter Rear Totally Diffused (n-PERT) cell. As can be seen in the figure, the structure of the n-PERT cell is similar to that of the i-TOPcon cell. The main difference between the two cells is the passivation on the rear side. TOPCon cell is passivated with thin SiO_x and an n+ doped polysilicon thin film on the rear side whereas the n-PERT cell has an n+ diffused rear side passivated by a SiN_x layer.

The n-PERT cell has a long history of industrial process development in the lab, including the research institutes from ECN, IMEC, ISC, etc., as well as industrial pioneers

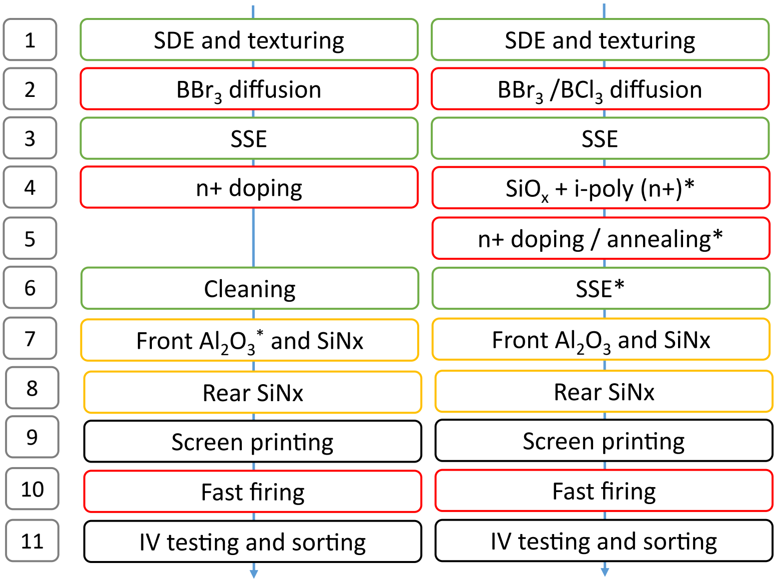

Figure 2.7: Typical process flows of n-PERT (left) and i-TOPCon (right) cells. Wet chemical processes are in green, high temperature processes are in red, vacuum processes are in yellow, and other processes are in black.*Different processes were reported by different companies or institutes.

such as PVGS, bSolar, MegaCell, Yingli (Panda cell in collaboration with ECN and Tempress), Jolywood, and many others. The development of i-TOPcon began around 2018 and is still in progress. The flow of n-PERT and TOPCon cells is depicted in Figure 2.7. n-PERT or i-TOPCon follow similar processes to PERC, which means that most of the equipment can be used immediately or after upgrading.

1. SDE, texturing, and cleaning are the first steps, the same as those in PERC.
2. The second step is BBr_3 diffusion. The emitter is formed by p+ diffusion since the wafer type is changed from p-type to n-type. BBr_3 diffusion is proven to be simple and cost-effective method compared to other methods like ion-implantation [90], or doping from CVD BSG [91]. Diffusion of boron is now widely used through LP-diffusion. As an alternative to BBr_3, Boron Trichloride (BCl_3) can also be used as a diffusion source [92], and was first commercialized by Semco.
3. A single side etching (SSE) process is applied to remove the wrap-around diffusion and to polish the rear side. The front BSG layer is usually kept and used as a barrier or mask during SSE processing.
4. In the case of n-PERT cells, this step completes n+ doping. There are various methods that can be used to accomplish this task, including: 1) $POCl_3$ diffusion; 2) Phosphorous implantation and annealing; or 3) APCVD PSG deposition and annealing. Process flow and equipment selection affect reverse-bias characteristics, and should be carefully chosen [93].
5. i-TOPCon cells can be manufactured using a variety of technologies and processes. Mass production relies mainly on LPCVD and PECVD, both of which are CVD pro-

cesses. In the case of LPCVD: thermal SiO_x was grown on the wafer, and then in-situ intrinsic polysilicon (i-poly) was applied. The n+ doping and annealing were performed in a $POCl_3$ diffusion tube. The LPCVD process can be integrated into the n-PERT cell line. However, one of the bottlenecks is that the low deposition rate of i-poly. In the case of PECVD: First, SiO_x is deposited by PECVD (or PEALD as recently reported in [94]). Second, in-situ doped poly-Si (n+) is deposited by using either tube PECVD, [95] or inline PECVD [96, 97]. Lastly, an annealing step is required to complete the crystallization of poly-Si.

6. For n-PERT cells, a cleaning step is required while for i-TOPcon cells, SSE and cleaning are required.
7. Front passivation includes Al_2O_3 and SiN_x passvation stacks, similar to the rear surface of PERC cells. Passivation can also be accomplished using an in-situ grown stack of SiO_2, BSG, and SiN_x layers reported and patented by the ISC Konstanz [98].
8. A SiN_x passivation layer is deposited by PECVD at the rear.
9. n-PERT and i-TOPCon use similar screen printing processes. The front side is printed with an Al/Ag paste and the rear side is printed with an Ag paste followed by drying.
10. Following printing and drying, a fast firing is performed to form the contact on both sides.
11. The final step is to perform IV testing and sorting. A variety of advanced technologies are now available, such as automatic EL and color sorting.

Different materials and equipment are still being evaluated to improve the process flow for i-TOPcon. A review article by Kafle et al. presents various process routes and manufacturing costs of this technology [99].

In summary, the cell structures and process flows of n-PERT and i-TOPCon are described. Passivating contact cell technologies are exceeding the efficiency limits of PERC. Compared to PERC cells, these cells offer the following advantages: 1) they use n-type wafers with a longer minority carrier lifetime than on p-type wafers. There are several advantages of n-type cells, including no boron-oxygen related LID, improved tolerance to common metal impurities, and higher efficiency. 2) SHJ cells and n-PERT/TOPCon cells offer high bifaciality. SHJ cells have over 90% bifaciality, and i-TOPCon cells have over 80% bifaciality.

In the case of i-TOPCon cells, efforts are currently directed towards improving the passivation of the front side metal region. Various technologies, such as selectively boron-doped emitters by laser [100] or selective polysilicon deposition on the finger area, are being developed for this purpose. Recently, JinkoSolar reported an efficiency of 26.4% [101] TOPCon cell, highlights the efficiency potential of TOPCon cells. The industry is currently prioritizing efforts to reduce capital expenditures, particularly for equipment, and to conserve materials, with a particular emphasis on minimizing the usage of silver.

2.1.4. Learnings from the past

In the last few years, industrial solar cells and manufacturing have undergone a few significant changes. It is important to review the changes in industrial silicon solar cells before discussing IBC cell and module technology.

The first learning is that the changes in the structure and flow of solar cells are inher-

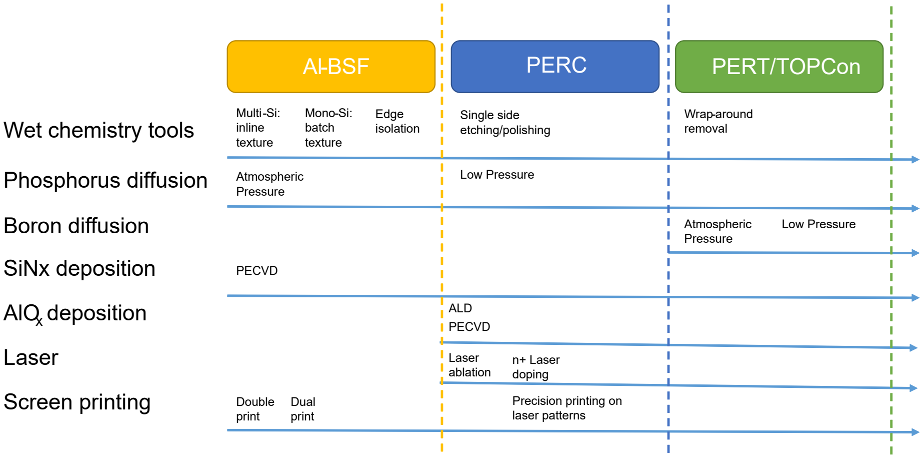

Figure 2.8: Silicon solar cell equipment has been developed steadily from Al-BSF, PERC to TOPCon cells. Selected achievements are listed in the figure.

ited. Solar cell structure change based on the last generation of cells. A few advantages of this approach include 1) less training of production personnel and support resources (materials and supply chain); 2) easy reliability testing, compared to a completely new cell structure; and 3) similar module production processes.

The second learning is the modification of process flows based on mature equipment and processes. After being upgraded, the traditional equipment has shown strong resilience. Since Al-BSF, PERC, and TOPCon cells were developed, the equipment for making solar cells has continued to evolve. There is not only an increase in throughput and a reduction in cost, but also an increase in performance. A selection of achievements is presented in the Figure 2.8. A powerful toolbox is now available for the development of next-generation solar cells. New processes and equipment can be introduced if they are well suited to the new requirements. An excellent example is ALD Al_2O_3. Spatial Al_2O_3 processes and equipment speed up and boost the market penetration of PERC.

The third lesson underscores the significance of materials development, encompassing the three types of materials mentioned below. 1) The rapid development and cost reduction of solar-grade silicon. In 2010, the a-Si thin film solar cells/modules were phased out of the market as a result of price declines in Si materials. 2) A reduction in wafer costs and an improvement in wafer quality. Mono-Si wafers replaced multi-Si wafers, and wafer size was also increased. There are several reasons for this: improvements in ingot and wafer technologies; Continuous Czochralski (CCZ) growth technology; diamond wire saw technology, and finally, PERC solar cells exhibit a higher efficiency gain on mono wafers than multi-Si wafers. A similar transition is currently taking place from p-type to n-type wafers. 3) The development of metallization paste. Various types of Ag pastes have been developed for different cell structures. Various types of Al pastes are developed, from Al-BSF to local Al-BSF, and from full-area printing to finger printing.

There are also the following learnings: 1) The importance of bifacial cells/modules has been widely recognized. 2) For both solar cell and solar module production lines,

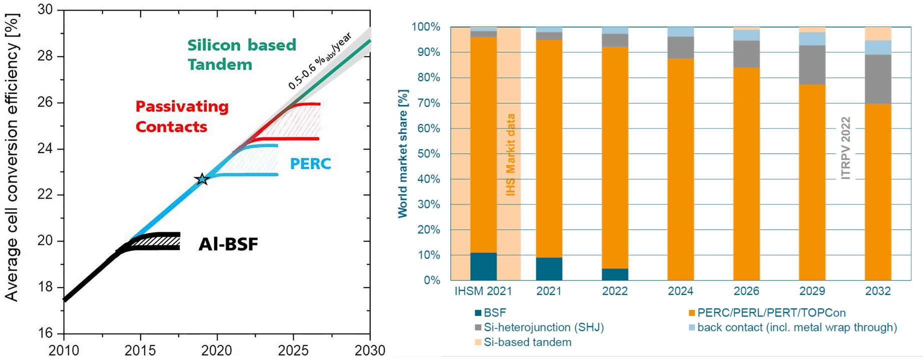

(a) (b)

Figure 2.9: (a) Efficiency trend in history and prediction with different cell technologies. Figure from [102]. Reproduced with permission. Copyright AIP Publishing (2020). (b) Predicted market share of different cell technologies, from [15].

automation development improved the quality of production and reduced the cost of manpower [16]. 3) The development of modules, especially the remarkable improvement in cell-to-module (CTM) losses and gains.

In developing the next generation of cells, we should make use of all the advantages obtained from previous developments. Silicon solar cell technology has developed from the megawatts level to hundreds of gigawatts level over many years, and its efficiency, cost, and reliability are well established. On the basis of current processes and equipment, a new successful cell structure can be developed.

2.2. IBC solar cells and modules

Since the advent of silicon solar cells in mass-production, efficiency has increased by about 0.5 – 0.6 $\%_{\text{abs}}$/year [102]. To maintain this trend, industrial production must adopt new technologies, such as passivating contacts (see Figure 2.9(a)). With passivating contacts, IBC cells can achieve an efficiency of 25% to 26% in mass production, which is considered to be the final evolution for industrial silicon single-junction solar cells [103]. Based on ITPRV's predictions, back contact technology is expected to take over 10% of the market by 2029 and close to 20% by 2032, as shown in Figure 2.9b [15]. The PV market will reach 1 TW/year by 2030 (or even 2028). In the case of back contact technology, the market will be larger than 200 GW/year.

There is a growing interest in back contact cells, especially IBC cells, as the next general technology for cells. SunPower has been producing IBC modules for many years. IBC production has also been launched by SPIC in China since 2019. The top module supplier LONGi launched its back contact modules in 2022 [104]. The leading solar cell manufacturer, Aiko, has also introduced its back contact technologies, featuring silver-free solutions [105]. Mass production is increasingly utilizing IBC technology.

The following subsections provide a summary of the technologies of IBC cells and modules, especially those relevant to this thesis.

Table 2.1: IV of IBC solar cells reported by different companies/institutes

V_{oc} (mV)	J_{sc} (mA/cm^2)	FF (%)	η (%)	Area (cm^2)	Company/ Institute	Comments	Year
737	41.33	82.7	25.2	153.5	SunPower	n-type, passivation n.a.	2016[109]
740.3	42.5	84.65	26.6	179.7	Kaneka	n-type, SHJ-IBC	2017[110]
681.6	41.34	82.47	23.24	4	ipv, University of Stuttgart	n-type IBC, laser doped	2017[111]
715.6	42.3	82.8	25.04	243.2	Trina	n-type, passivated contact IBC	2018[112]
726.6	42.6	84.28	26.1	4	ISFH	p-type (FZ), POLO-IBC	2018[113]
701	42.2	77.8	23.0	2	TU Delft	n-type, poly-Si passivated contact IBC	2018[114]
716	43.0	81	25.0	4	ANU	n-type, passivated contact IBC	2020[115]
736	41.5	81.9	25.0	25	CSEM	n-type (FZ), SHJ-IBC, screen printed	2016[116]
717	39.5	81.7	23.1	244.3	ISFH	p-type (CZ), POLO-IBC	2022[117]
719	42.7	80.4	24.7	274.2	ISC/SPIC	n-type, passivated contact IBC	2022[103]

2.2.1. IBC cell technologies

As early as 1954, Bell Laboratories applied for a patent for back contact cells[106, 107]. Solar cells with back contact include emitter wrap-through (EWT) and metallization wrap-through (MWT), as well as interdigitated back contact (IBC). IBC solar cells have the highest efficiency potential among back contact cells. The first IBC cell, published by Schwartz et al. in 1975 [108], was initially designed for high concentration applications. The technology was successfully commercialized by SunPower Corporation, which was founded in 1985.

IBC technology is regarded as the final solar cell structure in the single-junction cell era [103]. Advantage of IBC cells include: 1) There is no metal shadowing on the front side, resulting in a higher current generation. 2) Low metal resistance losses due to the fact that all metal layers are on the rear. Metallization can be designed with less restriction, and cheap metals such as aluminum and copper can be used. 3) Good performance under UV exposure and hot spot tests. 4) Passivation can be combined with state-of-the-art technologies, such as passivating contacts.

The IBC cell efficiency reported by various companies or institutions is summarized in the table 2.1. The table listed the efficiency ≥ 23% reported in recent years. Except for the POLO-IBC cells from ISFH, most of the reports in the table were achieved on n-type wafers. To make high-efficiency IBC solar cells, passivating contacts should be applied to both p+ and n+ contacts by using SiO_x/Poly-Si (POLO-IBC, or TOPCon-IBC) or by using a-Si (SHJ-IBC). The world record efficiency (2017-2022) of 26.6% was achieved with SHJ-IBC cell structure [110]. When it comes to transferring cell technology from a small to a large wafer, or from a lab process to an industrial process that is cost-effective, it can be a challenge.

Lab-fabricated IBC cells are usually fabricated using complex methods such as photolithography [115]. By using existing industrial equipment, the IBC Process flow can also be simple and cost-effective. A simplified IBC process flow was used in this thesis. This process flow was invented by ISC, and the solar cell was referred to as the ZEBRA IBC cell. ZEBRA IBC cell structures are depicted in Figure 2.10, including the structure of the IBC cell without and with passivating contacts.

A standard ZEBRA IBC cell process flow without passivating contacts is depicted in Figure 2.11 [103]. The process flow can be summarized in 12 steps.

1. The first step is SDE and texturing, followed by cleaning.

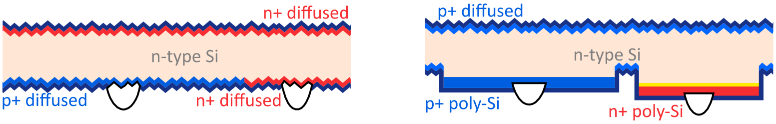

Figure 2.10: Schematic structure of ZEBRA IBC solar cell. The left figure shows an IBC cell without passivating contacts, known as ZEBRA, and the right figure shows an IBC cell with poly-Si/SiO$_x$ passivating contacts, known as polyZEBRA.

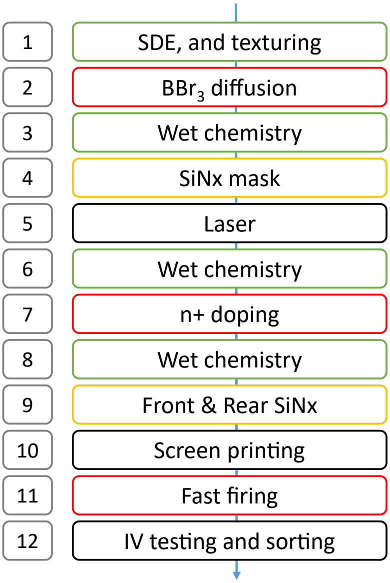

Figure 2.11: Process flow a ZEBRA IBC solar cell without passivating contacts, redrawn from [103]. Wet chemical processes are in green, high temperature processes are in red, vacuum processes are in yellow, and other processes are in black.

2. Low pressure tube BBr$_3$ diffusion is used to form the emitter (p+). One advantage of ZEBRA IBC cells is that the emitter is passivated by BSG and in-situ grown silicon dioxide.
3. Following BBr$_3$ diffusion, the BSG layer is cleaned using wet chemistry. Details regarding wet chemistry steps are discussed in the following paragraphs.
4. A SiN$_x$ mask layer was deposited by PECVD.
5. Laser is used for the patterning process. BSF (p+) regions are ablated by laser.
6. A wet chemistry cleaning step is performed before n+ doping.
7. The n+ doping is achieved by LP-POCl$_3$ diffusion.
8. After POCl$_3$ diffusion, another wet chemistry cleaning is followed to etch the PSG layer.
9. SiN$_x$ passivation is typically performed by PECVD on both the front and rear surfaces.
10. The process of metallization is carried out by screen printing. Typically, four to

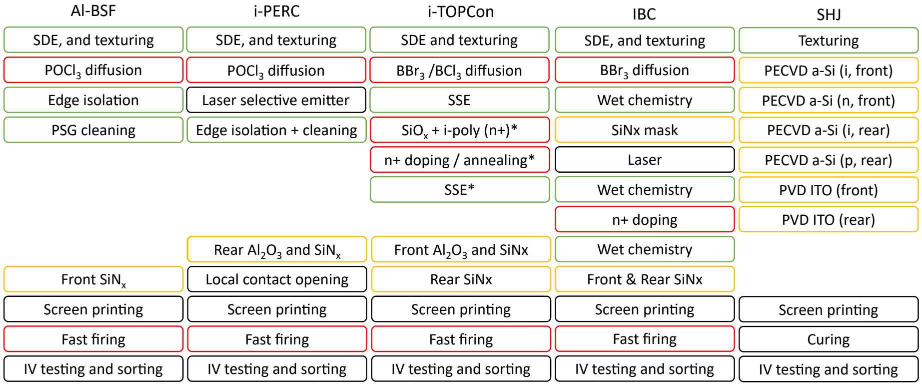

Al-BSF	i-PERC	i-TOPCon	IBC	SHJ
SDE, and texturing	SDE, and texturing	SDE and texturing	SDE, and texturing	Texturing
$POCl_3$ diffusion	$POCl_3$ diffusion	BBr_3 /BCl_3 diffusion	BBr_3 diffusion	PECVD a-Si (i, front)
Edge isolation	Laser selective emitter	SSE	Wet chemistry	PECVD a-Si (n, front)
PSG cleaning	Edge isolation + cleaning	SiO_x + i-poly (n+)*	SiNx mask	PECVD a-Si (i, rear)
		n+ doping / annealing*	Laser	PECVD a-Si (p, rear)
		SSE*	Wet chemistry	PVD ITO (front)
			n+ doping	PVD ITO (rear)
	Rear Al_2O_3 and SiN_x	Front Al_2O_3 and SiNx	Wet chemistry	
Front SiN_x	Local contact opening	Rear SiNx	Front & Rear SiNx	
Screen printing	Screen printing	Screen printing	Screen printing	Screen printing
Fast firing	Fast firing	Fast firing	Fast firing	Curing
IV testing and sorting	IV testing and sorting	IV testing and sorting	IV testing and sorting	IV testing and sorting

Figure 2.12: Solar cell process flow. Different types of process/equipment are highlighted in different colors. Wet chemical processes are in green, high temperature processes are in red, vacuum processes are in yellow, and other processes are in black.

five printing steps are involved in the printing process, and each printing step is followed by a drying step. A state-of-the-art screen printer can meet requirements such as alignment accuracy and throughput. A discussion of screen printing technology will be provided in the following chapter.

11. To form the metal contact to doped silicon, a fast firing step (peak firing temperature of 750 °C to 850 °C) is included using an inline firing furnace.
12. The last steps are IV testing and sorting. IV testing and sorting (including automatic EL and color sorting) can be conducted using the latest technology. Since all contacting devices are located at the rear of IBC cells, a new contacting device is needed. In Chapter 3, a contact device is discussed.

Based on the above process flow, poly-Si/SiO_x passivating contacts can also be incorporated. A ployZEBRA cell process flow is described in the paper from Linke et al.[118].

In order to manufacture low-cost high-efficiency IBC solar cells, there are a few challenges that must be overcome. First, cleaning of wafers. In laboratories, methods such as RCA and SPM (sulfuric peroxide mix) are used for cleaning, but these methods are not suitable for industrial use due to their high costs. The good news is that there are solutions available for high-efficiency solar cells, such as HF/O_3 cleaning, which is comparable to SPM cleaning in terms of cleaning efficiency [119]. Second, the patterning technologies. Lasers are proving to be a good solution for both research institutes and industry [113, 120]. Other solutions, such as shallow masks, are still under development to meet industrial needs [121]. The third challenge is the metallization process. SunPower has chosen plating for metallization. Currently, SunPower is the only manufacturer of solar cells that utilizes plating for metallization. The main metallization technology used in industry is screen printing. After many years of development, screen printing has been able to meet the requirements for IBC cells, from alignment accuracy to cost. A detailed discussion of screen printing technology can be found in Chapter 3. The last challenge is the costs, which can be addressed at three levels: 1) COO of cell and module. IBC has a higher COO of cells which is mainly due to the high Ag usage. Reduction of Ag usage is possible and is discussed in the next subsection. 2) Capex costs. The IBC cells stand on the shoulders of giants (Al-BSF, PERC, and TOPCon). IBC cells have a similar capex cost due to the similar process flow and equipment used. Figure 2.12 summarizes the cell process flow from different cell structures, along with different types of equipment highlighted in different colors. The process flow for SHJ cells is shorter than that of i-TOPCon or IBC cells. However, since SHJ uses different equipment, the capex is higher than others, and the reducing the capex may take a long time. 3) At LCOE level, IBC technology may achieve a similar or even lower LCOE than other technologies [103]. Mass production of IBC is anticipated once the challenges outlined above have been solved.

2.2.2. IBC modules technologies

Making IBC modules is not a straightforward task, due to the fact that all the connections are at the rear side. There are several types of interconnection method for back contact cells.

- Industrial solutions from SunPower and LG. IBC cells from SunPower with a busbar at the edge of the cell. By soldering the busbars using a specially designed connector, the cells can be connected to a string [122]. LG claimed that 30 multi-ribbon busbars were used for their IBC cells [123]. However, no technical details regarding interconnection were released. Both cases require specially designed interconnection solutions and customized equipment.

- Interconnection using wires or ribbons in encapsulate. One example is Meyer Burger's SmartWire Connection Technology (SWCT). SWCT technology has been applied to back contact cells [124]. The multi-wire is coated with low-temperature solder and is integrated into an encapsulate. Interconnections with back contact cells are made during lamination. Researchers from IMEC used a 3D multi-ribbon interconnection for back contact cells. A pre-fabricated 3D metal interconnection ribbons (also with low-temperature solder) in polymer encapsulate were used [125]. Both methods are suitable for back contact cells, especially when low temperature interconnection processes are required, such as on heterojunction back contact cells.

- Conductive backsheet solutions. Conductive back sheet is widely used in MWT modules. Suppliers of equipment, such as Eurotron, have demonstrated such equipment in the past [126]. Module suppliers like Sunport produce back contact modules with conductive back sheets. To further reduce the cost, aluminum foil can also be used [127].

- Soldering solution using ribbons. Front-and-back contact cells are commonly soldered with ribbons. In the first step, ribbons are placed on the busbars of the cells. Following that, the cells are soldered with infrared (IR) lamps, hot air, an electronic iron, or an induction method. Traditional solar modules have been manufactured using this technique for many years. This method can also be used to make back contact cells with modifications to the soldering stringer.

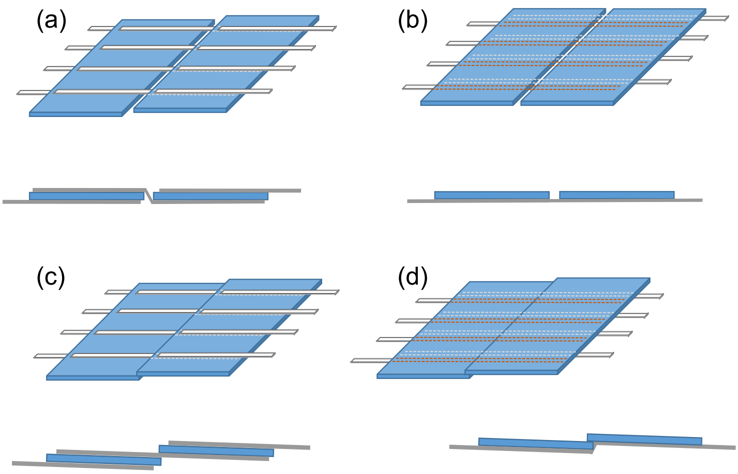

Figure 2.13: Isometric and cross-sectional views of the interconnection of different contact cells. (a) front-and-back contact cells interconnected with ribbon, with a gap between cells. (b) back contact cells interconnected with ribbon, with a gap between cells. (c) front-and-back contact cells interconnected with ribbon, with a negative gap between cells. (d) back contact cells interconnected with ribbon, with a negative gap between cells (patent pending).

Among the methods, the traditional ribbon connection method is attractive, because of the following reasons: 1) Existing equipment can be used. Traditional stringer equipment can be upgraded to allow for the soldering of back contact cells. 2) Existing module processes can be used. Expect soldering, other processes are the same as traditional processes. With this method, the equipment cost is comparable to that of standard modules and less than with the other methods. Using the same module process flow, the standard module quality control methods can be applied. For example, modules can be checked with EL before lamination. Module quality can be better controlled and checked than with technologies that use wire or ribbon in encapsulates. 3) Equipment upgrade is possible for multi busbars back contact cells. Multi busbars can be used for back contact cells to further improve efficiency and reduce cost. Stringers may be upgraded to multi-busbars accordingly, as was done in the case of soldering front-and-back contact cells in the past. 4) Interconnections can be soldered or glued using ECA, providing greater flexibility. 5) Bifacial module can be made by this method. Compared to the conductive back sheet solution, bifacial IBC module can be realized.

However, there are also challenges. One of the main challenge is cell bending/bowing due to the different temperature coefficients of ribbons and silicon solar cell. After high temperature soldering process (in the range from 200 °C to 300 °C) of a full size IBC cells, a cell bowing larger than 10 mm was observed for a M2 cell. Several solutions have been proposed. 1) Pre-bending the solar cells before soldering, which was proposed and developed by ISC. By pre-bending the cells using a customized soldering station, and then soldering the cells, the bowing can be offset [128]. 2) Wave-structured copper ribbons can be used to reduce stress during soldering [129]. 3) Using cut cells. As bowing is determined by the soldering length, it can be directly reduced by using cut cells. Addi-

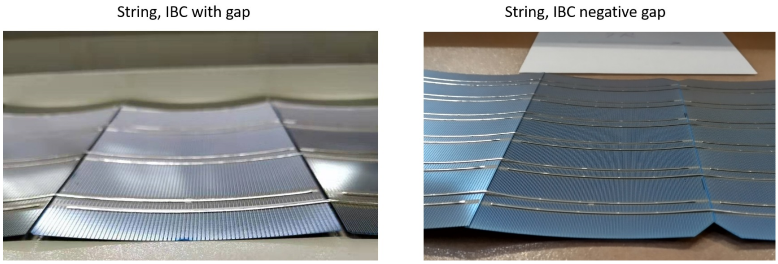

Figure 2.14: IBC cell strings soldered with gap design (left) and negative gap design (right).

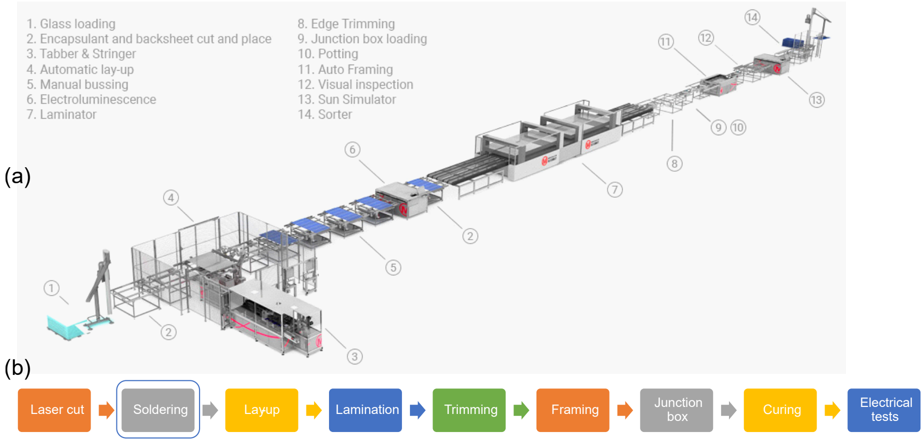

Figure 2.15: Module process flow. (a) Layout of an industrial solar module production. Courtesy of Mondragon Assembly [131]. (b) Schematic of the ribbon connected back contact module manufacturing flow.

tional module power gain may achieved from half-cut IBC module due to less Rs losses, and other benefits from cut cell modules, for example, better shadowing behavior. More attractively, gapless/negative-gap modules are possible. The half-cut ribbon interconnection of IBC cells is explained in Figure 2.13, and standard front-and-back contact cells are shown as references. (a) front-and-back contact cells are interconnected with ribbon, with a gap between cells. In the latest developments, front-and-back contact cells can be soldering with a negative gap shown in (c). For IBC cells, interconnection of cells is shown in (a) with gap between cells. Similarly, IBC cells can be soldered with negative gaps, shown in (d). A gapless module method, which has neither gaps between cells nor gaps between strings, has been proposed by ISC (patent pending) [130].

In mass production, ribbon and standard soldering have been used to connect IBC cells. Photos of string with gap and negative gap are shown in Figure 2.14.

The IBC module process can be accomplished in a similar way to the traditional front-and-back contact module by using half-cut cells and soldering process. An example of a module production line layout and a typical module process flow are shown in Figure 2.15. Modules are made as follows:

1. The first step is to laser cut the cells. In this step, the full size IBC cells are cut into

half cells. The laser cut on IBC cells is discussed in Chapters 3 and 4, and a solution to repassivate the cut edge is presented in Chapter 5.

2. The second step is soldering with stringer. The traditional stinger can be used to solder back contact cells after an upgrade. In this step, 10 or 12 pieces of cells are soldered in a string using the interconnection method shown in Figure 2.13.
3. The following processes are similar to the traditional process, including lay-up, lamination, etc., as shown in Figure 2.15. A bill of materials (BOM) should be developed for the back contact cells and module, which includes: front glass, front encapsulate, rear encapsulate, rear glass or backsheet, and frame.

2.3. Challenges and opportunities

It is generally believed that tandem solar cells will be the next generation of solar cells. For single junction solar cells, the last evolution will be back contact solar cells.

Solar cell technology is always being pursued for higher efficiency, lower cost, higher reliability, and greater sustainability. There are both opportunities and challenges for the development of new technologies. The focus of this thesis is on: 1) Further improvement in efficiency of IBC cells/modules, including the reduction of cell-to-module efficiency losses. 2) By using copper metallization, the module cost can be reduced and the sustainability can be increased.

2.3.1. Edge loss and cell-to-module efficiency losses

As shown in this chapter, silicon solar cell passivation has been continuously developed over many years, and the combination of advanced cell structures with different passivation materials has significantly improved efficiency. Contrary to surface passivation, edge passivation generally is less effective. The passivation of the edge of a solar cell is usually a beneficial side effect of surface passivation. Moreover, cutting and/or cleaving processes for making cut-cell modules introduce unpassivated edges that cause additional edge recombination and reduce efficiency. This cut loss is a part of cell-to-module losses.

Currently, the cell efficiency record for the world is 26. 81%, which is 2. 6%$_{\mathrm{abs}}$ below the theoretical efficiency limit of 29.4% [28]. The best module efficiency on the market, however, is only 22.8% from SunPower. The efficiency different between cells and modules usually refer as cell-to-module (CTM) losses. The CTM losses should be considered during the development of cells and modules. CTM losses are due to many factors, and can be simulated by using the software SmartCalc.CTM developed by Fraunhofer ISE.

For a half-cut IBC module (with gap between cells and standard module design), the typical CTM efficiency changes are shown in Figure 2.16. The main causes of CTM losses are shown in the figure as follows: 1) module margin, 2) cell spacing, 3) cover reflection, 4) cut losses, and 5) cover absorption. Among them, the cut losses are important for solar cell and modules, especially when the cut edge-to-area ratio is high (as in shingle modules, for example). The cut losses shown in the figure are the result of cutting through the emitter region, and can be further reduced to 0.1%$_{\mathrm{abs}}$. CTM gains are from: 1) cell/encapsulant coupling and 2) cover coupling. Based on this simulation, the module efficiency is limited to 22.1%. However, with advanced module designs (e.g. gapless

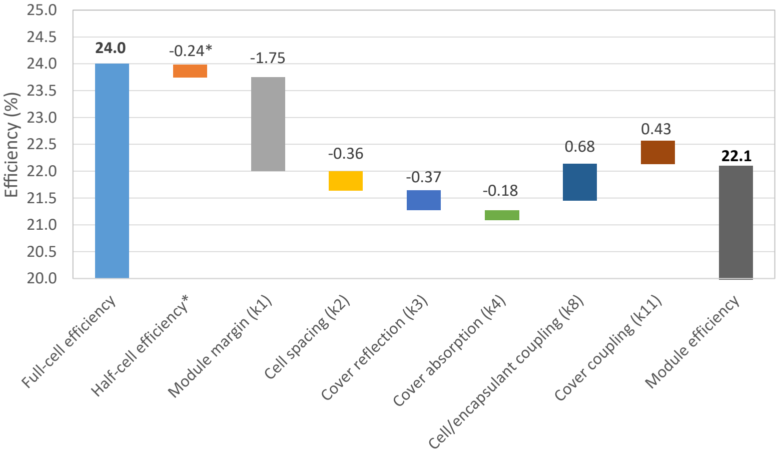

Figure 2.16: ZEBRA half-cut cell-to-module (CTM) losses and gains, efficiency changes less than 0.1% are not shown in the Figure. Simulation results from SmartCalc.CTM, except of the efficiency loss from full-cell to half-cell. *Half-cell efficiency loss can be improved, the study is shown in Chapter 4.

design) and higher efficiency solar cells, the efficiency of the IBC ZEBRA module can be improved to over 22.3%.

In this thesis, laser cut and efficiency losses of IBC cells are studied. Laser cutting is summarized in Chapter 3.1. The cutting losses of IBC cells can be mitigated by cutting through the BSF regions, as discussed in Chapter 4. In addition, Chapter 5 proposes a solution to further reduce cut losses by passivating the edges.

2.3.2. Silver usage and sustainable metallization

In the past, the PV industry has focused primarily on reducing the cost of solar cells and modules. Materials supply is not an issue for PV, since it is a small part of the energy industry. When PV reaches TW levels and becomes a major energy source. Sustainability is one of the new boundary conditions. Materials availability is one of the challenges for PV industry.

In addition to cost, sustainability of the material is also becoming a major concern. IBC cells face a number of challenges, primarily high metallization costs and the use of too much silver (not sustainable). Because IBC cells use silver in both polarities, they consume more than twice the amount of silver as PERC cells. In addition to high costs, this also restricts large scale deployment due to sustainability concerns.

Fortunately, the design of IBC cells offers an advantage wherein all metal patterns are positioned on the rear side. Consequently, the utilization of wider metal patterns in IBC cells does not result in any efficiency losses on the front side. Although there may be a slight compromise in rear-side efficiency, the absence of shadowing losses provides greater flexibility in the design of metallization for IBC cells. For IBC cell and other back contact cells, low-cost and sustainable materials can be used, such as Al or Cu. These materials can be applied to the cells through plating or screen printing methods.

In this thesis, the screen printed copper paste was evaluated for IBC solar cells. Silver

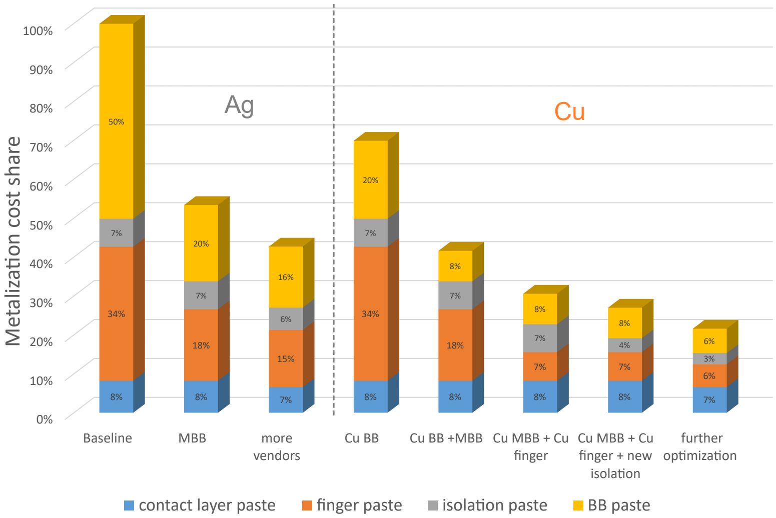

Figure 2.17: ZEBRA IBC cell metallization cost breakdown and road map.

is replaced with copper paste in IBC cells as fingers and busbars.

By using copper, the metallization cost can be reduced by 80%, with only 4.5 mgW^{-1} silver usage, resulting in a lower metallization cost than PERC. Figure 2.17 shows the cost reduction road map for metallization of IBC cells using silver and copper. This calculation is based on the following: 1) A baseline cell design consists of four pairs of busbars. 2) Multi-busbar design with 9 pairs of busbars. 3) Compared with silver, copper has a assumed cost factor of 0.4 in the road map. 4) Further optimization including process optimization in mass production and cost reduction due to economies of scale.

The copper solution for IBC cells is discussed in detail in Chapter 6. Copper paste was used to make high-efficiency large-area IBC cells. As a result, the use of Ag was reduced to 4.5 mgW^{-1} while maintaining efficiency and reliability.

3

Materials and methods

Abstract

This chapter provides a detailed description of the materials and methods used in this thesis, including:

- Laser cutting equipment and processing. This section covers different laser cutting techniques, such as laser cut and cleave, TLS, and cleaving. Laser damage is also discussed.

- Screen printers and screen printing processes. The section covers screen printers, screen printing processes, as well as screens.

- Characterization and reliability tests. This section discusses the methods used for characterization and reliability tests. Specifically, current and voltage (IV) and photoluminescence (PL) measurements were set up for this study. An IV measurement contact chuck was developed specifically for this purpose. This chapter also details the PL measurement on the wafer edges. Finally, the reliability tests are explained.

3.1. Laser and cell cut techniques

Lasers have been used in the manufacturing of silicon solar cells and in various applications [132] for many years.

Initially, lasers were used for edge isolation. In Al-BSF cells, for example, the emitter may diffuse around the edges to the rear BSF, causing shunts. Lasers were used to create laser groves so that the wrap-around emitter and BSF could be electrically isolated. However, due to high breakage and efficiency loss, the laser isolation technique was replaced by wet chemical etching [45]. In PERC cells, laser doping is the standard process for selective emitters [133]. Lasers are also used for ablation of the Al_2O_3/SiN_x layer, helping to ensure that silicon and Al are in contact. For back contact cells, lasers are used to drill holes in MWT/EWT cells; laser ablation of coating layers can also be used to create patterning in IBC cells [111]. As an accurate and fast technique, lasers can be used to create patterns on large area solar cells with high accuracy. With laser patterning, there is no need for additional materials or processing steps, making it a cost-effective solution. During the past few years, laser technology has developed to the point that it can be used in the mass production of back contact cells.

Other processes can be combined with laser technology. Laser Chemical Processing (LCP), including laser and chemical processing, has been used for many different purposes [134, 135]. Lasers are used in the metallization process, including pattern transfer printing for fine line printing [136, 137] laser firing and laser enhanced contact optimization (LECO) for helping with contact formation [138]. Laser is also used to enhance hydrogen passivation [139]. Laser can be used for characterization, for example, photoluminescence (PL) using laser as excitation source. Additionally, laser cutting can be used to make cut cells for modules.

Lasers are used in this thesis for patterning during cell processing, as well as for cutting cells to make modules. The following section focuses on laser cutting.

3.1.1. Laser cut and cleave of solar cells

Half-cut cell modules dominate the module market. Before module production, full cells are cut into half cells. In this thesis, three types of cell cutting techniques are examined, including laser cut and cleave (L&C), thermal laser separation, and cleaving.

The industry standard method for cutting or cleaving cells is L&C. First, a laser is used to create grooves on the surface of the solar cell. Second, the solar cells are mechanically cleaved along the grooves.

The laser used in this study can be seen in Figure 3.1. The laser system is the model of Powerline F20 from Rofin with a wavelength of 1064 nm and a frequency between 20 and 100 kHz. It consists of three main components: an electrical rack, a Galvo scanner and laser head, and a process chamber. As seen in Figure 3.1(b), a desired laser pulse is generated from the pulsed fiber laser unit, then amplified by the fiber amplifier to the desired pulse energy. Then the laser is transferred through the transport fiber. The Galvo/marking head with two mirrors, which can control the laser beam movement through x and y directions, according to the laser pattern design.

An example of a laser cutting recipe is shown in Table 3.1. The pumping power is set at 80% of the maximum power of the laser (14 watts). The laser cut depth on a textured silicon wafer with a 75 nm SiN_x coating is 60 μm using the recipe.

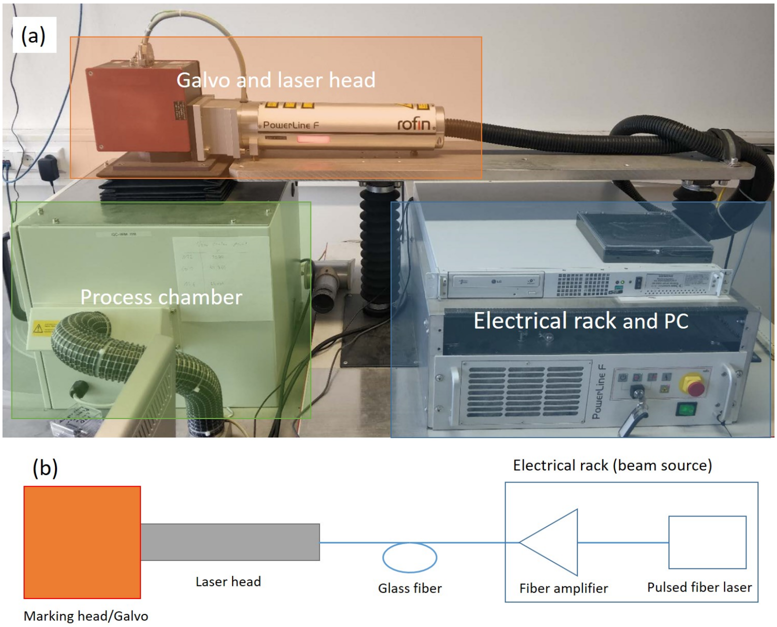

Figure 3.1: The laser cutting equipment used in this thesis. (a) Main components of laser system (Powerline F20 from Rofin). (b) A schematic drawing of the laser system, adapted from the equipment manual.

Table 3.1: A laser cutting recipe using F20 laser, with a cut depth of 60 μm.

Parameters	Value	Unit
Pumping power	80	%
Frequency	30	kHz
Speed	500	mm/s
Pulse width	10	μs
Scribe times	5	times

L&C provides a easy and cost-effective method for cutting solar cells. When laser scribing is performed with nanosecond lasers, however, undesired laser damages are introduced. Laser cut damages are explained in the Figure 3.2. The wafer is usually scribed multiple times by laser in order to create the groove with enough depth (between 30% and 50% of the wafer thickness). The figure 3.2(a) shows a single laser scribe on textured silicon. The SiN$_x$ was ablated, and a shallow groove (7 μm in the figure) was created by laser. (b) The wafer was laser scribed three times. The laser groove depth was increased to 21 μm, but the laser groove width remained the same. (c) Different types of laser damage are shown. On the surface of the wafer, laser process causes debris and surface ripples. The textured surface of the wafer was damaged, and silicon is was melted and recasted as a recast layer, which is higher than the original surface. The groove sides show recasted layers owing to scribbling. Silicon was damaged by laser heat transfer in the laser groove. During laser cutting and cleaving, micro cracks can also occur.

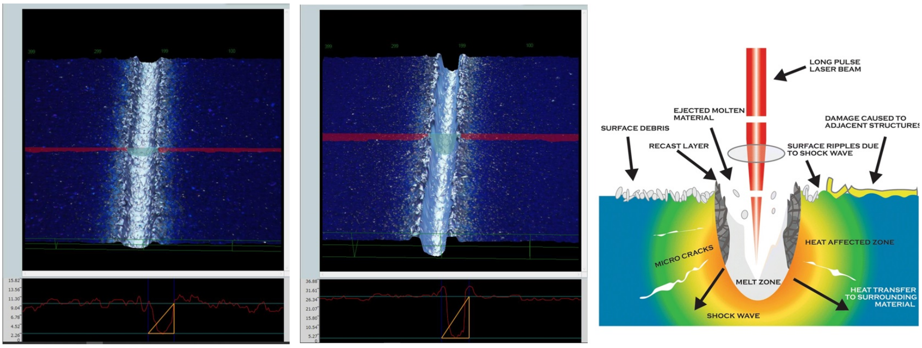

(a) (b) (c)

Figure 3.2: Damages caused by laser scribing. (a) A single laser scribe, cut depth 7 μm; (b) Three times of laser scribes, cut depth 21 μm; (c) Different types of damages caused by laser, courtesy of Clark-MXR, Inc [140]

These laser induced damages may result in mechanical and electrical degradation of the solar cells. Several technologies have been developed that can minimize laser damage, if not eliminate it.

3.1.2. TLS and 45° cleaving

Thermal laser separation (TLS) has been used to separate brittle materials, and in recent years has been used to separate silicon wafers [141, 142]. There are two steps involved in the TLS process. First, a laser is used to initiate a crack at the edge of wafer. Second, the wafer is locally heated by laser and subsequent cooling by water. As a result of thermal-induced mechanical stress, wafer separation occurs along the laser-heated lines. 3D-Micromac AG introduced TLS process to solar cells industry. The TLS used in this investigation was also supplied by 3D-Micromac.

Wafer separation can also be accomplished through 45° cleaving. Silicon wafers of solar cell are usually oriented in a (100) plane. Wafer edges are generally oriented along (010). It is possible to manually cleave wafers by creating a small damage with a diamond pen, then manually cleaving the wafer from the damage area. Wafers will be separated along (110) orientation, which is 45° along the edges. This method, however, cannot be used to cut solar cells.

Alternatively, wafers can be cut from rotated ingots, a method proposed by CEA INES researchers [143]. In this method, the wafer ingot is rotated by 45° during the ingot squaring process. The wafers can then be cleaved along (110), which is then parallel to the wafer edge. TLS and 45° cleaving significantly reduce laser damage, which is important for edge passivation. In Chapter 5, results of edge passivation are presented.

By examining the cut edges, different techniques can also be distinguished. Figure 3.3 shows cross-sections of the cut edges using the three different methods. The cut edge from laser cutting and cleaving is shown in (a). The image clearly shows laser damage. The figure (b) illustrates the TLS cut edge. The laser damage is visible in the enlarged image, with a laser damage depth of approximately 10 μm. All other parts of the wafer have been cleaved with stripes, but have not been damaged by lasers. (c) shows the 45°

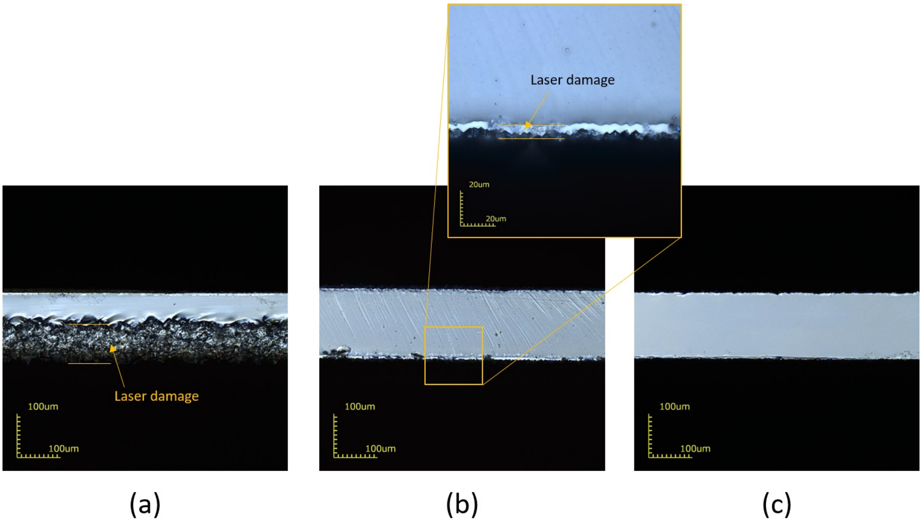

Figure 3.3: Cross-sectional views of wafer edges cut by different methods. (a) Laser and cleaving, resulting in a deep laser damage. (b) With TLS, the laser damage is limited to around 10 μm, as shown in the enlarged image. (c) 45° cleaving without visible laser damage.

cleaving sample. There is no laser damage on the wafer edge.

Comparing the three cutting methods: As a standard process in the current production line for PERC cells and modules, L&C has the lowest cost and is widely used. TLS shows the advantages of better mechanical stability, and even better module power [144, 145]. The equipment cost was the bottleneck for this technique. As the market shifts to larger wafers, and new cell technologies, such as SHJ cells, are more sensitive to process temperature, the market share of the TLS method is on the rise. The 45° cleaving is not used in production line yet. However, with this method, the wafers can easily be cleaved and used in research for cutting edge studies. Industrial application depends on further development of this method, for example, suitable cleaving equipment and breakage control during the cell and module fabrication process.

3.2. Screen printing

Screen printing can be traced back to centuries-old stenciling techniques used in China, Egypt, Japan, and other parts of the world. The first screen printing patent was granted to a man named Samuel Simon from Manchester, England in 1907 [146]. Currently, screen printing is the primary metallization technology for industrial silicon solar cells [15].

In this study, metallization is accomplished by screen printing. The screen printer used in this study is the EKRA XH2 from ASYS Group, as illustrated in Figure 3.4. The figure (a) depicts a photo of an overview of the printer. The printing station (b) includes the printing head, the screen, and the flood bar. In (c), a copper paste printed IBC ZEBRA solar cell is depicted. The printer is equipped with a camera alignment system with an alignment accuracy of ±12.5μm @ 6 Sigma. Wafers are automatically loaded and unloaded before and after screen printing. For drying the paste, an inline drying furnace

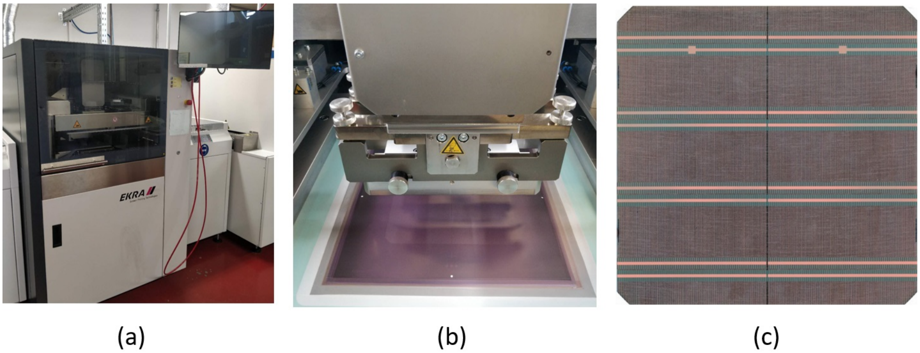
(a) (b) (c)

Figure 3.4: (a) Printer used in this study (EKRA XH2 from ASYS). (b) Printing head, screen and flood bar. (c) A cooper paste printed IBC cell from this study.

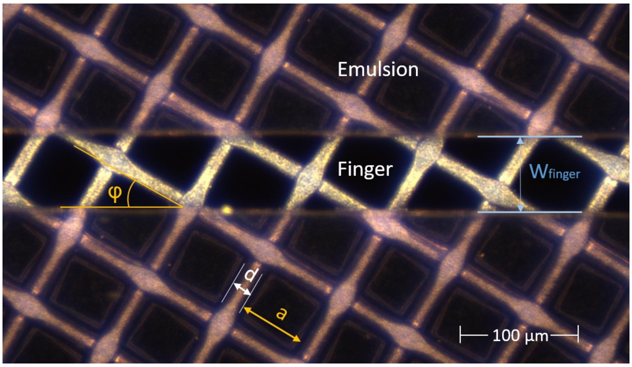

Figure 3.5: Microscope image of a screen with a finger opening of 70 μm.

from Rehm Thermal Systems GmbH is connected after the printer. Paste can also be dried in ovens. At printing and drying, a fast firing process is available. Solar cells can be fired with an inline belt firing furnace from Centrotherm up to 1000 °C.

In addition to the printer, the screen is another important component of the screen printing process. A microscope image of screen is shown in Figure 3.5. The screens are made of stainless steel mesh (or polymer in some applications) and emulsion. The figure illustrates some of the most important parameters of a screen, which is the wire diameter (d) and screen opening (a). The mesh count (MC) of a screen refers to the number of openings per linear inch. Screen opening ratio (OR) can be calculated from d and a, or from MC and d [147].

$$OR = \frac{a^2}{(a+d)^2} = (1 - MC \times d)^2. \tag{3.1}$$

Other important parameters include: emulsion thickness, screen thickness and mesh angle (angle of wire mesh relative to frame, ϕ in the Figure).

Screens have been developed for cells printing for many years. Table 3.2 shows the parameters of the screen used for solar cell (finger) metallization, including the mesh

Table 3.2: Screen mesh count, wire diameter, and opening ratio used for cell printing. Data from past (top) to present (bottom)

Mesh Count (/inch)	Wire diameter (μm)	Opening ratio (%)
325	23	49.8
360	16	59.8
325	16	63.2
380	14	62.5
430	13	60.8
480	11	62.7
520	11	60.0

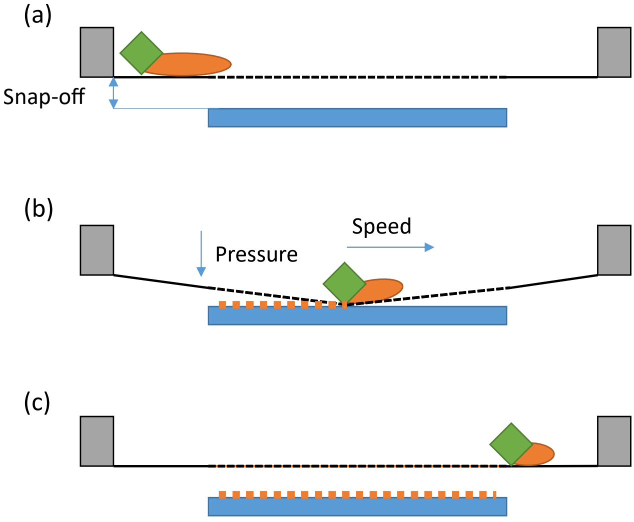

Figure 3.6: Printing process, including (a)before printing; (b) during printing; (c) printing finished.

count, wire diameter, and opening ratio. The opening of the screen was around 50% on screens with mesh count 323/inch, and wire diameter 23 μm. Currently, screens with a higher mesh count, thinner wire, and an opening ratio greater than 60% are used. Several new screen technologies are being developed, such as calendaring process (see the knot area is flatted in the Figure 3.5), and knotless screen (screens with 0° mesh angle, and finger openings are free of knots [148]). A finger width of 20 μm can be printed with screen printing [149].

For IBC solar cells, it is worth noting that the finger width is not limited to fine lines only. The finger can be wider, and screen requirements are not as high as with PERC.

Having a paste, a screen, and a screen printer, the screen printing process can now be done. The printing process is illustrated in Figure 3.6. (a) The first step in mounting the screen to the printer is to apply a well-mixed paste to it. (b) Second, paste is printed with the printing squeegee (green diamond shown in the figure) with a press and speed. (c) After the substrate printing is complete, the pressure is released and the substrate can be removed. A flood bar is attached to the printing head, allowing the paste to be flooded before or after printing. Various parameters can be controlled to control the printing process, such as the snap-off distance between the printing substrate and the screen, the printing speed, and the printing pressure. In the printing process, paste lay-down is an important indicator. The laydown of the paste is mainly influenced by the following factors: 1) Screen design, mesh choice, and thickness (emulsion and screen). 2) Properties of the paste (viscosity, for example). 3) Printing parameters, such as printing speed, pressure, squeegee angle and hardness, etc.

For solar cells with patterns, the accuracy is another important parameter for the screen printer, as it ensures the printed patterns align to the previous ones. Printing alignment accuracy has been improved from Al-BSF cells to IBC cells. The alignment of Al-BSF cells requires: 1) all patterns printed on the wafers; 2) Ag contact paste aligned to Al paste pattern. In later stages, double printing and dual printing were introduced to increase cell efficiency. The double printing process requires print-on-print alignment or finger-on-finger printing. The development of selective emitters required further alignment of accuracy. Printed fingers should be aligned with selective emitter patterns, either by laser doping or by other means. Additionally, bifacial PERC cells must have their Al fingers aligned with the laser ablation sites. A misalignment in the printing process leads to contact issues, or even shunts, which reduce the yield of solar cells. The printing alignment for IBC cells requires: 1) fingers should be printed on the $p+$ or $n+$ regions. Incorrect alignment may cause shunts. 2) If more than one layer is used for printing, the printing of different layers must be aligned.

Currently, the printers have an accuracy of $\pm 10\mu$m @ 3 Sigma [15]. A screen printed pattern can be aligned with a laser pattern with high precision. For example, 40 μm screen printed fingers can be aligned to 70 μm laser pattern on a 6-inch wafer was reported [150]. The printing accuracy is sufficient to meet the requirements of IBC cells.

3.3. Characterization and reliability

Throughout this study, the main characterization tools employed were: current and voltage (IV) including Suns-V_{oc}, electroluminescence (EL), and photoluminescence (PL). The two main types of reliability tests are the damp heat test and the thermal stress test.

3.3.1. IV testing of back contact cells

The IV tester and measurement chuck used for this study is shown in Figure 3.7. The IV test is from halm elektronik GmbH, and its main components are shown in Figure 3.7(a). Testing chamber interior: an xenon lamp is used, a pyrometer is on the left, an EL camera is on the right, and a custom-made contact unit is at the bottom. Several chucks were tested for the measurement of IBC cells, including a probe contact chuck and chucks were designed and manufactured using printed circuit board (PCB) technology. A PCB chuck for measuring 6 busbars IBC cells is shown in (c).

To accurately measure high-efficiency IBC cells, hysteresis measurement is provided by the IV tester[151]. Using a single light pulse to measure forward- and reverse-sweep curves, the steady-state curve can be determined. Suns-V_{oc} measurement [152] is integrated into the IV measurement. Parameters like pFF and iV_{oc} can be determined. At

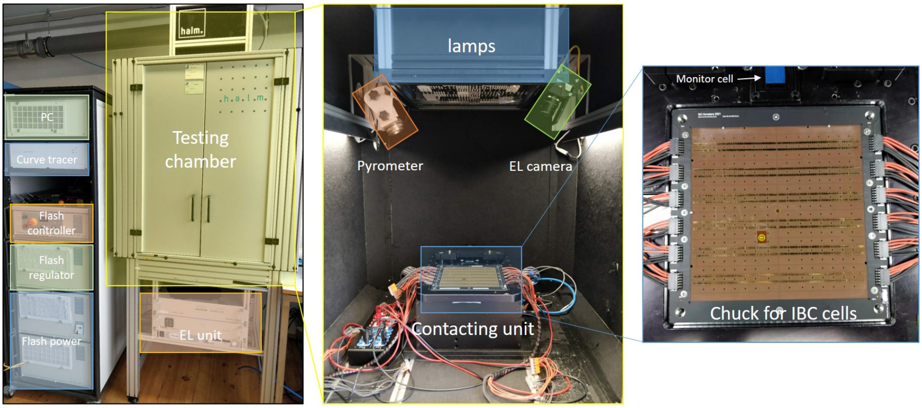

(a) (b) (c)

Figure 3.7: IV tester and measured chuck used in this study. (a) Main components of the IV measurement system. (b) Inside of testing chamber. (c) A specially designed PCB chuck for measuring IBC cells.

Table 3.3: IV results measured on a 1/4 M2 cell at different time of the same day

Measured sequence	$V_{oc}(mV)$	$J_{sc}(mA/cm^2)$	$FF(\%)$	$pFF(\%)$	$\eta(\%)$
1	690.2	40.891	78.19	82.26	22.07
2	690.0	40.890	78.22	82.31	22.07
3	690.1	40.893	78.12	82.28	22.05
4	690.0	40.892	78.15	82.32	22.05
5	690.2	40.892	78.14	82.32	22.05
6	690.1	40.890	78.18	82.33	22.06
7	690.3	40.891	78.30	82.34	22.10
Average	690.1	40.891	78.18	82.31	22.06
STD	0.1	0.001	0.06	0.03	0.02

last, different contact chucks were tested in the study, especially the PCB chuck.

Using PCB technology to design complex contact patterns for characterizing IBC solar cells is not only easier, but it is also a more cost-effective method of fabrication compared to traditional approaches involving probe contacts. Measurement results are comparable to those obtained from probe contact chuck, except for FF. Since the resistance of the contact bars is taken into account in the measurement of the FF, the FF measured from a PCB chuck is more closely related to the FF measured from modules. With the PCB chuck, it is possible to measure the IV with high repeatability, even for small cells. Table 3.3 presents IV results measured on the same cut cell (a 1/4-cut M2 cell). The results demonstrate excellent repeatability measured from the chuck.

3.3.2. Photoluminescence

The Photoluminescence (PL) measurement setup used in this study is shown in Figure 3.8. The PL can provide both spatial and temporal information about the passivation

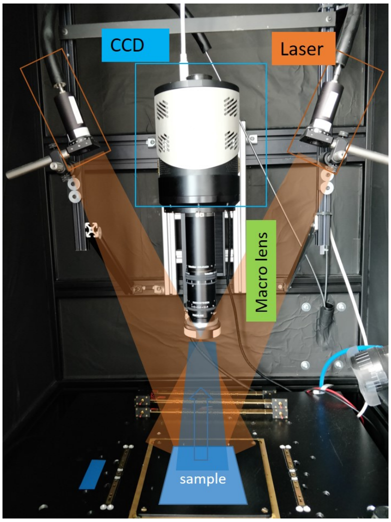

Figure 3.8: Photoluminescence measurement setup

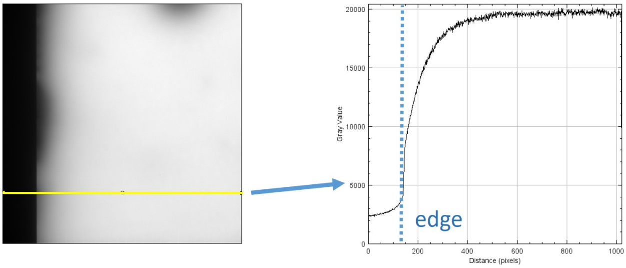

Figure 3.9: From a PL image (left) to a cross section PL profile (right).

of wafers, including wafer edges. Edge recombination can be studied effectively with this tool. PL has been used to characterize edge recombination losses at ISC and other research institutes [153–155]. This PL system consists of the following components:

- Silicon charge-coupled device (CCD) with the cooling system.
- Macro lens with a GaAs filter, resolution up to 1024 × 1024 pixels.
- Two 30-watt lasers with the wavelength of 808 nm as the optical excitation source.

The system is capable of taking high-resolution PL images in a matter of seconds.

By using the high-resolution PL images, one can inspect the PL profile from well passivated areas to the wafer edge. Passivation or recombination quality is indicated by the PL profile curve. Figure 3.9 illustrates an example of how a PL image is converted to a cross-sectional PL profile by examining the image's cross-sectional profile. The resulting PL profile indicates a decrease in passivation quality from the wafer center to the wafer edge. To minimize measurement errors, two approaches are employed. a) Either multiple curves or average curves of an area are analyzed to eliminate low lifetime areas that may be caused by wafer or process defects. b) To mitigate the effects of varying life-

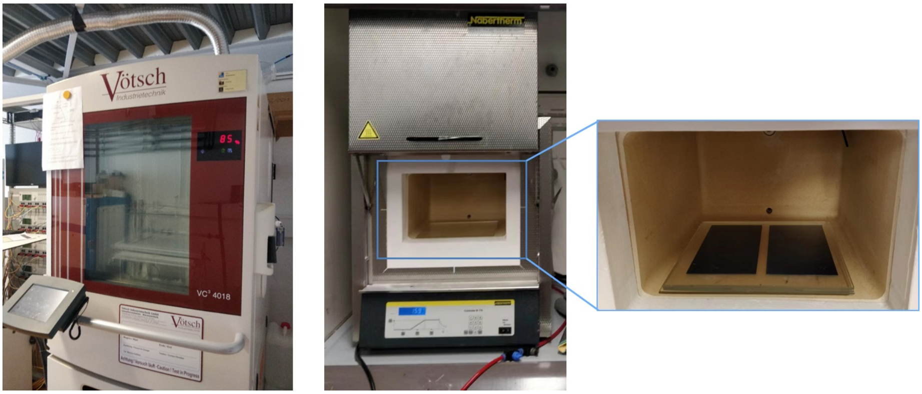

Figure 3.10: Damp heat chamber (left) and muffle oven (middle) used in this thesis for reliability testing. In the muffle oven, the cells are separated by glass to allow multiple samples to be placed in the oven.

times from sample to sample, a normalized PL curve (PL counts divided by maximum PL counts) is used.

3.3.3. Reliability tests

Tests are conducted according to IEC-61215, including damp heat (DH) and thermal cycling (TC). It is important to note that the reliability tests according to the standard module qualification do not imply the module's lifetime. There is a need for extended or additional tests. In this thesis, additional tests was conducted to assess the stability of solar cells under thermal stress. A muffle oven was used for the tests.

Figure 3.10 illustrates the damp heat chamber (from Vötsch Industrietechnik) and muffle oven (from Nabertherm GmbH) used in the study. The damp heat test was conducted at 85 °C, 85% relative humidity, and the thermal stress test was conducted at temperatures ranging from 150 to 250 °C. Cell samples are separated by glass when they are placed in the oven for the thermal stress test. By using this method, a greater number of samples can be tested than by using other methods (for instance, a hotplate). The oven is connected to a N_2 supply. During the thermal stress test, N_2 was turned on in order to minimize oxidation of copper metallization.

Other characterizations, such as spectral response measurement, laser scanning microscopy, and thermal cycling tests were used throughout this thesis. A list of ISC equipment specifications can be found at [156].

4

Mitigating cut losses in IBC solar cells [*]

Abstract

The edge recombination losses of crystalline silicon solar cells become significant when they are cut into smaller pieces to be assembled into modules. With the interdigitated pattern of doped p and n regions on the rear side, interdigitated back contact solar cells (IBC) can be cut through different doped regions. In this chapter, the cutting losses in IBC solar cells are investigated and various cutting scenarios are studied. Through simulations and experimental measurements, it is found that the cut losses can be reduced by cutting through the back surface field rather than through the emitter. The losses under low light intensity are reduced to an even greater extent. When a 23% cell is cut into $1/3$ pieces, the efficiency can be increased by $1.2\%_{\text{rel}}$ (cut related losses were improved from $2.0\%_{\text{rel}}$ to $0.8\%_{\text{rel}}$) under standard 1-sun testing conditions, compared to cutting through the emitter. Under a low light intensity of 0.25-sun, the improvement is around $2.4\%_{\text{rel}}$. The improvement is mainly due to lower FF losses in the IV characteristics and this is further confirmed by Suns-V_{oc} and PL measurements. In the pFF analysis, the additional losses due to laser damage were also observed. This strategy of cutting through the BSF region in IBC solar cells can be quickly adopted in mass production without the need for additional processes or equipment, and both module power and energy yield can be increased.

---

[*] This chapter is based on the following publication: **N. Chen**, F. Buchholz, D. D. Tune, O. Isabella, and V. D. Mihailetchi, *Mitigating Cut Losses in Interdigitated Back Contact Solar Cells*, IEEE Journal of Photovoltaics, 12(6), (2022)

4.1. Introduction

The ongoing industry shift to larger wafer sizes makes the use of cut solar cells in modules a necessity to reduce resistive power losses in strings due to the higher current of the larger wafers. In traditional ribbon-connected modules, half-cut cell modules are already the market's mainstay. Using half-cut cells, the module power is improved by reducing series resistance losses [157] [158], and the shading behavior is also improved [159]. As the wafer size increases from 156 mm (M0) to 166 mm (M6), 182 mm (M10), and even to 210 mm (M12), triple-cut cell modules show benefits in terms of both power and efficiency [160]. In the case of modules that use new interconnection technologies, such as shingles, which use small cell stripes that overlap each other, full cells are generally cut into five, six or more pieces[161]. However, the cutting process introduces additional recombination channels, resulting in a loss of efficiency. In industry, laser cut and cleave (L&C) methods are typically used to cut cells. In this process, a laser is used to cut grooves in solar cells, which are then mechanically cleaved [162]. During the high-power laser process, the wafer surface passivation and silicon bulk in the groove are damaged, and the cleaving process furthermore leaves the wafer edge unpassivated. Losses are dependent on the ratio of the length of the cut edges to the cell area, as well as the cutting method. To maximize the benefits of cut-cell technology, it is important to understand the mechanism and extent of losses caused by the cutting process and thus to develop methods for reducing these losses.

Previous studies on cut losses focused mainly on three areas. (1) Improving laser cutting techniques to reduce laser damage. In a study by Eiternick et al. [142], it was reported that thermal laser separation (TLS) can significantly reduce laser damage. According to Kaule et al. [144], the TLS technique also presents an advantage over conventional L&C in terms of mechanical properties. The work of Lelièvre et al. [163] presented a novel ingot cutting methodology in which cells are cleaved according to their crystallographic planes without introducing laser damage. (2) The cutting of various cell structures was also extensively studied, including passivated emitter and rear contact (PERC) [164], n-type passivated emitter rear totally diffused (n-PERT) [165] and silicon heterojunction (SHJ) [166] solar cells. In particular, Baliozian et al. [167] compared the cutting losses in SHJ and PERC cells. In contrast to PERC cells, high efficiency solar cells like SHJ cells, which have a high V_{oc}, result in higher losses. (3) Different strategies for mitigating cut losses have also been extensively investigated. It is possible to re-passivate the cut edges by adding an additional layer of passivation [164, 168, 169]. Another promising approach is to introduce a specific pattern at the cell edge by using emitter windows or similar [170–172], or using laser doping [173].

However, to our knowledge, there are very few studies on cut losses of large-area interdigitated back-contact (IBC) solar cells. The reason may be that the use of cut cells in IBC modules is relatively new. Most commercial IBC modules, for example as sold by SunPower/Maxeon and LG, are still using the full cell design, while half-cut IBC cell modules have only been available in mass production recently [174]. To reduce the cut losses using the solutions from previous reports would require additional processes and/or equipment that would be challenging to implement in mass production.

In contrast, this paper presents a new strategy that can be easily and immediately implemented in mass production, and is derived from a detailed study of cut losses in

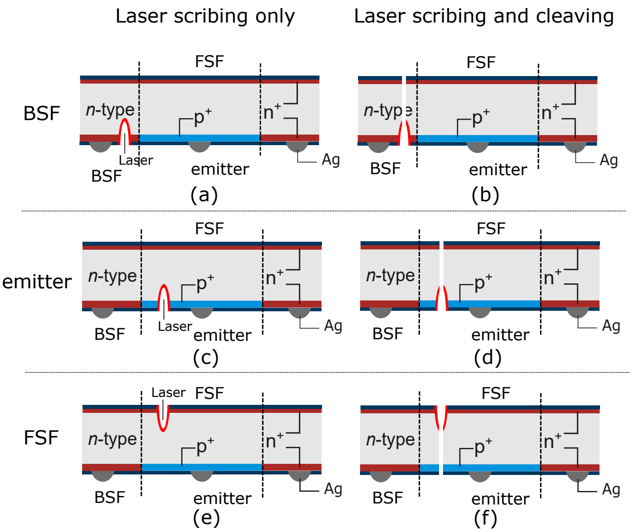

Figure 4.1: Schematic structure (not to scale) of cells with different cutting scenarios. BSF group: (a) and (b), cut on BSF and cleaved through BSF region; emitter group: (c) and (d), cut on emitter and cleaved through emitter region; FSF group: (e) and (f), cut on FSF and cleaved through emitter region.

large-area IBC solar cells, and the cell concept based on our commercially available IBC ZEBRA cell [174]. To evaluate the various cutting scenarios and reduce losses, various simulations and experiments were conducted. The results allow us to propose the new method for effectively reducing recombination losses at the cut edges of IBC solar cells without the need for additional equipment or procedures.

4.2. Experimental details

4.2.1. IBC solar cell cutting scenarios and sample preparation

In standard front- and back-contacted cells, laser cutting and subsequent cleaving inevitably occur through the emitter region, which extends over the entire surface. In contrast, the main feature of IBC solar cells is the interdigitation of the emitter and the back surface field (BSF) regions on the rear of the cells, meaning that they can easily be designed to avoid a cut through the emitter region. Figure 4.1 illustrates the different cutting scenarios for IBC solar cells. The left column represents the laser scribing process, and the right column represents the laser scribing and additional cleaving processes. The groups are named BSF, emitter, and FSF (front surface field). BSF group: (a) and (b), cut on BSF and cleaved through the BSF region; emitter group: (c) and (d), cut on emitter and cleaved through emitter region; FSF group: (e) and (f), cut on FSF and cleaved through emitter region.

Two objectives can be achieved by comparing the different cutting scenarios:

- By comparing the emitter and BSF groups, the losses due to cutting through either the BSF and emitter region can be determined.

- By comparing the emitter and FSF groups, the role of laser damage in cutting through emitter can be clarified.

In this study, cells were prepared that can be cut from BSF, emitter, and FSF. In addition, to evaluate the cut edge effect on different cell sizes, IBC cells have been designed that can be cut into 1/2, 1/3 and 1/4 sizes. All solar cells have been manufactured in our laboratory following the established ZEBRA baseline procedures [175]. The cells were fabricated on 175 μm thick, n-type M2 (length 156.75 mm, diameter 210 mm) wafers with a base resistivity of 4 ±1 Ω·cm. The FSF/BSF and rear emitter regions are formed in industrial tube diffusion furnaces using $POCl_3$ and BBr_3, respectively, as diffusion sources. A plasma-enhanced chemical vapor deposition (PECVD) mask layer of SiN_x and a 532 nm nanosecond laser were used to form the interdigitated doped regions on the rear side. The passivation and anti-reflection coating (ARC) layers were formed by a stacked layer structure comprising thermal SiO_2 grown $in-situ$ during the diffusion process and capped with SiN_x [98]. Finally, metallization was accomplished using screen-printed three-dimensional metallization patterns comprising busbars, fingers, and isolation layers. The interdigitated pattern on the rear side was designed such that a doped region of either BSF or emitter was left un-metallized at the designated locations for the final laser scribing process to yield the 1/2, 1/3, or 1/4 size cut IBC cells.

Following the cell processing, a laser was used to scribe the cells to a depth of 50 μm, which is approximately 30% of the cell thickness, followed by manually cleaving the cells into 1/2, 1/3, and 1/4 pieces. For this cutting process, a laser with a plus width of 300 femtoseconds (fs) (Rofin, StarFemto FX) was used. It should be emphasized that although the fs laser was used in this study, other laser sources should produce equivalent results based on our prior findings [176].

In total, nine clusters of cells were fabricated, which included cells of various sizes (1/2, 1/3, and 1/4 cells) and different cutting scenarios (cutting from either the BSF, emitter or FSF as indicated in Figure 4.1. In each cluster, there were 11 to 16 cells.

4.2.2. Characterization

The current-voltage (IV) characteristics were measured under standard test conditions (STC) for all solar cells to determine the electrical losses induced by the cutting. The measurements were conducted using a commercial AAA-class solar simulator (h.a.l.m. elektronik GmbH). Prior to measurement, the I_{sc} was calibrated using a secondary calibration cell (Fraunhofer ISE CalLab). The repeatability of the measurement was estimated by repositioning and measuring the same cell 5 times. In the case of a full cell without laser cutting, the repeatability evaluated by standard deviation divided by average value of different parameters is as follows: 0.01% for V_{oc}, 0.08% for J_{sc}, 0.26% for FF, 0.02% for pseudo fill factor (pFF), and 0.26% for power conversion efficiency.

To eliminate the effects of light inhomogeneity and probe contact on the measurement of cut cells, which was also reported previously [166], cut cells were measured as ‘full cells’ in this study (i.e., with all cut cells reassembled on the chuck and measured together with their edges not touching). The repeatability of V_{oc}, J_{sc}, and pFF for cut-cell measurements are similar for 1/2, 1/3, and 1/4 cut cells; however, the FF shows different repeatability because the IV measurement chuck is designed specifically for the measurement of full cells. In terms of repeatability, 1/2 cells are found to be 0.37% for

FF and 0.39% for efficiency. 1/3 cells have a repeatability of 0.18% for FF and 0.16% for efficiency. For 1/4 cells, repeatability is 0.60% for FF and 0.56% for efficiency.

During the IV measurement, the series-resistance-free Suns-V_{oc} curve was measured under a light intensity of 1000 W/m^2. The pFF was extracted from the Suns-V_{oc} curve [177] and was used to further analyze the edge recombination losses without the effect of series resistance [167]. pFF was tested at different stages: before laser scribing, after laser scribing without cleaving, and after cleaving. pFF was studied specifically for the BSF and emitter groups in order to distinguish the laser effects from different sides. In addition to STC with 1-sun irradiance, a low light intensity test with 0.25-sun irradiance was also conducted. The 0.25-sun irradiance was chosen because of the lowest level achievable in our solar simulator and as a practical limit for which the energy yield of solar modules is still significant. The low light performance is particularly important since edge recombination increases with a decrease in light intensity [171], [178]. The low light performance of solar modules is critical for the energy yield [179], especially for places that experience lower annual irradiance due to geographical and/or seasonal factors.

It has been demonstrated that photoluminescence (PL) characterization is useful in evaluating edge recombination [180], [153]. To validate the electrical measurement, PL measurements were performed on the final cut cells as part of characterization. For the measurement, cells with median FF and efficiency from each group were chosen. Our in-house built PL imaging system was used along with a macro lens to check the PL images of the cut edges, with the same settings as used in the previous study [176]. For cross-sectional analysis of the cut regions, a laser microscope (Olympus) was used.

4.2.3. Simulation

Quokka3 was used for solar cell simulation, with parameters based on a 23% ZEBRA cell. To speed up the simulation, a unit cell was used rather than a full cell. Different cell sizes were simulated in 3D, taking into account the dimensions of M2 cells and cutting the cells into 1/2, 1/3, 1/4, and 1/8. Among the cells, half-cut cells were simulated with a single cut edge, 1/3 and smaller cut cells were simulated with one cut edge and two cut edges.

In response to cutting through the BSF and emitter regions, two edge structure scenarios were simulated, with either the BSF or emitter situated at the edges. There are two key parameters of the recombination edges [181]: a high surface recombination velocity value (applicable to all unpassivated edges) of 1.0×10^7 cm/s (e.g. BSF, FSF, and quasi-neutral bulk regions) and, if the emitter is cut through, an additional J_{02} emitter recombination current that is assumed to be 19 nA/cm^2 (representing a “worst-case” scenario assuming a clean but not passivated space-charge region (SCR) recombination surface). In the simulation, the additional damage caused by the laser is not taken into account. Similar to the experimental part, the IV characteristics were simulated under both 1-sun and 0.25-sun irradiance conditions.

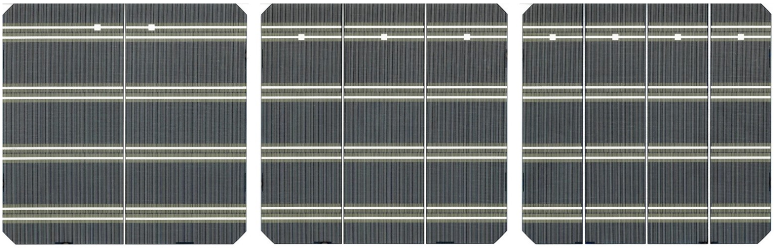

Figure 4.2: Photographs of the rear side of solar cells fabricated in this study. Left to right: 1/2, 1/3, and 1/4 cells.

Table 4.1: Summary of IV Results before laser cutting

Group	Cut	V_{oc} (mV)	J_{sc}(mA/cm^2)	FF (%)	η (%)
1/2-cell	FSF	689.6 ±1.8	41.23 ±0.07	80.09 ±0.34	22.77 ±0.16
	emitter	690.2 ±1.1	41.25 ±0.06	80.10 ±0.32	22.81 ±0.13
	BSF	690.2 ±1.2	41.23 ±0.05	80.11 ±0.28	22.80 ±0.10
1/3-cell	FSF	691.1 ±1.6	41.33 ±0.06	79.78 ±0.32	22.79 ±0.13
	emitter	691.9 ±0.8	41.34 ±0.06	79.77 ±0.36	22.82 ±0.11
	BSF	690.9 ±1.2	41.27 ±0.07	79.55 ±0.26	22.68 ±0.14
1/4-cell	FSF	691.2 ±0.9	41.31 ±0.04	80.54 ±0.37	23.00 ±0.12
	emitter	691.0 ±0.7	41.30 ±0.05	80.44 ±0.36	22.96 ±0.09
	BSF	691.0 ±0.9	41.30 ±0.05	80.30 ±0.39	22.92 ±0.14

4.3. Results and discussion

Figure 4.2 shows the rear side of the IBC cells fabricated in this study. As stated in section 3, the solar cells were first processed as a whole and then laser-cut and cleaved into 1/2, 1/3, and 1/4 pieces in the BSF, emitter, or FSF cutting scenarios.

To assess edge recombination on various cut-cell sizes, the cut edge-to-area aspect ratio (AR) defined by Glunz et al. [171] was used:

$$AR = \frac{Laser\ cut\ edge\ length}{Solar\ Cell\ Area}. \tag{4.1}$$

In this study, each cut groove creates two laser cut borders, so the laser cut edge length is equal to two times the laser cut number multiplied by the edge length. As examples, the AR of 1/2 cut M2 cells is approximately 0.13 cm^{-1} ; 0.26 cm^{-1} for 1/3 cells, 0.39 cm^{-1} for 1/4 cells, and 0.90 cm^{-1} for 1/8 cells, respectively. With this definition of AR, it is possible to extend the findings to other cell sizes, not just the sizes used in this study.

4.3.1. Effect of edge recombination at 1-sun intensity

Solar cells are comparable in terms of their IV characteristics prior to laser cutting. Table 4.1 summarizes the IV characteristics of each group. Each group contains 11 to 16 cells.

In contrast, as shown in Figure 4.3 and Figure 4.4, following laser cutting and cleaving, the cells from different groups exhibit different losses, particularly for the group cut-

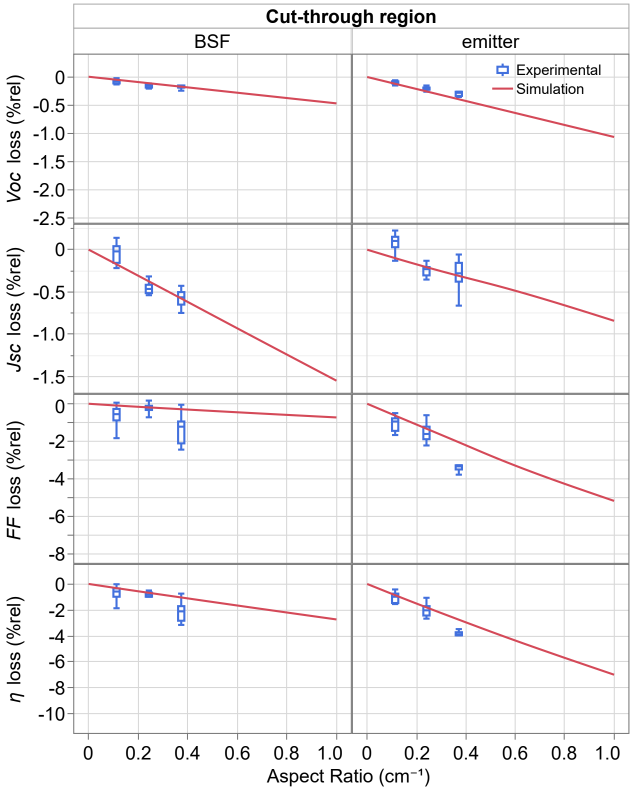

Figure 4.3: Relative losses of V_{oc}, J_{sc}, FF and efficiency (η) as a function of AR and cut-through region, under 1-sun irradiance.

ting through emitter and the group cutting through BSF.

The experimental mean values of relative losses in main cell parameters are plotted in Figure 4.3 (symbols) together with the simulated values (lines) as a function of AR and cut region under 1-sun irradiance. The simulated and experimental results agree well for V_{oc} and J_{sc} and the data shows that the relative V_{oc} losses are minor. For the 1/4 cells ($AR = 0.39$ cm^{-1}) cut through the BSF region, an absolute V_{oc} loss of 1.3 mV corresponds to only a 0.20%$_{\text{rel}}$ loss but the losses in the emitter-cut group are slightly higher at around 0.35%$_{\text{rel}}$. J_{sc} losses are likewise insignificant. When cut to 1/4 size or smaller, the emitter-cut samples perform marginally better in J_{sc} than the BSF-cut samples, which demonstrates a good current collection on the emitter-cut samples.

Most of the cut losses can be attributed to losses in the FF. In both simulations and experiments, the losses in the emitter-cut samples are larger than those of the BSF-cut samples, as the difference increases with the AR. This shows that edge recombination losses are reduced when cutting through the BSF rather than cutting through the emitter. The higher FF losses observed in the experimental data, in comparison to the simulation, may be due to additional series resistance introduced by the measurement chuck unit, which has been reported previously [144]. A second reason is that the measure-

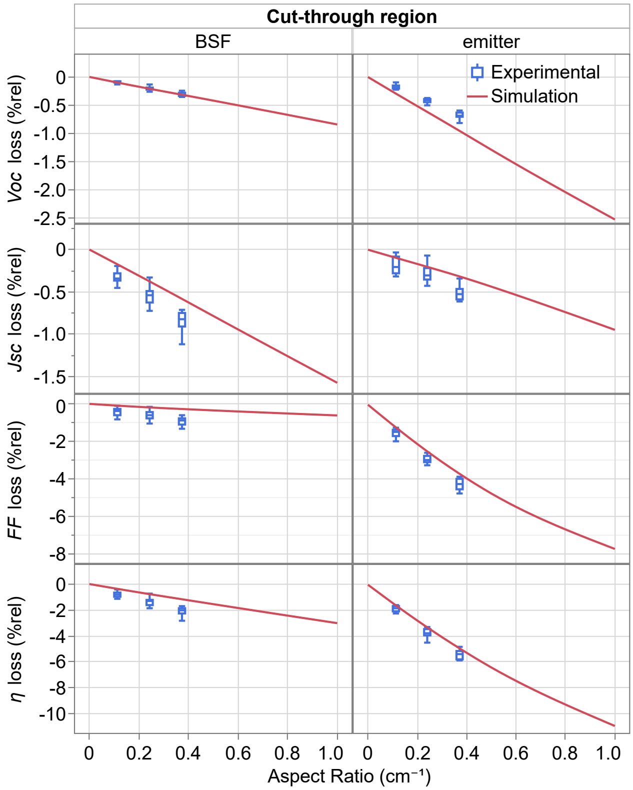

Figure 4.4: Relative losses of V_{oc}, J_{sc}, FF and efficiency (η) as a function of AR and cut-through region, under 0.25-sun irradiance.

ment uncertainty of FF is high, particularly when measuring the 1/4 cells as discussed in section II (B).

Overall, the BSF-cut group exhibits lower efficiency losses than the emitter-cut group, both in experiment and simulation, and this is mostly due to lower FF losses. In the following discussions, losses are expressed as a relative percentage of the original value (e.g., J_{sc}) and differences in losses between different samples are also given. So, cutting through the BSF region rather than the emitter region reduces cut losses by 1.2%$_{\text{rel}}$ for 1/3 cells (i.e., 2.0%$_{\text{rel}}$ for emitter-cut vs. 0.8%$_{\text{rel}}$ for BSF-cut).

4.3.2. Effect of edge recombination at 0.25-sun intensity

Figure 4.4 shows the relative IV losses measured at 0.25-sun irradiance, showing similar trends to those obtained under 1-sun irradiance for BSF group. In the emitter group, V_{oc} and FF losses are greater under 0.25-sun than under 1-sun, while J_{sc} losses remain the same. Therefore, the efficiency gap between the BSF and emitter groups is wider. Thus, the BSF group has gained an advantage of 2.4%$_{\text{rel}}$ vs. the emitter group for the 1/3 cut cells, both in simulation and in experiments.

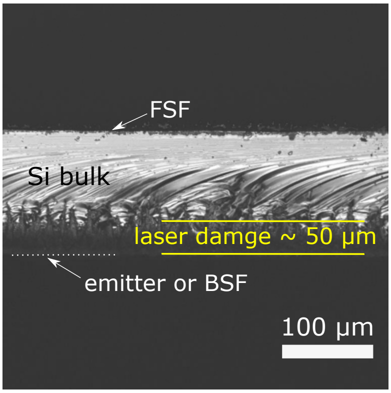

Figure 4.5: Cross-section of the laser cutting area

4.3.3. Effect of laser damages

As shown in Figure 4.5, the depth of the laser scribe is 50 μm, which is approximately 30% of the wafer thickness. The laser damage thus penetrated through passivation and diffused layers, either emitter, BSF, or FSF, which are typically less than 1 μm. Cleaving damage accounts for 70% of the wafer thickness and comprises unpassivated quasi-neutral bulk edge as well as emitter/SCR or BSF/$n+$ regions.

To further clarify the laser damage losses, the pFF losses for the emitter and FSF groups were analyzed. As shown previously, laser damage can occur on either the FSF or the emitter side for the emitter-cut samples. The two groups were measured at different stages. First, before laser scribing without damage; then, after laser scribing without cleaving (with only laser damage) and, finally, after laser scribing and cleaving (with both laser damage and cleaving damage). The pFF loss statistics are depicted in Figure 4.6. A large distribution of data can be seen in the Figure, mainly due to measurement uncertainty introduced by the measurement chuck. The chuck used for Suns-V_{oc} was specially designed for full cell measurement. When cut cells are used, measurement uncertainty increases. However, as we have more than 10 samples in each group, the pFF loss can be still analysed. Trends are clearly visible as shown in Figure 4.6.

In the FSF group, around 30% to 40% of the pFF loss occurred due to laser damage on the FSF, which is above the laser damage rate of 30%. The main losses in pFF occurred after the FSF-cut wafer had been cleaved. In contrast, for the emitter group, in which there is laser damage directly on emitter/SCR, most pFF losses already occurred after laser scribe, with only slight additional pFF losses after cleaving through the bulk and BSF region. In both groups, the pFF losses due to the exposed SCR regions [182] are clearly observed.

Compared to the pFF losses after cleaving, the FSF group exhibits similar but still lower losses than the emitter group. It was difficult to distinguish the differences between the two groups when cut into 1/2 cells. When the AR is higher, however, the difference between the two groups becomes statistically relevant. A linear fit to the pFF losses in the Figure 4.6 was applied to show more clearly the laser damage to the SCR regions. These results clearly indicate that laser damage to the emitter region should be

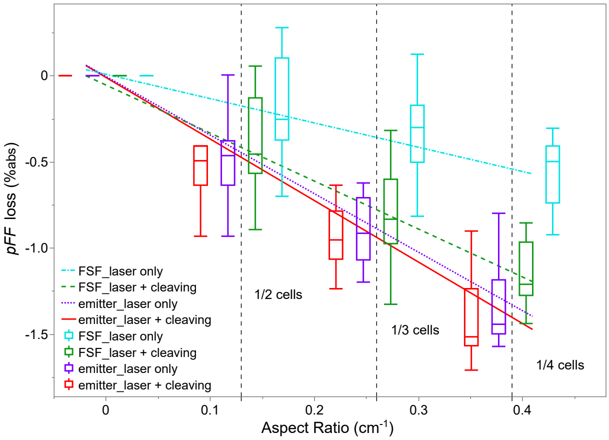

Figure 4.6: Solar cell pFF losses due to cutting from emitter and FSF sides, as a function of AR. The lines are linear fits of the data. The AR corresponding to the cut cell size (1/2, 1/3 or 1/4 cells) is labeled accordingly, and the box plots are with offset from their original positions in order to be distinguished from each other.

avoided during solar cell cutting.

Similarly, researchers have compared the difference between front emitter and rear BSF (similarly to FSF cut in our study) cuts on p-PERC and n-PERT cells [183] [165]. In the report from Xia et al.[165], FF losses were reported (no pFF loss was reported). On half-cut n-PERT cells, FF losses were 1.62%$_{\text{rel}}$ when cut on emitter, and 0.55%$_{\text{rel}}$ when cut on BSF. Münzer et al.[183], reported laser scribe on front emitter reduced pFF by 7.5%$_{\text{abs}}$, when using the L&C technique (M2 PERC cells, cut to 22 mm strips, $AR = 0.9$). When using TLS, pFF losses were similar between the two. In our study, we only performed L&C cuts. We found that IBC cells have lower pFF losses even when the emitter is cut. There is also a relatively smaller difference between emitter and FSF cuts. In comparison with previous studies, the differences can be explained by both cell structure and laser cutting techniques. It is generally agreed that laser damage to the emitter region should be avoided during the cutting of solar cells.

4.3.4. PL characterization of the cut edges

Figure 4.7 shows the high-resolution PL images and their corresponding profiles measured with 1-sun equivalent illumination intensity. Cells with median FF and efficiency were selected from each group and measured with PL after laser scribing and cleaving. The line where the laser cut and cleave was applied is in the center of the image, thus showing the left and right cell piece after separation placed next to each other. The PL profiles clearly demonstrate the advantage of cutting from BSF rather than the emitter/FSF, with a steeper profile from the laser cut edge (plot of 0 mm position) to the cell center. Slight differences are also apparent between the FSF-cut and emitter-cut samples. The PL results support the findings of the IV and pFF results and further demonstrate that high-resolution PL imaging is a useful tool for qualitatively comparing edge recombination, even at the cell level.

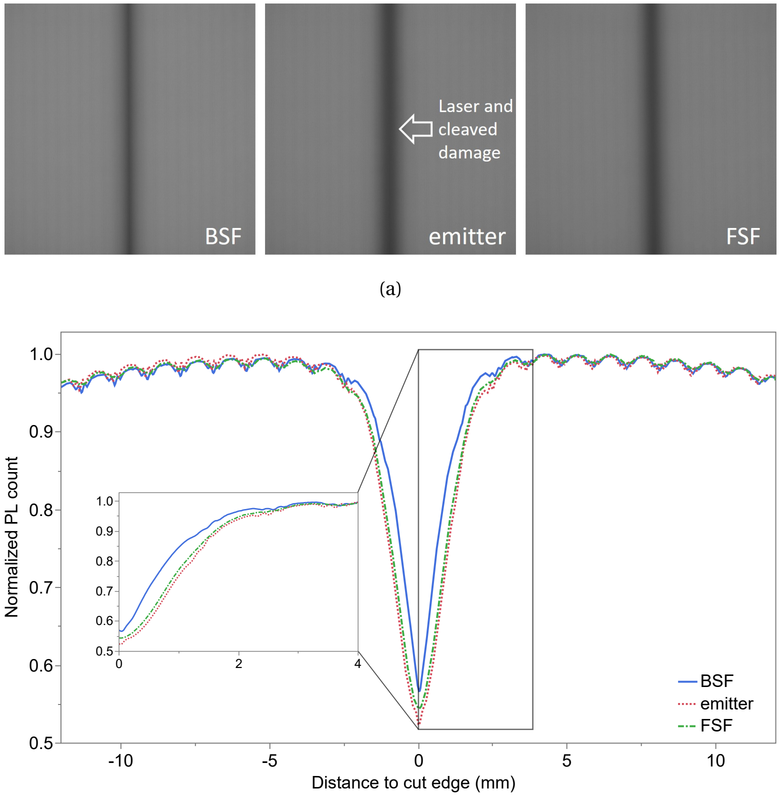

(a)

(b)

Figure 4.7: (a) Photoluminescence images of the laser-cut regions after laser cut and cleaving, with the same scaling. From left to right: BSF, emitter and FSF. (b) Cross-section of PL profiles from the cell edge.

4.3.5. Application on modules

From the results, it is clear that cutting through the emitter-free BSF regions results in a significant reduction in edge recombination compared to cutting through the emitter. These findings are applicable to all cell concepts based on c-Si. However, implementation of the necessary emitter-free cutting regions in a both-sides-contacted cell concept such as PERC, SHJ, or TOPCon (Tunnel Oxide Passivated Contact) would require additional process steps for creating the so-called emitter window. The IBC concept thus has an inherent advantage in that its doping structures can be designed to avoid emitter cuts without any additional process steps.

The power gains observed on cell level by cutting through the BSF rather than the emitter can be transferred to modules. In this case, both the module power and energy yield are predicted to increase.

In both simulations and experiments, cutting through the BSF results in efficiency losses of $1\%_{\mathrm{rel}}$ or less under 1-sun irradiance for 1/2 and 1/3 cut cells. These losses are small and are comparable to those measured on PERC cells [158], confirming that IBC cells can be used for cut-cell modules without additional losses vs. similar PERC modules. In the case of a 72-cell M10 module (typically used for power plants) cut into 1/3 cells, the cut losses are reduced by ~$1.2\%_{\mathrm{rel}}$ or 6.6 W when comparing BSF and emitter cut. For the lower light intensity of 0.25-sun irradiance, the relative efficiency losses improvement by cutting through the BSF instead of the emitter is higher. For the same 72-cell M10 module with BSF cutting, the cut losses are reduced by $2.4\%_{\mathrm{rel}}$ or 3.3 W compared to the module power of around 136 W. As a result of better low light performance, the energy yield can be improved.

4.4. Conclusion

An important feature of the IBC solar cell concept is that its doping regions can be designed such that cutting of the cells before module assembly can be done exclusively through either the BSF or the emitter regions. In this paper, different cutting scenarios for large-area IBC solar cells were compared using simulations and experiments. The results clearly show that cutting through the BSF reduces both FF and efficiency losses compared to cutting through the emitter. Compared to the simulations, higher losses were observed from measurements due to FF effects are explained, however, the difference in losses between emitter-cut and BSF-cut samples was the same in both simulation and experimental results. Under 1-sun illumination, the measurements of BSF-cut samples showed up to $1.2\%_{\mathrm{rel}}$ reduction in cut losses compared to emitter-cut samples. This reduced the power loss by 6.6 W for a simulated 72-cell M10 module when using 1/3 cut cells. The benefit increases for smaller cell fractions and lower light intensity. In the case of 0.25-sun irradiance, the difference between BSF-cut and emitter-cut is around $2.4\%_{\mathrm{rel}}$. Further investigation reveals that the main pFF losses on the samples cut through the emitter are due to the exposed space charge region, and that laser damage to the emitter was revealed from linear fitted curves. High-resolution PL measurements also confirmed the IV and pFF results.

The strategy presented in this work can significantly contribute to reducing cut losses in IBC cells and modules and markedly enhancing their low-light performance and energy yield. Moreover, this strategy can be easily applied in mass production of IBC cells without the need for additional equipment or processes.

5

Edge passivation using Nafion polymer [*]

Abstract

In this study, the edge passivation effectiveness and long-term stability of Nafion polymer in n-type IBC solar cells are investigated. In wafer-based crystalline silicon solar cells, edge passivation is usually less effective than surface passivation. For new module technologies such as half-cut, triple-cut, or shingled modules, cutting of the cells introduces unpassivated edges with a high recombination rate and this limits the module power. These cut edges can be "repassivated" after laser cutting and in this work Nafion polymer is used to achieve this. First, different edge types, namely emitter edges (n+/n/p+) and back surface field (BSF) edges (n+/n/n+), as well as different cutting techniques such as laser cut and cleave (L&C), thermal laser separation (TLS), and mechanical cleaving along the crystal orientation are evaluated. It is found that TLS and mechanical cleaving enable good repassivation on both BSF and emitter edges. Second, industrial-size IBC solar cells are made to assess the effect of the edge repassivation on performance. On 1/4-cut M2 size IBC cells with two emitter edges, efficiency is improved by over $0.3\%_{\text{abs}}$. However, efficiency improvement is not observed for similar cells with BSF edges, due to an insufficient passivation at the bulk edges. Last, the real-world stability of the Nafion repassivation is evaluated in industrially relevant module stacks by laminating the repassivated wafers with ethylvinylacetate (EVA) or polyolefin elastomer (POE) encapsulants and then exposing them to industry standard testing of 1000 hours under damp heat conditions (85 °C, 85% relative humidity). The tests reveal that the repassivation is stable in EVA encapsulants but not in POE.

---

[*] This chapter is based on the following publication: **N. Chen**, D. Tune, F. Buchholz, R. Roescu, M. Zeman, O. Isabella, and V. D. Mihailetchi, *Stable passivation of cut edges in encapsulated n-type silicon solar cells using Nafion polymer*, Solar Energy Materials and Solar Cells, 258, (2023)

5.1. Introduction

The passivation of silicon solar cells has been continuously developed for many years and the combination of advanced cell structures with different passivation materials has been key to boosting the conversion efficiency. Since aluminum back surface field (Al-BSF) solar cells were introduced, the front n+ emitter in p-type silicon solar cells has been well passivated with SiN_x. Likewise, on passivated emitter and rear cells (PERC), the rear side is well passivated with Al_2O_3 [184]. Passivation strategies have also been developed for metal contact areas and these are commonly used in n-type solar cells. Examples include tunnel oxide passivated contacts (TOPCon) cells, where the passivation is based on polysilicon/SiO_x structures [185], and silicon heterojunction (SHJ) solar cells based on the passivation of amorphous silicon [186]. In contrast, edge passivation is generally less effective than surface passivation. However, the edges also play a significant role in the efficiency of solar cells. For traditional Al-BSF cells, Wong et al. state that "there can be ~0.25% – 0.6% absolute efficiency gain if the peripheral and edge recombination sources are eliminated" [187]. PERC cells show better edge passivation than Al-BSF cells, with edge recombination losses up to $0.2\%_{\text{abs}}$ for a 21% efficient M0 size (156 mm × 156 mm) cell [188]. The TOPCon cell concept has an edge recombination loss of $0.5\%_{\text{abs}}$ based on the modeling of an M0 cell with a full edge recombination and without edge recombination [181]. The SHJ cells suffer edge recombination losses due to both imperfect edge passivation and the transparent conductive oxide (TCO) gap that prevents short circuits from front to back [189]. Advanced module technologies such as half-cut, triple-cut, or shingled modules can provide significant increases in module power. However, the cutting and/or cleaving processes introduce new unpassivated edges which cause additional edge recombination and reduce the efficiency potential. For high-efficiency solar cells such as TOPCon and SHJ cells, edge recombination has a greater effect on absolute efficiency losses after cutting than for lower efficiency PERC cells. When the cell area becomes small with a high edge-to-area ratio, the edge recombination effects become more severe.

The traditional industrial solution for edge treatment focuses primarily on isolation of the edge [45]. Edge passivation is mainly achieved as a beneficial side effect of the surface passivation process of a solar cell and there is no cost-effective industrial solution for passivating just the cut edges of half, triple or shingled cells. In the lab, researchers have developed several small-scale solutions, including:

- Partially passivating the edges during front-end processes [173, 190].
- Creating a structure to avoid cutting through the emitter region. For example, the emitter window approach or similar [170, 172], or simply cutting through BSF regions for interdigitated back contact (IBC) solar cells [191].
- Using advanced cutting methods to reduce laser damage. Mechanical damage can be reduced using thermal laser separation (TLS) [144, 192], and module power gains have been reported [145]. Another method is to cleave without causing any laser damage to the edge. For this, the wafers should be cut from the ingot such that the crystal orientation is parallel to the wafer edges [163].

- Passivating the edge using Al_2O_3 after laser cutting, namely “Passivated Edge Technology” [168]. Using this technique, very good passivation has been achieved on both PERC and SHJ cells [143, 164, 168, 169].

Among the methods, the Al_2O_3 passivation method has great potential to become a standard process for industry. However, there are still bottlenecks to overcome. For example, the Al_2O_3 is usually deposited under vacuum and in heated conditions, and post annealing or thermal treatment is needed to activate the passivation.

As an alternative, it is possible to use the very strong field effect passivation provided by certain Lewis acid organic polymer thin films, especially the so-called superacids. After the first reports of silicon surface passivation from Biro and Warta in 1998-2002 [193, 194], this technique has been attracting significant renewed interest in recent years, starting with the 2016 reports of Bullock et al. [195] and Hossain et al. [196] and continuing through a growing number of other works [197–202]. Compared to other methods of silicon surface passivation, these organic polymer films have the advantage that they can be deposited at room temperature using non-vacuum processes such as spin-, dip-, spray- or slot-die coating. Of the various superacids studied, Nafion (sulfonated tetrafluoroethylene) is particularly promising for industrial application due to its relatively low reactivity and thus stability potential. Recently, we extended the application of Nafion passivation to the edges of laser-cut silicon solar cells and demonstrated the critical importance of the morphology of the edge surface, whether laser damaged or cleanly cleaved, in determining the extend of edge passivation achievable through this technique [153, 176]. Similarly, Li et al. used Nafion edge passivation on a 9 cm^2 SHJ cell, showing a V_{oc} improvement of 8 mV, and an improvement of 1-2$\%_{\mathrm{abs}}$ in efficiency [203], while Chen et al. showed that an alkaline etching and cleaning procedure can improve the edge passivation by removing laser damage [204].

In this work, we further extend the Nafion edge passivation concept through a systematic study on industrial size n-type silicon solar cells. The edge passivation is applied on the newly cut or cleaved edges to recover partly the cut losses, which is also referred to as edge repassivation hereafter. Different types of industrially relevant cut edges were evaluated, including emitter edges (n+/n/p+) and BSF edges (n+/n/n+), as well as different cutting techniques. The edge repassivation was tested on n-type IBC solar cells and electrical parameters were compared before and after repassivation. Importantly for commercial application, we show for the first time that the Nafion passivation can withstand the accelerated damp heat testing regime of the IEC 61215 industrial qualification standard for photovoltaic modules when the modules are manufactured using a standard industrial bill of materials.

5.2. Experimental details

5.2.1. Lifetime and solar cell samples

M2 (156.75 mm × 156.75 mm) n-type Czochralski (CZ) (100) oriented wafers, with a thickness of 175 µm and a base resistivity of 4 ±1 Ω·cm were used as lifetime test structures as well as solar cell samples. All wafers were saw damage etched in a KOH solution and cleaned in a piranha solution. The emitter edge samples were doped using BBr_3 and $POCl_3$ diffusion, respectively. The BSF edges samples were first textured in a KOH bath

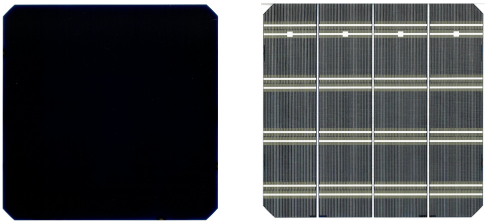

Figure 5.1: Images of a solar cell fabricated for edge passivation evaluation. The left image is the front side of a cell. The right image is the rear side of a cell, and the cell was cut into 1/4 sizes through the gaps.

with a texture additive, and then double-sided diffused with $POCl_3$. Solar cells were fabricated using our best-known method (BKM) described previously [103, 205]. One of the features is that the passivation layer was in-situ grown SiO_2 and then capped with SiN_x [98].

The IBC cells were designed to be cut into 1/4 sizes through either the emitter or BSF regions [191], and the images are shown in Figure 5.1. The lifetime samples were cut into 4 mm × 4 mm. Different methods were used to cut the edges, including 1) TLS cut, using an industrial tool (3D-Micromac); 2) Laser cut and cleave (L&C) using a nanosecond laser with a laser damage depth around 80 μm (F20, InnoLas); 3) Cleaving was done manually. After scribing the wafer edge with a diamond pen, the wafer edge was manually cleaved to a 45° angle.

5.2.2. Edge passivation using Nafion

Nafion perfluorinated resin solution, 5wt.% in mixture of lower aliphatic alcohols and water, contains 15-20% water, from Sigma-Aldrich was used in the study. To remove native oxide from the wafer edges, the wafer edges were dipped into 5vol.% HF for 10 seconds followed by a DI water rinse and N_2 blow drying.

Passivation was achieved by dipping the cell edges in Nafion solution for 10 seconds, followed by N_2 blow drying. In the case of solar cell repassivation, two groups of solar cells were also tested with and without HF cleaning before Nafion, to check whether the HF cleaning can be skipped (to avoid HF corrosion to solar cells). The edge of the cell was dipped into Nafion solution and then dried with N_2. The process flow of edge repassivation on solar cells is shown in Figure 5.2.

5.2.3. PL and IV characterizations

Photoluminescence (PL) and IV were measured for the samples to evaluate the edge passivation. The PL was measured using a custom-built PL system (ISC Konstanz), integrated with a macro lens described in a previous publication [176]. A Class AAA xenon flasher (Halm Elektronik) was used for IV characterization under standard test conditions. A measurement chuck, based on printed circuit board technology, was specifically designed for back contact cells.

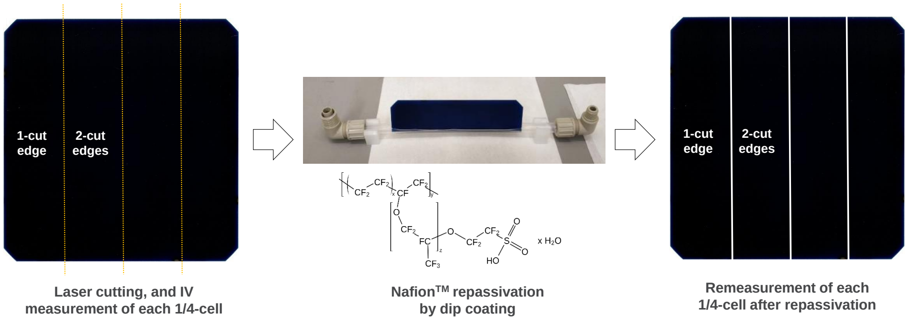

Figure 5.2: Process flow of edge repassivation on solar cells. M2 size IBC solar cells were cut into 1/4 sizes; then repassivated by Nafion using dip coating.

5.2.4. Encapsulated samples and damp heat tests

The wafer samples were laminated in a solar module laminator (Phototrade - P. Energy). Module structure comprises 2 mm thick glass and transparent backsheet (Dunmore DS450). In the case of EVA, the lamination temperature is 145 °C, and the lamination time is 10 min; the lamination temperature for POE is 150 °C, and the lamination time is 13 min. The damp heat test was conducted in a climate chamber (Vötsch) at 85 °C, 85% relative humidity for 1000 hours in accordance with IEC 61215. The PL was measured at various intervals during the test, including before lamination, after lamination, at DH 0 h, 25 h, 100 h, 260 h, 500 h, 785 h, and 1000 h.

5.3. Results and discussion

5.3.1. Nafion passivation of the different edges

PL is a useful tool for qualitative lifetime analysis of wafers as well as the passivation of their edges [155, 206]. A high-resolution PL imaging technique was used in this study for the evaluation of edge passivation [153] and both lifetime samples and solar cells can be quickly evaluated using this technique. Lifetime samples were prepared to represent different types of edges and cutting methods of n-type cells. Based on the cell structure, there can be two types of wafer edges, emitter edges (n+/n/p+) and BSF edges (n+/n/n+). Depending on the application, emitter edges might represent 1) all front and rear contact cells edges when the cut is always through emitter regions or 2) for IBC cells, when the cut is through emitter regions. The BSF edges represent a special case for IBC cells, when the cut is through BSF regions. Additionally, different cutting methods were also evaluated, including TLS, L&C [162], and mechanical cleaving. Four types of edges were included in the test as shown in Figure 5.3:

- (a) Emitter edge (n+/n/p+) with TLS cut;
- (b) Emitter edge (n+/n/p+) with L&C on the n+ side;
- (c) Emitter edge (n+/n/p+) with no laser damage, only cleaving through the emitter regions;

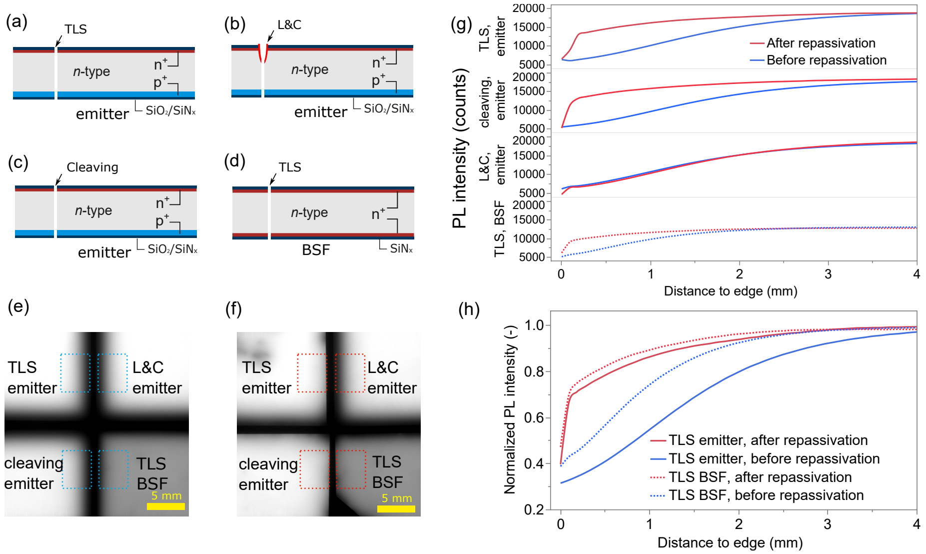

Figure 5.3: Samples for edge repassivation evaluation and results. (a), (b), (c), and (d) are n-type silicon wafer samples with different types of edges; (e) shows PL images of the (a-d) samples before Nafion repassivation while (f) shows PL images of the samples after Nafion repassivation; (g) shows PL intensity profiles of different types of edges before and after repassivation, measured from the square areas marked in (e) and (f); (h) shows normalized PL intensity profiles (measured PL intensity divided by maximum of PL intensity of each curve) of TLS edges before and after repassivation.

- (d) BSF edge (n+/n/n+) with TLS cut.

Qualitative differences in edge repassivation of the four types of samples can be clearly observed in the PL images shown in Figure 5.3. Prior to repassivation (Figure 5.3(e)), all edges appear blurry and indistinct from the black background. However, after repassivation (Figure 5.3(f)) the TLS-cut and the mechanically cleaved edges have become much sharper and are clearly distinguishable from the black background, indicating an improvement in edge passivation.

To better quantify the effect of edge repassivation, the PL intensity of different samples was plotted along a line from the wafer edge (0 mm) towards the center of the wafer up to a distance of 4 mm and the resulting PL intensity profiles are shown in Figure 5.3(g) for each type of cutting process. The blue curves were taken from the PL images before repassivation whereas the red curves from the images after Nafion repassivation. For all samples, the PL signal increases gradually from the edge towards the center of the wafer and saturates at a level limited by bulk and surface passivation (a typical distance of several times the minority carrier diffusion length).

In the case of emitter samples (the upper three plots of Figure 5.3(g), and shown schematically in Figure 5.3(a-c)), the profiles before repassivation are similar. After repassivation, TLS and mechanical cleaving show similar repassivation effectiveness as indicated by identical PL profiles. There was no repassivation on the L&C sample due to severe laser damage to the edge. For repassivation, a smooth cut edge (from either TLS or 45° cleaving) is essential [207]. In the TLS BSF samples (with TLS cut through the n+/n/n+ edge), the initial passivation quality is poor due to the passivation of BSF samples is not as good as that of the emitter samples. A better comparison of repassivation between BSF and emitter samples can be achieved by comparing normalized PL profile curves as shown in Figure 5.3(h). By normalizing the PL profile curves, the initial passivation difference between the two samples can be excluded. From Figure 5.3(h) we observed that the TLS BSF cut edge shows better repassivation than TLS emitter cut edge before repassivation process. Whereas after repassivation the two profiles are similar to each other. A quantitative modelling of edge recombination using Quokka3 tool was previously presented by Fell [181]. This simulation model accounts for the recombination at the edge from the space-charge-region (SCR) of the emitter and the quasi-neutral (qn) bulk of the Si base. Thus, for BSF cut edges, only the qn recombination losses are dominant. For the emitter cut edges, the recombination losses are caused from both SCR and qn regions. Before repassivation, the difference between them was the SCR recombination. Following repassivation, the PL profiles of both edges become similar, indicating a significant reduction in SCR recombination. The repassivation quality of both edges after repassivation is constrained by the qn bulk edge.

5.3.2. Repassivation on solar cells

To evaluate the Nafion repassivation at the cell level, n-type IBC solar cells were prepared. M2 size IBC cells were prepared and cut into 1/4 sizes using TLS and L&C. Nafion repassivation was performed using dip coating and the IV characteristic were measured before and after repassivation.

First, a test was conducted to determine whether the HF cleaning step could be skipped. The results are summarized in Table 5.1. As can be seen in Table 5.1, a similar efficiency gain can be achieved without the use of HF cleaning. The presence of native SiO_x on the edge has the potential to influence the repassivation quality of Nafion and is usually removed by HF etching. However, Table 5.1 shows that no improvement in repassivation quality was observed after additional HF etching before Nafion treatment. For a cost-effective industrial process, this HF etching post metallization should anyway be avoided. In the following experiment, all cells were treated without HF cleaning.

Table 5.1: Solar cells' IV changes (Δ) after repassivation, with and without HF clean. Cells are TLS emitter cut with 1-edge.

Group	Cell number	ΔV_{oc} (mV)	ΔJ_{sc} (mA/cm^2)	ΔFF (%)	$\Delta\eta$ (%)
HF clean	3	-0.10 ±0.13	0.08 ±0.00	0.31 ±0.07	0.13 ±0.03
non-HF clean	3	0.26 ±0.07	0.19 ±0.02	0.31 ±0.05	0.15 ±0.04

Different groups of samples were evaluated including different cutting methods (L&C and TLS), different edge types (emitter and BSF edges), as well as different cut-edge numbers (1-edge and 2-edge), and reference samples (L&C BSF cut cells with 2-edge) without repassivation were also measured to confirm the repeatability. Table 5.2 summarizes the IV results in detail. No repassivation was observed on either BSF or emitter edges of L&C cut samples. On TLS emitter cut samples, a clear improvement in efficiency was observed. In 1-edge cells, efficiency was improved by $0.14\%_{\mathrm{abs}}$; and in 2-edge cells,

Table 5.2: Solar cells' IV changes (Δ) after repassivation

Group	Cell number	ΔV_{oc} (mV)	ΔJ_{sc} (mA/cm^2)	ΔFF (%)	$\Delta\eta$ (%)
L&C, BSF 1-edge	3	0.02 ±0.22	-0.02 ±0.00	-0.03 ±0.02	-0.02 ±0.00
L&C, emitter 1-edge	3	-0.05 ±0.04	-0.01 ±0.00	-0.05 ±0.02	-0.01 ±0.02
TLS, emitter 1-edge	6	**0.10** ±0.19	**0.08** ±0.01	**0.31** ±0.08	**0.14** ±0.03
TLS, emitter 2-edge	5	**0.76** ±0.11	**0.17** ±0.01	**0.68** ±0.10	**0.32** ±0.04
TLS, BSF 1-edge	6	-0.16 ±0.14	0.01 ±0.01	-0.03 ±0.02	0.00 ±0.01
TLS, BSF 2-edge	5	0.18 ±0.25	0.00 ±0.02	-0.01 ±0.05	0.01 ±0.03
Reference (no repassivation)	5	-0.03 ±0.24	0.00 ±0.04	-0.01 ±0.09	0.00 ±0.02

Table 5.3: Quokka3 simulation results from [191], solar cells' IV changes (Δ) before and cutting.

Group	ΔV_{oc} (mV)	ΔJ_{sc} (mA/cm^2)	ΔFF (%)	$\Delta\eta$ (%)
emitter 1-edge	-2.04	-0.09	-1.15	-0.45
emitter 2-edge	-3.97	-0.19	-2.20	-0.85
BSF 1-edge	-0.84	-0.17	-0.16	-0.17
BSF 2-edge	-1.68	-0.33	-0.32	-0.33

efficiency was improved by 0.32%$_{\text{abs}}$. However, on BSF cut samples, no repassivation was observed. Factors contributing to this include:

- The edge recombination on BSF samples is relatively small. This is demonstrated by the Quokka3 simulation results in Table 5.3, which show the change in the IV parameters of a 1/4-cell with and without edge recombination. These simulation results were taken from [191] and were confirmed by the experimental data. As can be seen from Table 5.3, when cutting through the BSF regions, the efficiency losses are only around one-third compared with cutting through emitter regions. Therefore the potential efficiency gain from repassivation is relatively small for BSF cut region. For emitter samples, there was approximately 30 to 40%$_{\text{rel}}$ of initial efficiency loss was recovered by Nafion repassivation.

- Quokka3 simulation was performed to evaluate how SCR (defined by $J_{02,\text{ edge}}$) and qn bulk edge (defined by S_{eff}) recombination parameters influence the cell efficiency. The results are shown in Figure 5.4. The simulation results agree with the experimental observed 2-edge repassivation improvement for TLS cut emitter and BSF cells in Table 5.2 if one assume a $J_{02,\text{ edge}} \leq 3$ nA/cm and a S_{eff} in a range of 4000-8000 cm/s. By comparing the $J_{02,\text{ edge}}$ and S_{eff} values required to fit the experimental cut cells before and after repassivation, one can see that the largest effect of Nafion repassivation consist in significant reduction of edge SCR recombination ($J_{02,\text{ edge}}$). The additional reduction in S_{eff} from $S_{eff} = 10^6 cm/s$ to $S_{eff} = 4000 cm/s$ only seems to be beneficial for emitter cut. For BSF cut cells a S_{eff} below ~ 1000 cm/s would be needed to observe a repassivation effect.

- The final significant factor to consider is the uniformity of repassivation along the

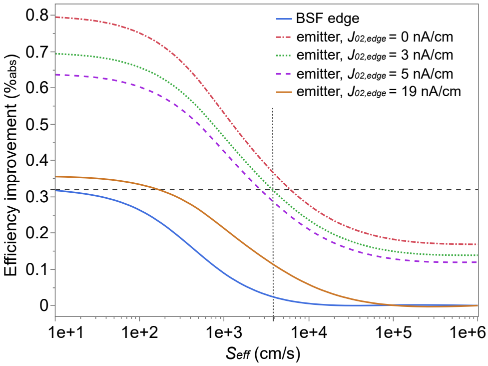

Figure 5.4: Quokka3 simulation results of potential efficiency improved with different edge recombination parameters. The simulation was done for a M2 1/4-cell with two recombining edges, either BSF or emitter edges. Efficiency improvement was simulated compared with cells with very high edge recombination ($J_{02,\text{ edge}}$ = 19 nA/cm and recombination of qn bulk $S_{eff} = 10^6 cm/s$). The horizontal dashed line represents the 0.32%$_{\text{abs}}$ efficiency improvement measured on emitter cells, and the vertical dotted line corresponds to the S_{eff} value at which $J_{02,\text{ edge}}$ = 3 nA/cm.

cut edge. From PL measurements, it was observed that the repassivation uniformity on solar cells is lower than that on lifetime samples. The PL profiles for the lifetime samples in Figure 5.3 are taken locally in a part of the cut edge with fewer defects in order to assess the maximum repassivation capability whereas the solar cell IV measurements take into account the effect of repassivation over the entire length of the cut edge. This non uniformity in the edge repassivation effect may explain the apparent discrepancy between the results on lifetime samples and the magnitude of the efficiency improvements upon Nafion treatment of the BSF and emitter cut cells. Therefore, it is conceivable that by improving the uniformity of the repassivation by Nafion treatment of the cut edge, a higher improvement in cell efficiency would be possible. The potential for such improvements is shown in Figure 5.4 if one assume further reduction in $J_{02,\text{ edge}}$ and especially in S_{eff} values.

Nevertheless, an average of 0.32%$_{\text{abs}}$ efficiency gain from Nafion edge repassivation is still significant improvement. One of the best cells with repassivation on two edges can be observed in the IV curves shown in Figure 5.5. It is evident from the IV curve and parameters that the improvement was predominantly due to increased FF, with only slight improvements in J_{sc} and V_{oc}.

5.3.3. Damp heat test results

In air, the Nafion passivation is not stable and the edge repassivation effect on the solar cell level rapidly wears off. This can be readily observed in Figure 5.6, where the initially excellent repassivation of an unencapsulated TLS emitter cut sample degrades over several hours of air exposure. The degradation can be observed from the gradient changes (from sharp to flat) of PL profiles measured at different time intervals.

An adhesive foil has been used in previous studies to protect the Nafion passivated

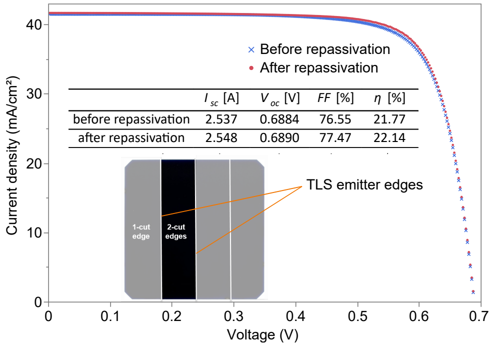

	I_{sc} [A]	V_{oc} [V]	FF [%]	η [%]
before repassivation	2.537	0.6884	76.55	21.77
after repassivation	2.548	0.6890	77.47	22.14

Figure 5.5: *IV* curves measured on a 1/4 M2 cell before (blue cross) and after repassivation (red dots), the cell was with 2-edge cut through emitter by TLS. The *IV* parameters and the cell images are also indicated.

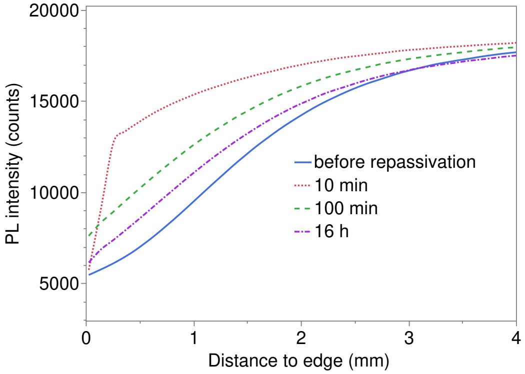

Figure 5.6: PL results of edge passivation over time, when the edge was exposed in the air.

samples from degrading [194]. However, this solution is not relevant for industrial production where several standard encapsulating materials are instead used to protect the solar cells. In this work, we studied whether or not such standard industrial encapsulation materials can preserve the passivation, as well as whether the Nafion passivation can withstand the heating and mechanical pressures introduced during the module assembly process.

After assembling modules with standard industrial processes and materials, the stability of the edge passivation was evaluated by damp heat (DH) testing according to the IEC 61215 standard. For the evaluation of edge repassivation stability, lifetime samples and high-resolution PL were again used. TLS cut samples were used since these showed encouraging results in the previous experiment and the tools are already commercially available. Samples were encapsulated with ethylene vinyl acetate (EVA) or polyolefin elastomers (POE) in a glass/backsheet structure.

PL images taken immediately after encapsulation and after 100 h of damp heat exposure (DH100) and 1000 h of exposure (DH1000) are shown in Figure 5.7(a). Combined with the PL intensity plots shown in Figure 5.7(b) and Figure 5.7(c), these show the ex-

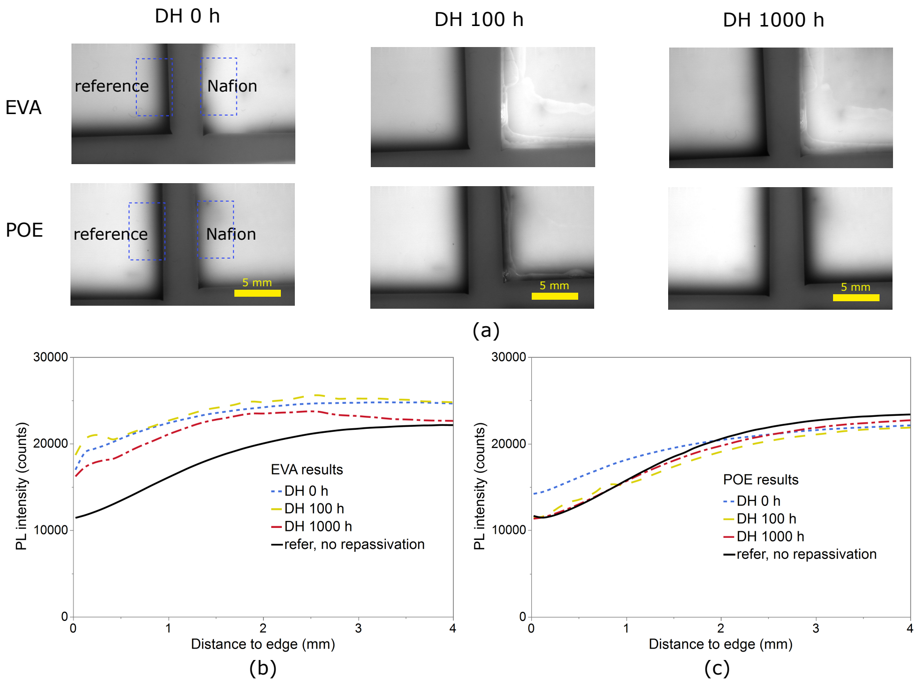

(a)

(b)

(c)

Figure 5.7: PL results of samples encapsulated with either EVA or POE and tested before and after exposure to damp heat (DH) conditions. The results of the PL measurements were taken before DH (DH0), after 100 h of damp heat exposure (DH100), and after 1000 h (DH1000), measured from the square areas marked. The normalised PL intensity profiles of Nafion passivated edges in EVA and POE are shown in (b) and (c), respectively.

tent of the repassivation effect of Nafion following the lamination process with both EVA and POE, as well as clearly demonstrating that the repassivation can survive the lamination process. However, the level of repassivation after lamination reduced in the POE case (starting point at x = 0 mm), relative to that of the EVA (starting point at x = 0 mm). In addition, significant differences are observed between the rates of degradation of the repassivation using EVA and POE, with the repassivation almost fully degraded after only 100 h in POE but with the repassivation remaining relatively stable even after 1000 h in EVA. POE is usually preferred over EVA for encapsulation, especially for n-type solar cell because of its better resistance against potential-induced degradation (PID) and superior moisture barrier performance. However, this work clearly demonstrates that EVA performs better in regards to maintaining the repassivation effect of the Nafion polymer.

5.4. Conclusion

In this study, edge repassivation of cut n-type silicon IBC solar cells using Nafion polymer was investigated. It was shown that Nafion can be used to passivate the cut edges of both n+/n/n+ and n+/n/p+ sample structures, but that the repassivation is more effective on n+/n/p+ structures (a solar cell) than on n+/n/n+ structures (a symmetric BSF sample). Furthermore, the effectiveness of the repassivation depends strongly on the cutting method used, with edges that have less laser damage after cutting (such as TLS) or mechanically cleaved edges being more susceptible to repassivation. An efficiency improvement of over 0.3$\%_{\text{abs}}$ was measured on 1/4-cut M2-size IBC solar cells with TLS cut emitter (n+/n/p+) edges, but there was no edge passivation observed on cut edges of symmetric n+/n/n+ structures or on solar cells with L&C cuts which is limited by passivation on bulk edge region. Importantly for industrial application of this material, encapsulation using EVA and POE were demonstrated to provide protection of the passivation through the solar module lamination process. However, only the EVA encapsulation provided protection against degradation of the passivation over time, with the edge passivation remaining stable even in harsh damp heat conditions (85 °C, 85% relative humidity) for 1000 h as per the IEC 61215 standard. In contrast, POE failed to provide such protection, with almost complete degradation of the encapsulant with only 100 h of damp heat exposure.

In summary, this work has shown that Nafion polymer can be used to repassivate the edges of cut n-type solar cells, but that the degree of repassivation provided depends heavily on the method used to cut the cells. Furthermore, this work has also shown for the first time that the repassivation provided by this material can be stable under harsh accelerated aging conditions when encapsulated with industrial standard EVA polymer. The repassivation can be achieved with a simple solution process at room temperature and without the use of vacuum, and this process could be simply integrated into the inline wet chemistry tools of industrial module manufacturing lines. Further research is necessary to improve the repassivation of n-type bulk regions and achieve uniform passivation on cell edges. Additionally, it is important to investigate the observed degradation in POE samples. Nevertheless, the results of this work firmly establish the viability of Nafion polymer, or analogues thereof, for edge passivation of industrial solar cells.

6

Sustainable back contact cells with screen printed copper[*]

Abstract

The high usage of silver (Ag) in industrial solar cells may limit the growth of the solar industry. One solution is to replace Ag with copper (Cu). A screen printable Cu paste was used in this study to metallize industrial interdigitated back contact (IBC) solar cells. A novel metallization structure was proposed to make solar cells. Cu paste was applied to replace the majority of the Ag used in IBC cells as busbars and fingers. Cu paste was evaluated for use as fingers, and solar cells were made to test conversion efficiency and reliability. The Cu paste achieved comparably low resistivity, and Cu paste printed cells demonstrated similar efficiency to Ag paste printed cells, with an average efficiency of 23%, and only 4.5 mg W^{-1} of Ag usage. Also, the solar cells are stable and no Cu in-diffusion was observed under damp heat (85 °C, 85% relative humidity) and thermal stress (200 °C) for 1000 hours, respectively. All processes used in this study can be carried out with industrial equipment. These findings reveal a new application for Cu pastes and point to a new direction for reducing Ag utilization and cost.

---

[*] This chapter is based on the following publication: **N. Chen**, D. Rudolph, C. Peter, M. Zeman, O. Isabella, Y. Rosen, M. Grouchko, O. Shochet, and V. D. Mihailetchi, *Thermal Stable High Efficiency Copper Screen Printed Back Contact Solar Cells*, Solar RRL, 7(2), 2200874 (2023).

6.1. Introduction

The photovoltaic (PV) industry has entered the Terawatt (TW) era. As of early 2022, the total PV installation has reached 1 TW [208]. Annual production and installation past TW level is expected in 2030 [209] or even earlier in 2028 [210]. One of the main concerns for the TW production is the shortage of certain materials [12]. Especially silver (Ag) is one of the key materials used to form electrodes onto silicon solar cells, and mostly applied as paste by screen printing method. For passivated emitter and rear contact (PERC) cells, the Ag consumption is currently around 12 mg W^{-1} [15]. In the case of new emerging industrial solar cells, like silicon heterojunction (SHJ) cells and tunnel oxide passivated contact (TOPCon) cells, the Ag consumption is even higher. International Technology Roadmap for Photovoltaic (ITRPV) predicts the Ag usage for PERC cells will reduce to 7.5 mg W^{-1} within the next 10 years [15]. However, to meet multi-TW production, Zhang et al. [18] proposed that Ag consumption should be reduced to 2 mg W^{-1}. In the near future, if the Ag usage does not decrease, it will not only result in more expensive solar cells, but also limit the sustainable growth of the PV industry.

To reduce the consumption of Ag on solar cells, researchers from industry and institutes are working on different approaches. The first way is to improve the traditional screen design and paste. The use of Ag can be reduced while not compromising cell efficiency, by printing fine lines and improving the finger height-to-width aspect ratio. With advanced screen design, Wenzel et. al [149] reported printed finger width can be reduced to 21 μm with 19 mg Ag paste lay down (without busbar), and the best efficiency group achieved 22.7% efficiency on PERC cells. Secondly, new equipment is being developed to metallize fine lines. Adrian et al. [211] have reported pattern transfer printing (PTP) with a finger width of 18 μm and an aspect ratio of 0.51. A rotary screen printing method developed by Lorenz et al. [212] has short printing cycles and a low Ag consumption of about 6-9 mg W^{-1}. Schube et al. [213] reported a novel metallization technology called FlexTrail-printing, and very low Ag consumption 0.05 mg W^{-1} has been achieved by using Ag nanoparticle ink. The use of dispensing equipment has also been developed for the metallization of solar cells [214], with 0.54 mg per Ag finger being reported [215]. The third way is to replace or reduce the use of Ag is to deploy other metals such as copper (Cu). Since Cu is an abundant commodity, replacing Ag with Cu will not have an effect on competing technologies [17]. Cu plating is one of the most promising methods of using Cu metallization. In mass production, SunPower/Maxeon has employed Cu plating for many years, resulting in the most efficient and reliable modules in the world [216]. Recent advances have been made on different cell structures [217, 218] in labs. Very recently, Sundrive and Maxwell have reported 26.41% record efficiency on large-size heterojunction solar cells by Cu plating [219].

Despite SunPower/Maxeon's success and excellent lab results, it can be difficult to introduce a new equipment and process into mass production. Manufacturers other than SunPower/Maxeon still have challenges when introducing plating equipment and other new processes. It takes considerable effort and time to evaluate throughput and yield, reduce equipment costs, and reassure environmental concerns regarding the plating process. With the introduction of new equipment with new materials, such as FlexTrail-printing with Ag nanoparticle ink, the challenges will be doubled.

On the other hand, screen printing has proven to be an effective metallization method that is both cost-effective and high-throughput. For industry, it is attractive that Cu can be applied through screen printing. One such application is Ag-coated Cu paste [220], particularly for SHJ cells [213]. By using a coated Ag on Cu particles, the Ag usage can be reduced by 30% to 50%. A more exciting alternative would be to use a Cu paste that is free of Ag. Previously, Cu paste was successfully used to replace busbar of solar cells [221, 222]. Cu pastes were also used as front fingers [223, 224], but either the cell efficiency reported was not as good as reference or was below the state of the art.

In this work, we demonstrate a new method for producing high efficiency interdigitated back contact (IBC) solar cells using screen printable Cu paste. Our previous study demonstrated that Cu paste can be used as busbar for IBC cells, resulting in high cell efficiency and module reliability [225]. In this study, we replace most of the Ag in IBC cells with Cu paste. An almost fully Cu metallized IBC solar is demonstrated and its efficiency is assessed. The reliability of Cu cells were also evaluated under damp heat conditions (85 °C, 85% relative humidity) and thermal stress at 200 °C for 1000 hours, respectively. The findings reveals a new application of Cu pastes to make high-efficiency solar cells and modules, and a new direction for reducing Ag usage.

6.2. Experimental details

6.2.1. Solar cell structure

To use Cu to replace Ag, a properly designed cell structure is needed. The structure of the solar cell used in this study is shown in Figure 6.1(a).

The solar cells are based on ZEBRA Gen2 cells [205] with a front surface field (FSF). In contrast to standard ZEBRA Gen2 solar cells, the new Cu IBC cells described in this contribution form the local contacts through the dielectric passivation layer stack using a narrow pattern of fire-through Ag paste. The Cu paste fingers are printed in a second printing step in alignment to those Ag contacts. This is achievable by means of a state-of-the-art screen printer. Figure 6.1(b) shows a microscope image of a printed Cu finger on Ag contacts. A critical part is the contact area, since there Cu diffusion into silicon may occur. To prevent Cu diffusion into silicon, there are two types of measures. First, the locally printed Ag patterns are used for contacting silicon and may also act as barriers between Cu and silicon. Second, the SiO_2/SiN_x stack layers (not visible in the microscopic image) serve both as passivation layers and barriers. The use of SiN_x has been proven to be an effective barrier to the diffusion of Cu [226].

6.2.2. Solar cell fabrication

The solar cells were fabricated based on ZEBRA Gen2 cells process flow [205], on 175 μm thick, n-type 6-inch wafers with a base resistivity of 6 ±3 Ω·cm. The front/back surface field (FSF/BSF) and rear emitter regions are formed in industrial tube diffusion furnaces using $POCl_3$ and BBr_3 as the diffusion sources, respectively. A plasma-enhanced chemical vapor deposition (PECVD) mask layer of SiN_x and a 532 nm nanosecond laser were used to form the interdigitated patterns on the rear side. The passivation and anti-reflection coating (ARC) layers were formed by a stacked layer structure comprising thermal SiO_2 grown $in-situ$ during the diffusion process and capped with SiN_x [227]. Finally, metallization was accomplished by screen printing three-dimensional metalliza-

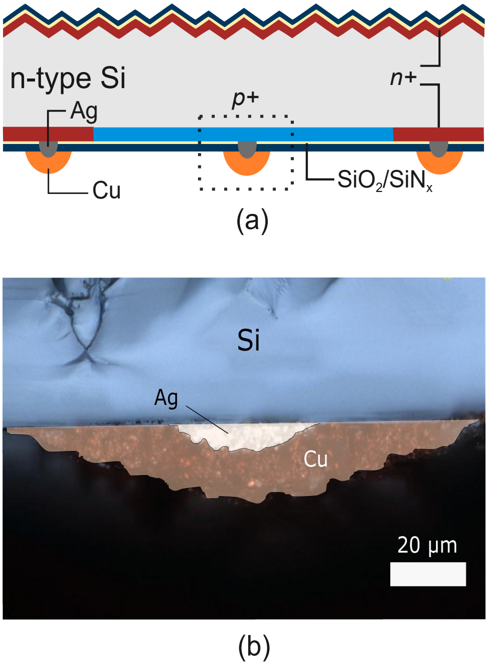

Figure 6.1: (a) Cross sectional sketch of the ZEBRA IBC solar cell structure used in this study. The microscope image of Ag contact coated with Cu finger is shown in (b), corresponding to the dashed area in (a).

tion patterns comprising busbars, fingers, and isolation layers. The solar cells were fabricated in the mass production line until the metallization step. For metallization, two groups of cells were made - Cu and Ag cells. Both cells were printed with point contact Ag pattern of a fire-through Ag paste, and dried at a around 200 °C followed by high-temperature firing process at around 800 °C to form the local Ag-Si contacts. In a second printing step, for Cu group, wider Cu paste fingers are printed in alignment to the Ag point contacts whereas for Ag groups the Ag fingers are printed. The Cu paste was dried at 100 °C for 30 seconds and then annealed at 300 °C for 5 seconds in a lamination machine. The Ag group was printed with a non-fire-through Ag paste, dried and fired in an inline furnace at around 700 °C for a few seconds. Then an insulation paste was printed for both groups and dried. After applying the insulation paste pattern, the busbars pairs are printed by either Cu paste or Ag paste to interconnect the p-type and n-type fingers, completing the multi-layer metallization pattern. The Cu paste used in the experiment, LF-371, was provided by Copprint Technologies Ltd. and all pastes used in this study are commercially available.

6.2.3. Mini-modules fabrication and reliability tests

Mini-modules were made from two pieces of half-cut cells for damp heat testing. Before module processing, the solar cells were cut into half cells by a 1064 nm laser (Rofin F20). For making modules, the ECA (Henkel) was dispensed on the busbar of cells (Stepcraft).

Ribbon were placed on ECA and fixed to the cells, then curing at 140 °C for 7 minutes on a hot plate. String connectors were connected to the ribbons by soldering [228]. The encapsulation layers - EVA or POE, glass, backsheets were placed on the cells, then laminated in a laminator (Phototrade - P. Energy) with recipes for EVA/backsheet, or POE/double-glass modules.

The mini-modules were tested under damp heat conditions for 1000 hours in a climate chamber (Vötsch) according to the IEC-61215 standard [229]. For the high temperature thermal stress test, half cut cells were used. The cells were placed between two pieces of glass, and put into a muffle furnace (Nabertherm). Then the cells were heated and annealed at a set temperature of 200 °C under N_2 flow in order to minimize oxidation. The modules or cells were taken out the climate chamber or furnace and cooled down to room temperature for measurement at different time intervals.

6.2.4. Characterization

One sun IV characterization was performed using a Class AAA xenon flasher (halm elektronik). Before measurement, the I_{sc} was calibrated by using a calibration cell or module (Fraunhofer ISE CalLab). The finger height, width and cross sectional area were analyzed using a laser scanning microscope (LSM, Olympus). The finger line resistance is calculated from busbar to busbar resistance which is measured from a resistance tester (ECN). PL and EL were measured using in-house developed equipment (ISC Konstanz). pFF and V_{oc} were from Suns-V_{oc} measurement [152], using an in-house developed chuck for IBC cells.

6.3. Results and discussion

6.3.1. Cu finger geometry and resistance

In this study, Cu pastes were printed as fingers and busbars. In a previous study we reported results about screen printed Cu busbars on IBC cells [225]. Here, the focus is on Cu paste as fingers. As a reference, a group of IBC cells were screen printed with the baseline Ag paste using the same screen layout. The Figure 6.2 shows typical microscope images of a finger printed with Cu paste and a finger printed with Ag paste. After printing and curing, the Cu finger has an average width of 125 μm, which is 25 μm wider than the Ag finger.

The difference in width is mainly due to the properties of the paste, and the Cu paste spreads more after screen printing. A revised formulation of Cu paste with improved viscosity and thixotropic index for printing fine lines will be tested in the near future. However, the 125 μm finger width is acceptable for use on the rear side of IBC cells in this study. As can be seen by the typical cross section view in Figure 6.2(c), the Cu finger height is approximately 8 μm whereas the Ag finger height is approximately 11 μm. In addition, the Cu finger has a flatter top than the Ag finger, which is related to the different sintering processes used for the two pastes. Overall, the cross sectional areas of the two pastes are mostly similar.

The line resistance were measured as 0.64 ±0.03 $\Omega \cdot cm^{-1}$ for Cu fingers and 0.35 ±0.03 $\Omega \cdot cm^{-1}$ for Ag fingers. As the cross sectional areas of the two pastes are similar, the differences in line resistance are primarily due to differences in the resistivity of the pastes.

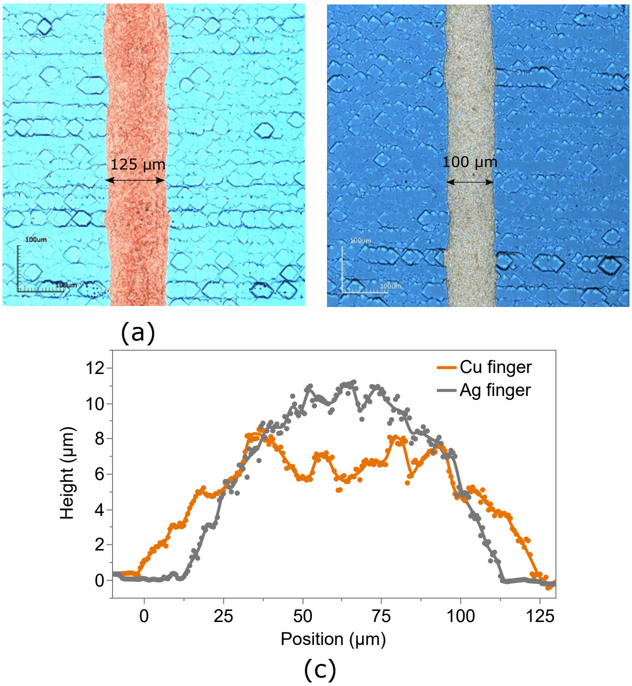

Figure 6.2: A microscope snapshot of a typical printed Cu finger (a) and printed Ag finger (b) on the IBC cells. Typical cross sections of a Cu finger and a Ag finger are reported in (c).

Based on the line resistance and the cross sectional area, we have calculated that the Cu resistivity is approximately $5 \times 10^{-6} \Omega \cdot cm$. This result is superior to the previous reported values for a Cu paste [230, 231], which were annealed at a higher temperature in nitrogen or in vacuum. The solar cell results are shown in the next subsection.

6.3.2. Solar cell results

A batch of IBC solar cells precursors were identically fabricated up to the metallization step. A first layer of Ag fire-through paste was then screen printed using a point contact pattern and fired in a fast firing furnace according to our best-known method. Subsequently the cells were randomly distributed in two groups as follow: a Ag group of cells that were printed with Ag fingers and Ag busbars, and a Cu group of cells that were printed with Cu fingers and Cu busbars.

Figure 6.3 illustrates the parameters extracted from current-voltage (IV) characteristics of all cells under the standard test conditions (STC). IV results are also summarized in Table 6.1 along with their averages and standard deviations. In both groups, V_{oc} values are similar, with an average V_{oc} of around 689 mV. Compared to the Ag group, the Cu group has a lower average J_{sc} of 0.1 mA/cm^2. Cells with median J_{sc} were measured for quantum efficiency (QE), and the results are shown in Figure 6.4. In long wavelength range, QE and reflenctance curves are similar for Ag cell and Cu cell. There were slightly higher QE curves measured on Ag cells in the wavelength range between 400 and 1000

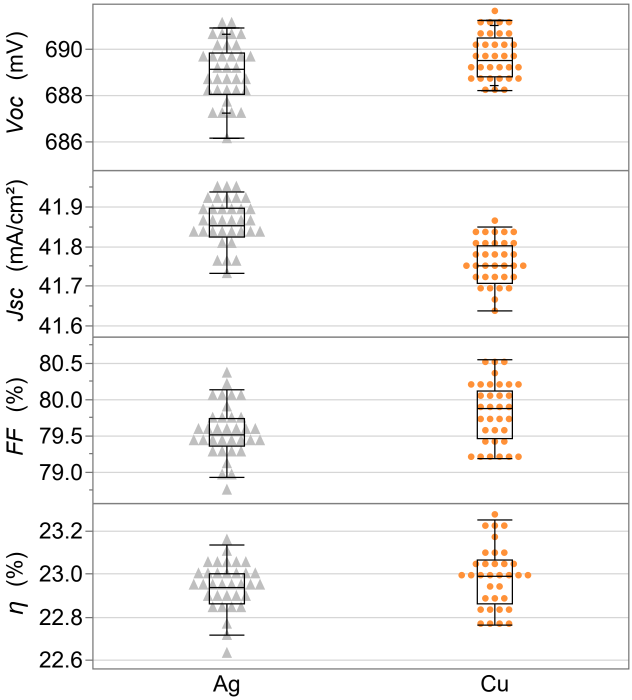

Figure 6.3: IV results of solar cells made using Ag and Cu pastes. In the box-and-whisker plots, the box show the median, 25^{th} and 75^{th} percentiles, and the whiskers are minimum and maximum data values excluding outliers.

nm. The results suggest that the difference in J_{sc} may be caused by factors other than pastes (e.g., difference in wafer bulk lifetime).

In terms of fill factor (FF), the Cu cells exhibit a $0.3\%_{abs}$ higher FF on average than that of the Ag cells. However, compared to the standard deviations, the differences between the groups were not statistically significant. It is worth noting that the Ag cells were fired twice (contact and fingers, respectively), and the two firing steps need to be carefully tuned to get an optimal FF. In contrast, Cu cells require only one firing step, which makes it easier to optimize the firing process and improve the FF in the future.

At last, in terms of cell efficiency, same efficiency was achieved for both the Cu metallized group and the reference Ag metallized group. The average efficiency of Cu cells group (34 cells) was 23%, with the best cell efficiency of 23.25%.

By using Cu paste, the Ag consumption was reduced to 25 mg for a 6-inch M2 wafer (our best result so far), which is less than 4.5 mg W^{-1}. Compared to current state-of-the-art PERC cells, which use approximately 12 mg W^{-1} Ag, the Ag consumption was reduced by over 60%. Moreover, Ag consumption can be further reduced by printing thinner and smaller layers of Ag.

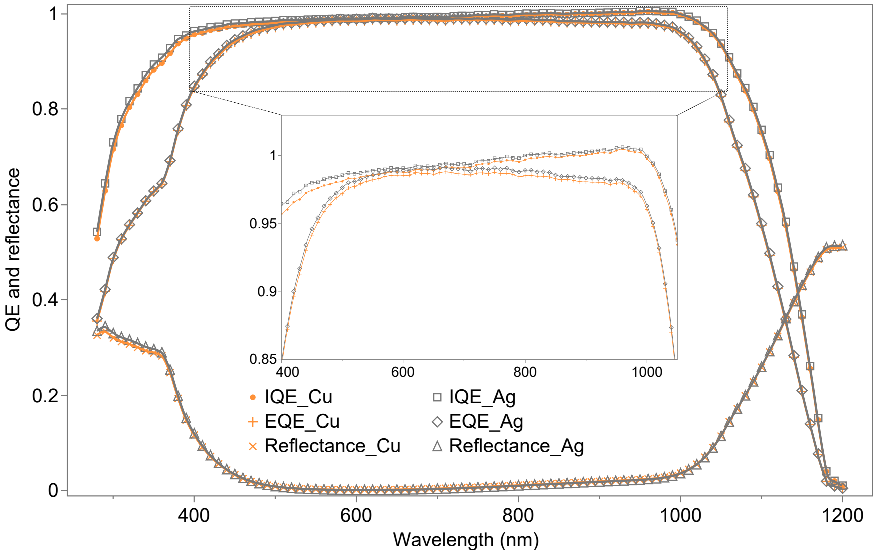

Figure 6.4: Quantum efficiency (QE) and reflectance curves of Cu and Ag solar cells with median I_{sc} selected from each group. From 400 nm to 1000 nm, the Ag cell exhibits better QE.

Table 6.1: IV summary of Cu and Ag printed cells

Paste	Data type	$V_{oc}(mV)$	$J_{sc}(mA/cm^2)$	$FF(\%)$	$\eta(\%)$
Ag	Best cell	687.2	41.92	80.32	23.14
	Avg. of 34 cells	688.9±1.2	41.85±0.05	79.54±0.36	22.94 ±0.11
Cu	Best cell	690.2	41.80	80.56	23.25
	Avg. of 34 cells	689.6±0.9	41.75±0.06	79.81±0.41	22.98±0.13

6.3.3. Reliability of damp heat test

Besides the efficiency of the solar cell, the main concern for Cu metallized cells and modules is their reliability. In spite of this, there are no standards specifically designed for testing Cu paste printed solar cells. In accordance with IEC standard 61215, damp heat (DH) and thermal cycling (TC) tests are the most relevant tests. As described in our previous study [225], we demonstrated that after DH3000 and TC600 the modules with Cu busbars show no sign of cells degradation due to Cu in-diffusion. Several mini-modules with Cu metallization of both fingers and busbars were also tested for DH in this study. We skipped TC tests since they were more related to interconnections, which have already been tested for Cu busbar [225]. For DH test, the mini-modules were manufactured with different combinations, including glass-backsheet (BS) structures with ethylene vinyl acetate (EVA) encapsulation, and glass-glass structures with polyolefin elastomer (POE) encapsulation, as detailed in the experimental section. Since we are still working on improving the peel force of soldering method, we used electrically conductive adhesives (ECA) to make mini-modules in this experiment. The Ag-containing ECA was used to demonstrate the reliability of Cu cells in the experiment. In mass produc-

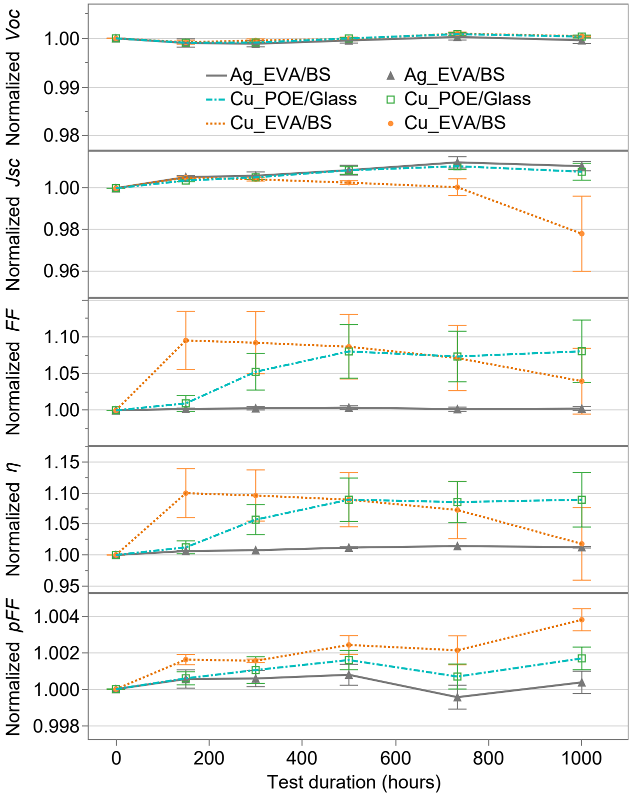

Figure 6.5: Normalized IV parameters and pFF changes of different mini-modules during 1000 hours DH exposure. Three types of mini-modules were tested, including Cu cells encapsulated in POE and glass-glass (POE/Glass), in EVA and glass-backsheet (EVA/BS), and reference Ag cells encapsulated in EVA and glass-backsheet (EVA/BS). The values are averages of 3 samples with the error bar representing one standard deviation, and the shaded areas indicate the 95% confidence interval.

tion, either ECA can be used (in this case, the Ag usage in ECA should also be considered [18]), or Ag-free solutions such as soldering with SnPb ribbon can be employed (in development).

Figure 6.5 illustrates the normalized IV parameters and pFF changes of different mini-modules during the 1000 hours' DH test. Three types of mini-modules were tested, including Cu cells encapsulated in POE and glass-glass (POE/Glass), in EVA and glass-backsheet (EVA/BS), and reference Ag cells encapsulated in EVA and glass-backsheet (EVA/BS). One of the unexpected findings is the increase in FF observed in the Cu groups. FF of Cu modules with EVA/BS increased until around DH200 and then decreased whereas the FF of Cu modules with POE/Glass increased by ~10% and remained stable. On the other hand, the FF of reference Ag modules remained unchanged during the test. An unexpected observation is that the initial FF of Cu modules was low around 70%, while Ag modules had a high FF of around 78%. Electroluminescence (EL) images indicate that the low initial FF of Cu modules is due to poor interconnection between Cu paste

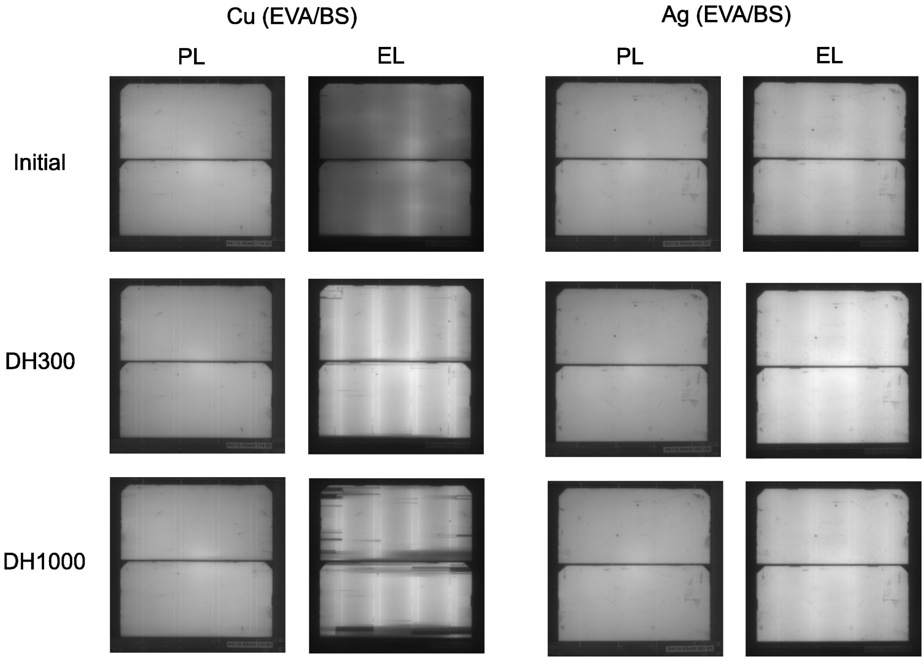

Figure 6.6: Photoluminescence and electroluminescence images of Cu metallized (left clomuns) and Ag metallized (right columns) samples measured at the initial stage, 300 hours, and 1000 hours after damp heat test.

and ECA. Photoluminescence (PL) and electroluminescence (EL) results are shown in Figure 6.6.

During the DH test, the FF of Cu cells increased or decreased due to changes in the interconnection between Cu busbar and ECA. It is not yet clear what the underlying cause is. For all groups, the V_{oc} and pFF remain stable during the test. For the Cu groups, there was even a small increase in pFF. The pFF increased by 0.4 $\%_{\text{rel}}$ and 0.2 $\%_{\text{rel}}$ for the EVA/BS and POE/Glass groups, respectively. From these stable pFF and V_{oc} results, we can conclude that there is no Cu in-diffusion observed during the DH1000 test.

6.3.4. Stability under thermal stress

For commercial modules, manufacturers generally provide a warranty of 25 years or longer. That means, modules should retain at least 80 percent of their original power generation capacity after 25 years. However, it should be noted that the “standard module qualification test results cannot be used to obtain or infer a product lifetime" [232]. To test the long-term reliability of Cu metallized cells, additional accelerated tests are required. According to Bartsch et al., stability under thermal stress can be estimated by fitting pFF loss measurement data at different temperatures using the Arrhenius plot [233]. Our study, however, did not observe obvious pFF losses from the high temperature degradation test at 200 °C, so it was not possible to use this method.

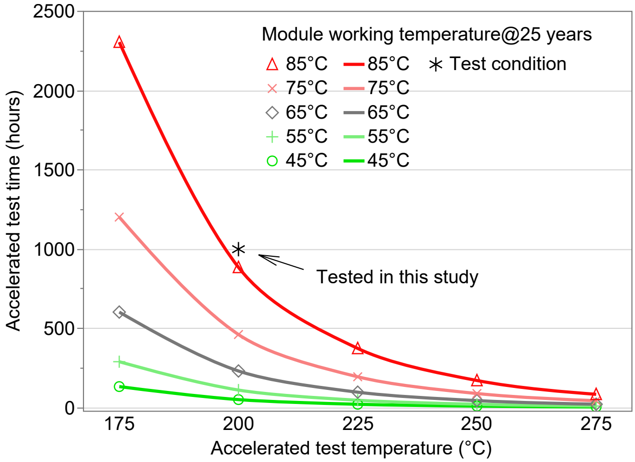

Figure 6.7: Calculated accelerated thermal stress test temperature (x-axis) and time (y-axis) according to the different module operating temperatures (shown in the legend). Conditions with 1000 hours at 200 °C was tested in this study, shown as asterisk.

Alternatively, the long term stability of the cells can be determined by using the Arrhenius model, using the equation [234]:

$$\frac{t(T_{use})}{t(T_{acc})} = exp\left[\frac{E_a}{k}(\frac{1}{T_{use}} - \frac{1}{T_{acc}})\right] \tag{6.1}$$

In the equation, T_{use} is the device's operating temperature, and T_{acc} is the acceleration testing temperature, k is Boltzmann constant, and E_a is activation energy; The device working time (e.g. 25 years) is represented as $t(T_{use})$, and the corresponding testing time is $t(T_{acc})$.

One of the challenges of using this method is the difficulty in determining the activation energy. Similarly to a previous study [235], we used here the activation energy as suggested in the standard of the European Cooperation for Space Standardization (ECSS) for photovoltaic assemblies and components (ECSS-E-ST-20-08C Rev.1) [236]. The standard assumes an activation energy of 0.70 eV, which applies to “crystalline silicon and single and multi-junction GaAs solar cells with a thickness of more than 50 μm."

By using equation 6.1 and an activation energy of E_a=0.70 eV, the temperature and time required to conduct an accelerate test can be calculated.

Figure 6.7 shows the estimated temperature and time needed for acceleration test based on different working temperatures for 25 years. For example, the green curve at lowest position assumes that the modules working temperature is 45 °C (typical working temperature stated in the module datasheet, also called nominal module operation temperature (NMOT)) for 25 years, and that the acceleration test should take place for 50 hours at 200 °C. For worse-case scenarios, the working temperatures of 55 °C, 65 °C, 75 °C, and 85 °C are also provided. As a worst case scenario, for example 85 °C for 25 years, the acceleration test should be carried out for 900 hours at 200 °C. With a higher test temperature, such as 250 °C, the acceleration testing time can be significantly reduced.

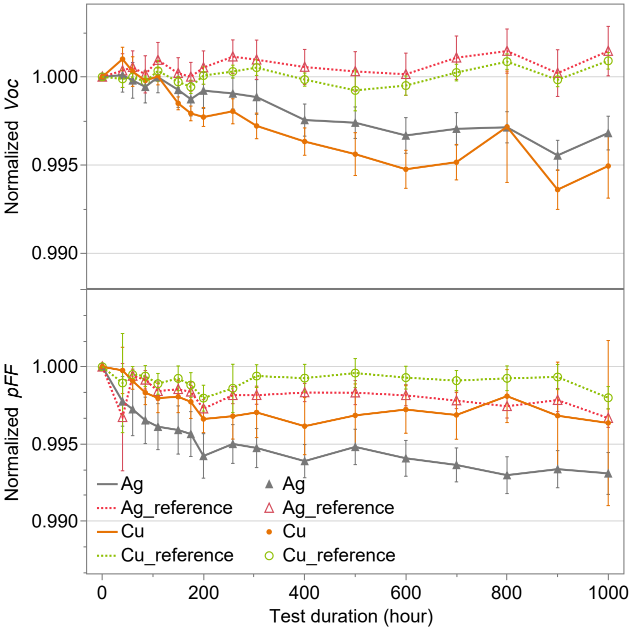

Figure 6.8: Results of normalized V_{oc} and pFF of different groups, including Ag cells (Ag) and Cu cells (Cu) exposed to 1000 hours of 200 °C, as well as reference groups with Ag cells (Ag_reference) and Cu cells (Cu_reference) kept at room temperature. The values are averages of 3 to 5 samples with the error bar representing one standard deviation, and the shaded areas indicate the 95% confidence interval.

In this study we considered a worst case scenario by testing the Cu cells at 200 °C for 1000 hours, which is equivalent to a module working at 85 °C for more than 25 years. The temperature of 200 °C was chosen because the cell structure of the IBC cells will not be damaged at this temperature. Also, 1000 hours is an acceptable time frame for testing, which can be completed within two months, including characterization. Four groups of samples were measured: Two groups underwent the 200 °C thermal stress testing, and two reference groups were kept at room temperature. The test results are shown in Figure 6.8, which includes the two most degradation sensitive cell parameters - V_{oc} and pFF. During these tests, the reference groups with Ag or Cu paste showed stable V_{oc}; the fluctuations were only due to measurement errors. A slight reduction in V_{oc} was observed for test groups of Ag and Cu cells. For Cu cells, a degradation in V_{oc} of only around 0.5%$_{\text{rel}}$ or 3.4 mV was observed. Additionally, the PL results shown in Figure 6.9 confirm the V_{oc} results on Cu and Ag tested cells. In terms of pFF changes, the reference groups are stable with no change after 1000 hours. After 1000 hours of accelerating temperature test, the decrease in pFF for the Cu printed group is less than 0.5%$_{\text{rel}}$, indicating that there is no sign of Cu diffusion into the silicon during this time period, which would otherwise resulted in significantly higher pFF degradation [226]. Moreover, this is demonstrated also by the reference Ag group results, which show similar or slightly higher pFF loss during the test.

In summary, there was no measurable pFF degradation observed in these acceler-

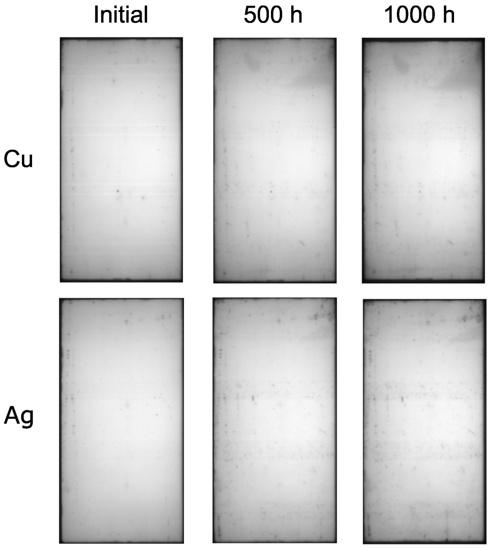

Figure 6.9: Photoluminescence images of Cu cell (top) and Ag cell (bottom) at the initial stage of heat stress, exposed to 200 °C for 500 hours and 1000 hours, respectively.

ated stress tests, which indicates that no Cu diffusion into the silicon took place. The pFF losses of Cu cells are comparable to previous reports with thick nickel barriers on plated Cu cells [226]. The screen printed fire-through Ag paste served as an effective barrier. Cu diffusion may be inhibited by the paste constituents (particularly the glass frit). Similarly, in a report from Kraft et al. [237], Ag pastes were used as seed layers for Cu-plated cells, and the seed layer was also noticed as a barrier which may be related to the paste composition. In our study, the additives present in the Cu paste prevented oxidation. During the solar cell process, the Cu paste remained stable. No oxidation occurred during the curing process even when the process temperature was elevated to 300 °C (as determined by the paste resistivity and color). In a recent report, a Cu paste was even used to directly contact the front side of p-PERC cells with no barriers [238]. Screen printed Cu pastes for metallization of solar cells are attracting researchers' attention. In contrast to the extensively studied plated Cu [239], more research is needed on screen printed Cu pastes and cells, notably on the contact formation and diffusion of Cu and their impact on long-term stability.

6.4. Conclusion

In this study a screen printed Cu paste was used as a conductive layer for IBC cells in order to replace the majority of Ag utilization. The cells were printed using two layers - a thin fire-through Ag paste was printed first, followed by Cu paste applied as fingers and busbars. The Cu paste printed cells achieve the same level of efficiency as the reference fully Ag paste printed cells, both groups achieving average efficiencies of 23%. Cu paste replaced most of the Ag usage in the cells, resulting in a Ag consumption of only 4.5 mg W^{-1}. In addition, reliability and stability were examined. There was no degradation in V_{oc} and pFF during the damp heat stress test (85 °C, 85% relative humidity) of 1000 hours. Under more severe test conditions - a thermal stress test under 200 °C for 1000 hours - V_{oc} of Cu cells only degraded by $0.5\%_{\mathrm{rel}}$, and pFF only by $0.3\%_{\mathrm{abs}}$. The reliability and stability results convincingly show that Cu diffusion into Si bulk from a screen printed paste can be prevented. The findings of this study demonstrate that the screen printed Cu paste has an immediate potential to replace most of the Ag used for metallization of an industrial cell concept.

7

Conclusions and outlook

7.1. Conclusions

Climate change presents a significant challenge to humanity, evident from the increasing levels of CO_2 and global warming and other indicators. To achieve the Paris Agreement's goal of limiting global warming to 2 °C or even 1.5 °C, we must reduce greenhouse gas emissions by using zero-carbon energy sources. Photovoltaic technology emerges as a primary solution to address this challenge.

This thesis focuses on the investigation of interdigitated back contact (IBC) cells, which are among the most efficient industrial solar cells. In particular, the IBC technology in this study is based on ZEBRA technologies developed by ISC Konstanz, featuring both high-efficiency and low-cost. The aim is to improve the efficiency of ZEBRA cells and modules and to reduce their costs while improving their sustainability, making them a more attractive option for industrial applications.

Currently, the photovoltaic market is dominated by silicon solar cells. Considering the historical development of silicon solar cells, IBC technology exhibits enormous potential as a next-generation photovoltaic technology. Chapter 2 of this thesis provides a comprehensive review of past cell technologies, including the earlier Al-BSF technology, the present PERC technology, and passivated contact cell technologies. The emphasis is placed on industrial cell structures and the associated process flows. Through the analysis of historical developments, it becomes evident that modifications in the structure and process flow of solar cells are built upon prior advancements. The next generation of solar cells must leverage the advantages inherited from previous generations to achieve optimal results. IBC technology is a promising candidate for the next generation of solar cells and is considered to be the ultimate solar cell structure for single-junction cells. However, it should be noted that there is currently no established standard process flow for IBC cells. By building on established technologies like ZEBRA, industrial IBC cells can benefit from the knowledge and experience gained, facilitating a smoother transition and optimized manufacturing processes.

This thesis focuses on two approaches aimed at enhancing the efficiency and sustainability of ZEBRA technology. The first approach focuses on improving efficiency by minimizing cut edge recombination, while the second approach aims to develop low-cost and sustainable IBC cells by replacing Ag with Cu. Futhermore, throughout the work, reliability tests were conducted to ensure the robustness of the technology. These tests serve to ensure that the advancements made in efficiency and sustainability are accompanied by a high level of reliability, thus validating the practical viability of ZEBRA technology.

Chapter 3 of the thesis provides a summary of the experimental and characterization methods employed in the study. Various cutting techniques were evaluated, with particular emphasis on the laser cutting damages. For metallization, screen printing was chosen as the preferred method. To characterize the cells, specialized equipment was utilized. An IV tester equipped with a custom-designed chuck enabled precise determination of the current-voltage characteristic. Additionally, high-resolution photoluminescence (PL) was employed to gather detailed information on passivation at the edges. In order to assess the reliability and long-term stability of the cells, a series of tests were conducted. These tests included standard assessments in accordance with the IEC 61215 requirements, as well as an additional thermal stress test designed to evaluate the cells' performance under extended thermal conditions.

Chapters 4 and 5 of the thesis focused on the study of cut edge recombination and its mitigation. In Chapter 4, cut losses of IBC cells were investigated. The study found that for IBC cells, cut losses can be minimized by cutting through the BSF regions. When a 23% cell is cut into 1/3 pieces through BSF, the efficiency can increase by $1.2\%_{\text{rel}}$ under standard 1-sun testing conditions, compared to cutting through the emitter. Under a low light intensity of 0.25-sun, the improvement is around $2.4\%_{\text{rel}}$. Half-cut cells exhibited an efficiency increase of around $0.1\%_{\text{abs}}$ under standard testing conditions. Mass production can be easily accomplished with this technique. For a 200 MW cell line, the resulting $0.1\%_{\text{abs}}$ efficiency gain would translate to approximately 1.0 MW cells, which equates to more than 3,000 high-efficiency modules. Furthermore, this technique can also improve the energy yield as a result of better low light performance.

In order to further reduce edge recombination, edge passivation technologies were investigated in Chapter 5. Edge passivation can be achieved using Nafion, a polymer that shows promise at both the cell and module levels. The study found that in 1/4-cut M2 size (156.75 mm × 156.75 mm) IBC cells with two emitter edges, efficiency was improved by over $0.3\%_{\text{abs}}$ with the use of Nafion passivation. However, no significant improvement in efficiency was observed for similar cells with back surface field (BSF) edges. The passivation was found to work on both thermal laser separation (TLS) and mechanically cleaved edges. Furthermore, the passivation was stable under industry standard testing of 1000 hours under damp heat conditions (85 °C, 85% relative humidity) in EVA encapsulants. Although edge passivation is not currently being used in industry, it holds promise for future applications.

In Chapter 6, the replacement of Ag with Cu paste is studied. Metallization was done by screen printing and adjustments were made to the cell structure and process to accommodate Cu application. The cells were designed using a two-layer structure, with Ag paste used as contact layers and Cu paste used as the conductive layer. The Cu paste printed cells achieved the same level of efficiency as the fully Ag paste printed reference cells, and both groups achieved average efficiencies of 23%. Moreover, the Cu paste replaced most of the Ag use in cells, resulting in a significant reduction in Ag consumption to only 4.5 mg W^{-1}. Additionally, reliability and stability tests are evaluated. There was no degradation in V_{oc} and pFF during the damp heat stress test (85 °C, 85% relative humidity) of 1000 hours. Under more severe test conditions, a thermal stress test under 200 °C for 1000 hours - V_{oc} of Cu cells was only degraded by $0.5\%_{\text{rel}}$, and pFF only by $0.3\%_{\text{abs}}$. The findings of this study demonstrate that screen printed Cu paste has immediate potential to replace most of the Ag used for metallization in industrial solar cells.

In summary, this thesis focuses on enhancing the efficiency and sustainability of back contact cells. Three main achievements have been made. First, cut losses can be reduced by cutting through different regions. The finding has been implemented in production to minimize cutting loss in cut-cell modules. Second, the edge losses can be further improved by using Nafion polymer edge passivation. The results demonstrate improved efficiency and stability, highlighting significant potential for industrial implementation. Last, Cu metallization was proposed for back contact cells. A low Ag usage of only 4.5 mg W^{-1} was achieved, which is significantly lower than the market standard (12 mg W^{-1} in PERC cells). Together with excellent reliability performance, these findings indicate the advantages of back contact cells that could revolutionize the field.

7.2. Outlook

Further research is expected to extend the scope of this thesis. A wider range of polymer materials could be explored in terms of reducing edge recombination. Specifically, the focus would be on:

1. Widely screening multi-functional materials that can serve as both passivation and encapsulation.
2. Cost-effective solutions for mass production can be explored, which may involve investigating new equipment and coating methods.

To achieve sustainable metallization, further research can be conducted in the following areas:

1. Further optimization of contact layers, to reduce the Ag usage below 2 mg W^{-1}. Current technologies for Ag paste printing primarily involve printing thick layers, commonly referred to as thick-film printing. However, for use as contact layers, a thick layer is not required. By optimizing paste formations and screen designs, it is possible to significantly reduce the amount of Ag paste used. Achieving Ag usage of less than 2 mg W^{-1} is feasible through these optimizations.
2. Additional testing of reliability and module solutions. Considering their long lifespan, solar modules are very special electrical products. Greater emphasis should be placed on reliability and more tests should be conducted. In addition to standard tests (according to IEC 61215, UL 1730 et al.), non-standard tests should also be performed. Non-standard tests should take into account product properties (for example, oxidation problems with Cu) and the environment in which the modules will be used. For example, if modules are used in a tropical environment, an additional damp-heat test should be considered. The results obtained from

these tests can guide the development of solutions, considering both the cell/paste level and the module as a whole.

More studies are being conducted within the European Commission's (EC) IBC4EU project, coordinated by ISC Konstanz. The author of this thesis is eagerly anticipating the advancements that will arise from these studies.

References

[1] H. K. Observatory, *Vital indicators of climate change,* (accessed on 20/02/2023).

[2] NASA, *If earth has warmed and cooled throughout history, what makes scientists think that humans are causing global warming now?* (accessed on 20/02/2023).

[3] NASA, *Land-ocean temperature index,* (accessed on 28/02/2023).

[4] NOAA, *Noaa gml data,* (accessed on 03/03/2023).

[5] U. N. E. P. (2022), *Emissions gap report 2022,* (accessed on 20/02/2023).

[6] I. P. on Climate Change (IPCC), *The evidence is clear: the time for action is now. we can halve emissions by 2030,* (accessed on 20/02/2023).

[7] U. Nations, *Facts and figures,* (accessed on 28/02/2023).

[8] W. Hoffmann, *Pv as a major contributor to the ∼100% renewably powered world and solving the climate battle,* in *High-Efficient Low-Cost Photovoltaics* (Springer, 2020) pp. 9–30.

[9] M. Perez and R. Perez, *Update 2022–a fundamental look at supply side energy reserves for the planet,* Solar Energy Advances **2**, 100014 (2022).

[10] A. Smets, K. Jäger, O. Isabella, R. van Swaaij, and M. Zeman, *Solar energy: The physics and engineering of photovoltaic conversion (kindle edition),* Technologies and Systems , 62 (2016).

[11] pv magazine, *Solar in the new king of energy markets,* (accessed on 03/03/2023).

[12] P. J. Verlinden, *Future challenges for photovoltaic manufacturing at the terawatt level,* Journal of Renewable and Sustainable Energy **12** (2020).

[13] pv magazine, *Global solar capacity additions hit 268 gw in 2022, says bnef,* (accessed on 03/03/2023).

[14] LONGi, *At 26.81%, longi sets a new world record efficiency for silicon solar cells,* (accessed on 10/02/2023).

[15] J. Trube, *International Technology Roadmap for Photovoltaic (ITRPV): 2021 Results*, Report (VDMA Photovolt. Equipment, 2022).

[16] Y. Chen, D. Chen, P. P. Altermatt, S. Zhang, L. Wang, X. Zhang, J. Xu, Z. Feng, H. Shen, and P. J. Verlinden, *Technology evolution of the photovoltaic industry: Learning from history and recent progress,* Progress in Photovoltaics: Research and Applications (2022).

[17] M. A. P. Macé, E. Bosch, *Terawatt scale pv by 2050 and competition for minerals: The case of silver and copper,* in *38th European Photovoltaic Solar Energy Conference and Exhibition* (2021) pp. 683–689.

[18] Y. Zhang, M. Kim, L. Wang, P. Verlinden, and B. Hallam, *Design considerations for multi-terawatt scale manufacturing of existing and future photovoltaic technologies: challenges and opportunities related to silver, indium and bismuth consumption,* Energy & Environmental Science **14**, 5587 (2021).

[19] B. Hallam, M. Kim, Y. Zhang, L. Wang, A. Lennon, P. Verlinden, P. P. Altermatt, and P. R. Dias, *The silver learning curve for photovoltaics and projected silver demand for net-zero emissions by 2050,* Progress in Photovoltaics: Research and Applications (2022).

[20] R. Underwood, M. Kim, S. Drury, Y. Zhang, L. Wang, C. Chan, and B. Hallam, *Abundant material consumption based on a learning curve for photovoltaic toward net-zero emissions by 2050,* Solar RRL , 2200705 (2022).

[21] B. Hallam, M. Kim, R. Underwood, S. Drury, L. Wang, and P. Dias, *A polysilicon learning curve and the material requirements for broad electrification with photovoltaics by 2050,* Solar RRL **6**, 2200458 (2022).

[22] A. Lennon, M. Lunardi, B. Hallam, and P. R. Dias, *The aluminium demand risk of terawatt photovoltaics for net zero emissions by 2050,* Nature Sustainability **5**, 357 (2022).

[23] I. Fraunhofer, *Photovoltaics report,* Fraunhofer ISE, Freiburg (2022).

[24] P. Holzhey, M. Prettl, S. Collavini, N. L. Chang, and M. Saliba, *Toward commercialization with lightweight, flexible perovskite solar cells for residential photovoltaics,* Joule (2023).

[25] D. M. Powell, R. Fu, K. Horowitz, P. A. Basore, M. Woodhouse, and T. Buonassisi, *The capital intensity of photovoltaics manufacturing: barrier to scale and opportunity for innovation,* Energy & Environmental Science **8**, 3395 (2015).

[26] W. Shockley and H. J. Queisser, *Detailed balance limit of efficiency of p-n junction solar cells,* Journal of applied physics **32**, 510 (1961).

[27] T. Tiedje, E. Yablonovitch, G. D. Cody, and B. G. Brooks, *Limiting efficiency of silicon solar cells,* IEEE Transactions on electron devices **31**, 711 (1984).

[28] A. Richter, M. Hermle, and S. W. Glunz, *Reassessment of the limiting efficiency for crystalline silicon solar cells,* IEEE journal of photovoltaics **3**, 1184 (2013).

[29] S. Schäfer and R. Brendel, *Accurate calculation of the absorptance enhances efficiency limit of crystalline silicon solar cells with lambertian light trapping,* IEEE Journal of Photovoltaics **8**, 1156 (2018).

[30] M. Green, *Efficiency limits for perc, topcon, hjt and ibc,* (accessed on 10/02/2023).

[31] NREL, *Best research-cell efficiency chart,* (accessed on 10/02/2023).

[32] M. A. Green, E. D. Dunlop, G. Siefer, M. Yoshita, N. Kopidakis, K. Bothe, and X. Hao, *Solar cell efficiency tables (version 61),* Progress in photovoltaics: research and applications **31**, 3 (2023).

[33] J. Mandelkorn and J. H. Lamneck Jr, *A new electric field effect in silicon solar cells,* Journal of Applied Physics **44**, 4785 (1973).

[34] P. Singh, R. Kumar, M. Lal, S. Singh, and B. Das, *Effectiveness of anisotropic etching of silicon in aqueous alkaline solutions,* Solar Energy Materials and Solar Cells **70**, 103 (2001).

[35] Y. Nishimoto, T. Ishihara, and K. Namba, *Investigation of acidic texturization for multicrystalline silicon solar cells,* Journal of the Electrochemical Society **146**, 457 (1999).

[36] W. Kern, *The evolution of silicon wafer cleaning technology,* Journal of the Electrochemical Society **137**, 1887 (1990).

[37] M. Meuris, P. W. Mertens, A. Opdebeeck, H. Schmidt, M. Depas, G. Vereecke, M. Heyns, and A. Philipossian, *The imec clean: A new concept for particle and metal removal on si surfaces,* Solid State Technology **38**, 109 (1995).

[38] A. Dastgheib-Shirazi, M. Steyer, G. Micard, H. Wagner, P. P. Altermatt, and G. Hahn, *Relationships between diffusion parameters and phosphorus precipitation during the pocl3 diffusion process,* Energy Procedia **38**, 254 (2013).

[39] A. Ebong, B. Rounsaville, I. B. Cooper, K. Tate, A. Upadhyaya, A. Rohatgi, B. Bunkenburg, J. Cathey, S. Kim, and D. Ruf, *Optimizing the inline emitters for higher efficiency silicon solar cells,* in *24th European Photovoltaic Solar Energy Conference. Hamburg, Germany: WIP-Renewable Energies* (2009).

[40] P. K. Basu, Z. Hameiri, D. Sarangi, J. Cunnusamy, E. Carmona, and M. B. Boreland, *18.7% efficient inline-diffused screen-printed silicon wafer solar cells with deep homogeneous emitter etch-back,* Solar energy materials and solar cells **117**, 412 (2013).

[41] F. Book, H. Knauss, C. Demberger, F. Mutter, and G. Hahn, *Phosphorous doping from apcvd deposited psg,* in *32nd European Photovoltaic Solar Energy Conference and Exhibition* (2016) pp. 824–827.

[42] H. Hieslmair, L. Mandrell, I. Latchford, M. Chun, J. Sullivan, and B. Adibi, *High throughput ion-implantation for silicon solar cells,* Energy Procedia **27**, 122 (2012).

[43] D. Kray, S. Hopman, A. Spiegel, B. Richerzhagen, and G. P. Willeke, *Study on the edge isolation of industrial silicon solar cells with waterjet-guided laser,* Solar Energy Materials and Solar Cells **91**, 1638 (2007).

[44] A. Hauser, G. Hahn, M. Spiegel, P. Fath, E. Bucher, H. Feist, O. Breitenstein, and J. P. Rakotoniaina, *Comparison of different techniques for edge isolation,* in *17th European photovoltaic solar energy conference* (2001) pp. 1739–1742.

[45] T. Dannenberg, J. Vollmer, M. Passig, C. Scheiwe, D. Brunner, A. Pediaditakis, U. Jäger, I. Wang, W. Xie, S. Xu, *et al.*, *Past, present, and future outlook for edge isolation processes in highly efficient silicon solar cell manufacturing,* Solar RRL , 2200594 (2022).

[46] H. Nagel, A. G. Aberle, and R. Hezel, *Optimised antireflection coatings for planar silicon solar cells using remote pecvd silicon nitride and porous silicon dioxide,* Progress in Photovoltaics: Research and Applications **7**, 245 (1999).

[47] A. G. Aberle, *Surface passivation of crystalline silicon solar cells: a review,* Progress in Photovoltaics: Research and Applications **8**, 473 (2000).

[48] J. Schmidt and M. Kerr, *Highest-quality surface passivation of low-resistivity p-type silicon using stoichiometric pecvd silicon nitride,* Solar Energy Materials and Solar Cells **65**, 585 (2001).

[49] J.-W. Jeong, A. Rohatgi, V. Yelundur, A. Ebong, M. D. Rosenblum, and J. P. Kalejs, *Enhanced silicon solar cell performance by rapid thermal firing of screen-printed metals,* IEEE transactions on electron devices **48**, 2836 (2001).

[50] S. Narasimha, A. Rohatgi, and A. Weeber, *An optimized rapid aluminum back surface field technique for silicon solar cells,* IEEE Transactions on Electron Devices **46**, 1363 (1999).

[51] L. Gong, F. Wang, Q. Cai, D. You, and B. Dai, *Characterization of defects in monolike silicon wafers and their effects on solar cell efficiency,* Solar energy materials and solar cells **120**, 289 (2014).

[52] M. M. Hilali, M. M. Al-Jassim, B. To, H. Moutinho, A. Rohatgi, and S. Asher, *Understanding the formation and temperature dependence of thick-film ag contacts on high-sheet-resistance si emitters for solar cells,* Journal of the Electrochemical Society **152**, G742 (2005).

[53] A. Ebong, I. Cooper, A. Rounsaville, A. Rohatgi, W. Borland, K. Mikeska, *et al.*, *Overcoming the technological challenges of contacting homogeneous high sheet resistance emitters (hhse),* in *26th European Photovoltaic Solar Energy Conference and Exhibition* (2011) pp. 1747–1749.

[54] M. Galiazzo, A. Voltan, E. Bortoletto, M. Zamuner, M. Martire, O. Borsato, M. Bertazzo, and D. Tonini, *Fine line double printing and advanced process control for cell manufacturing,* Energy Procedia **67**, 116 (2015).

[55] X. Ye, S. Zou, K. Chen, J. Li, J. Huang, F. Cao, X. Wang, L. Zhang, X.-F. Wang, M. Shen, *et al.*, *18.45%-efficient multi-crystalline silicon solar cells with novel nanoscale pseudo-pyramid texture,* Advanced Functional Materials **24**, 6708 (2014).

[56] G. Hahn, *Status of selective emitter technology,* in *25th European Photovoltaic Solar Energy Conference and Exhibition. 5th World Conference on photovoltaic Energy Conversion* (2010) pp. 1091–1096.

[57] S. Braun, G. Hahn, R. Nissler, C. Pönisch, and D. Habermann, *Multi-busbar solar cells and modules: high efficiencies and low silver consumption,* Energy Procedia **38**, 334 (2013).

[58] T. Fellmeth, S. Mack, J. Bartsch, D. Erath, U. Jäger, R. Preu, F. Clement, and D. Biro, *20.1% efficient silicon solar cell with aluminum back surface field,* IEEE Electron Device Letters **32**, 1101 (2011).

[59] K. H. Kim, C. S. Park, J. D. Lee, J. Y. Lim, J. M. Yeon, I. H. Kim, E. J. Lee, and Y. H. Cho, *Record high efficiency of screen-printed silicon aluminum back surface field solar cell: 20.29%,* Japanese Journal of Applied Physics **56**, 08MB25 (2017).

[60] Y. Chen, H. Shen, and P. P. Altermatt, *Analysis of recombination losses in screen-printed aluminum-alloyed back surface fields of silicon solar cells by numerical device simulation,* Solar energy materials and solar cells **120**, 356 (2014).

[61] T. Dullweber, C. Kranz, R. Peibst, U. Baumann, H. Hannebauer, A. Fülle, S. Steckemetz, T. Weber, M. Kutzer, M. Müller, *et al.*, *Perc+: industrial perc solar cells with rear al grid enabling bifaciality and reduced al paste consumption,* Progress in Photovoltaics: Research and Applications **24**, 1487 (2016).

[62] R. Kopecek and J. Libal, *Towards large-scale deployment of bifacial photovoltaics,* Nature Energy **3**, 443 (2018).

[63] R. Kopecek and J. Libal, *Bifacial photovoltaics 2021: Status, opportunities and challenges,* Energies **14**, 2076 (2021).

[64] M. A. Green, *The passivated emitter and rear cell (perc): From conception to mass production,* Solar Energy Materials and Solar Cells **143**, 190 (2015).

[65] A. Blakers, *Development of the perc solar cell,* IEEE Journal of Photovoltaics **9**, 629 (2019).

[66] S. Lohmüller, S. Schmidt, E. Lohmüller, A. Piechulla, U. Belledin, D. Herrmann, and A. Wolf, *Transfer of pocl3 diffusion processes from atmospheric pressure to high throughput low pressure,* in *AIP Conference Proceedings*, Vol. 1999 (AIP Publishing LLC, 2018) p. 070002.

[67] E. Cornagliotti, A. Uruena, J. Horzel, J. John, L. Tous, D. Hendrickx, V. Prajapati, S. Singh, R. Hoyer, F. Delahaye, *et al.*, *How much rear side polishing is required? a study on the impact of rear side polishing in perc solar cells,* in *27th European Photovoltaic Solar Energy Conference and Exhibition* (2012) pp. 561–566.

[68] C. Kranz, S. Wyczanowski, U. Baumann, K. Weise, C. Klein, F. Delahaye, T. Dullweber, and R. Brendel, *Wet chemical polishing for industrial type perc solar cells,* Energy Procedia **38**, 243 (2013).

[69] A. W. Blakers, A. Wang, A. M. Milne, J. Zhao, and M. A. Green, *22.8% efficient silicon solar cell,* Applied Physics Letters **55**, 1363 (1989).

[70] K. Münzer, M. Hein, J. Schöne, M. Hanke, A. Teppe, R. Schlosser, J. Maier, A. Yodyunyong, S. Krümberg, S. Keller, *et al.*, *Technical performance and industrial implementation in favour of centaurus technology,* Energy Procedia **27**, 631 (2012).

[71] S. Dauwe, L. Mittelstädt, A. Metz, and R. Hezel, *Experimental evidence of parasitic shunting in silicon nitride rear surface passivated solar cells,* Progress in Photovoltaics: Research and Applications **10**, 271 (2002).

[72] B. Hoex, J. Gielis, M. Van de Sanden, and W. Kessels, *On the c-si surface passivation mechanism by the negative-charge-dielectric al 2 o 3,* Journal of Applied physics **104**, 113703 (2008).

[73] P. Poodt, A. Lankhorst, F. Roozeboom, K. Spee, D. Maas, and A. Vermeer, *High-speed spatial atomic-layer deposition of aluminum oxide layers for solar cell passivation,* Advanced materials **22**, 3564 (2010).

[74] H. Sperlich, D. Decker, P. Saint-Cast, E. Erben, and L. Peters, *High productive solar cell passivation on roth&rau maia® mw-pecvd inline machine–a comparison of al2o3, sio2 and sinx-h process conditions and performance,* in *25th European Photovoltaic Solar Energy Conference and Exhibition, Valencia, Spain* (2010).

[75] L. E. Black, T. Allen, A. Cuevas, K. R. McIntosh, B. Veith, and J. Schmidt, *Thermal stability of silicon surface passivation by apcvd al2o3,* Solar Energy Materials and Solar Cells **120**, 339 (2014).

[76] T.-T. Li and A. Cuevas, *Effective surface passivation of crystalline silicon by rf sputtered aluminum oxide,* physica status solidi (RRL)–Rapid Research Letters **3**, 160 (2009).

[77] T. Dullweber, C. Kranz, B. Beier, B. Veith, J. Schmidt, B. Roos, O. Hohn, T. Dippell, and R. Brendel, *Inductively coupled plasma chemical vapour deposited alox/siny layer stacks for applications in high-efficiency industrial-type silicon solar cells,* Solar energy materials and solar cells **112**, 196 (2013).

[78] H. Profijt, S. Potts, M. Van de Sanden, and W. Kessels, *Plasma-assisted atomic layer deposition: basics, opportunities, and challenges,* Journal of Vacuum Science & Technology A: Vacuum, Surfaces, and Films **29**, 050801 (2011).

[79] J.-Y. Hung, J.-c. Wang, S.-w. Chen, T.-C. Chen, Y.-S. Lin, C.-H. Ku, and C.-C. Wen, *Back-side alox passivation material and technology for the application of high efficiency (20%) and low cost perc solar cells,* in *2014 IEEE 40th Photovoltaic Specialist Conference (PVSC)* (IEEE, 2014) pp. 3308–3312.

[80] B. Liao, X. Wu, W. Wu, C. Liu, S. Ma, S. Wang, T. Xie, Q. Wang, Z. Du, W. Shen, *et al.*, *Tube-type plasma-enhanced atomic layer deposition of aluminum oxide: Enabling record lab performance for the industry with demonstrated cell efficiencies> 24%,* Progress in Photovoltaics: Research and Applications **31**, 52 (2023).

[81] K. Neckermann, S. Correia, G. Andra, *et al.*, *Local structuring of dielectric layers on silicon for improved solar cell metallization,* Proc. 22nd EPVSEC, Milan (2007).

[82] E. Urrejola, K. Peter, H. Plagwitz, and G. Schubert, *Silicon diffusion in aluminum for rear passivated solar cells,* Applied Physics Letters **98**, 153508 (2011).

[83] C. Kranz, U. Baumann, B. Wolpensinger, F. Lottspeich, M. Müller, P. Palinginis, R. Brendel, and T. Dullweber, *Void formation in screen-printed local aluminum contacts modeled by surface energy minimization,* Solar Energy Materials and Solar Cells **158**, 11 (2016).

[84] B. J. Hallam, P. G. Hamer, A. M. Ciesla née Wenham, C. E. Chan, B. Vicari Stefani, and S. Wenham, *Development of advanced hydrogenation processes for silicon solar cells via an improved understanding of the behaviour of hydrogen in silicon,* Progress in Photovoltaics: Research and Applications **28**, 1217 (2020).

[85] D. C. Walter, T. Pernau, and J. Schmidt, *Ultrafast lifetime regeneration in an industrial belt-line furnace applying intense illumination at elevated temperature,* 32nd EU PVSEC (2016).

[86] C. Derricks, A. Herguth, G. Hahn, O. Romer, and T. Pernau, *Industrially applicable mitigation of bo-lid in cz-si perc-type solar cells within a coupled fast firing and halogen lamp based belt-line regenerator–a parameter study,* Solar Energy Materials and Solar Cells **195**, 358 (2019).

[87] A. Edler, M. Schlemmer, J. Ranzmeyer, and R. Harney, *Understanding and overcoming the influence of capacitance effects on the measurement of high efficiency silicon solar cells,* Energy Procedia **27**, 267 (2012).

[88] T. Fuyuki and A. Kitiyanan, *Photographic diagnosis of crystalline silicon solar cells utilizing electroluminescence,* Applied Physics A **96**, 189 (2009).

[89] M. Alt, S. Fischer, S. Schenk, S. Zimmermann, K. Ramspeck, and M. Meixner, *Electroluminescence imaging and automatic cell classification in mass production of silicon solar cells,* in *2018 IEEE 7th World Conference on Photovoltaic Energy Conversion (WCPEC)(A Joint Conference of 45th IEEE PVSC, 28th PVSEC & 34th EU PVSEC)* (IEEE, 2018) pp. 3298–3304.

[90] F. Kiefer, J. Krügener, F. Heinemeyer, M. Jestremski, H. Osten, R. Brendel, and R. Peibst, *Bifacial, fully screen-printed n-pert solar cells with bf2 and b implanted emitters,* Solar Energy Materials and Solar Cells **157**, 326 (2016).

[91] B. Terheiden, *Cvd boron containing glasses–an attractive alternative diffusion source for high quality emitters and simplified processing-a review,* Energy Procedia **92**, 486 (2016).

[92] C. Oliver, B. Semmache, Y. Cuminal, A. Foucaran, M. Gauthier, and Y. Pellegrin, *Implementation of boron emitters using bcl3 diffusion process for industrial silicon solar cells fabrication,* in *25th European Photovoltaic Solar Energy Conference*

and Exhibition. 5th World Conference on photovoltaic Energy Conversion (2010) pp. 1930–1933.

[93] V. Shanmugam, N. Chen, X. Yan, A. Khanna, B. Nagarajan, J. Rodriguez, N. Nandakumar, H. Knauss, H. Haverkamp, A. Aberle, *et al.*, *Impact of the manufacturing process on the reverse-bias characteristics of high-efficiency n-type bifacial silicon wafer solar cells,* Solar Energy Materials and Solar Cells **191**, 117 (2019).

[94] B. Liao, W. Wu, R. J. Yeo, X. Wu, S. Ma, Q. Wang, Y. Wan, X. Su, W. Shen, X. Li, *et al.*, *Atomic scale controlled tunnel oxide enabled by a novel industrial tube-based peald technology with demonstrated commercial topcon cell efficiencies> 24%,* Progress in Photovoltaics: Research and Applications (2022).

[95] F. Feldmann, T. Fellmeth, B. Steinhauser, H. Nagel, D. Ourinson, S. Mack, E. Lohmüller, J. Polzin, J. Benick, A. Richter, *et al.*, *Large area topcon cells realized by a pecvd tube process,* in *36th European Photovoltaic Solar Energy Conference and Exhibition* (2019) pp. 304–308.

[96] N. Nandakumar, J. Rodriguez, T. Kluge, T. Grosse, D. Landgraf, N. Balaji, M. Esber, P. Padhamnath, and S. Duttagupta, *21.6% monopoly tm cells with in-situ interfacial oxide and poly-si layers deposited by inline pecvd,* in *2018 IEEE 7th World Conference on Photovoltaic Energy Conversion (WCPEC)(A Joint Conference of 45th IEEE PVSC, 28th PVSEC & 34th EU PVSEC)* (IEEE, 2018) pp. 2048–2051.

[97] J. Temmler, J.-I. Polzin, F. Feldmann, L. Kraus, B. Kafle, S. Mack, A. Moldovan, M. Hermle, and J. Rentsch, *Inline pecvd deposition of poly-si-based tunnel oxide passivating contacts,* physica status solidi (a) **215**, 1800449 (2018).

[98] V. D. Mihailetchi, H. Chu, J. Lossen, and R. Kopecek, *Surface passivation of boron-diffused junctions by a borosilicate glass and in situ grown silicon dioxide interface layer,* IEEE Journal of Photovoltaics **8**, 435 (2018).

[99] B. Kafle, B. S. Goraya, S. Mack, F. Feldmann, S. Nold, and J. Rentsch, *Topcon–technology options for cost efficient industrial manufacturing,* Solar Energy Materials and Solar Cells **227**, 111100 (2021).

[100] D. Ding, Z. Du, R. Liu, C. Quan, J. Bao, D. Du, Z. Li, J. Chen, and W. Shen, *Laser doping selective emitter with thin borosilicate glass layer for n-type topcon c-si solar cells,* Solar Energy Materials and Solar Cells **253**, 112230 (2023).

[101] V. Shaw, *Jinkosolar achieves 26.4% efficiency for n-type topcon solar cell,* (accessed on 14/03/2023).

[102] M. Hermle, F. Feldmann, M. Bivour, J. C. Goldschmidt, and S. W. Glunz, *Passivating contacts and tandem concepts: Approaches for the highest silicon-based solar cell efficiencies,* Applied Physics Reviews **7**, 021305 (2020).

[103] R. Kopecek, F. Buchholz, V. D. Mihailetchi, J. Libal, J. Lossen, N. Chen, H. Chu, C. Peter, T. Timofte, A. Halm, *et al.*, *Interdigitated back contact technology as final*

evolution for industrial crystalline single-junction silicon solar cell, in *Solar*, Vol. 3 (MDPI, 2022) pp. 1–14.

[104] S. Rai-Roche, *Longi launches new hi-mo 6 hpbc module for distributed generation market,* (accessed on 14/02/2023).

[105] T. news, *Aiko solar subsidiary unveils silver free abc solar modules with back-junction back contacts and maximum efficiency of 23.5%,* (accessed on 14/02/2023).

[106] D. M. Chapin, C. S. Fuller, and G. L. Pearson, *A new silicon p-n junction photocell for converting solar radiation into electrical power,* Journal of applied physics **25**, 676 (1954).

[107] D. Chapin, C. Fuller, and G. Pearson, *Solar energy converting apparatus,* Patent US2780765 (1954).

[108] R. Schwartz and M. Lammert, *Silicon solar cells for high concentration applications,* in *1975 International Electron Devices Meeting* (IEEE, 1975) pp. 350–352.

[109] D. D. Smith, G. Reich, M. Baldrias, M. Reich, N. Boitnott, and G. Bunea, *Silicon solar cells with total area efficiency above 25%,* in *2016 IEEE 43rd photovoltaic specialists conference (PVSC)* (IEEE, 2016) pp. 3351–3355.

[110] K. Yoshikawa, W. Yoshida, T. Irie, H. Kawasaki, K. Konishi, H. Ishibashi, T. Asatani, D. Adachi, M. Kanematsu, H. Uzu, *et al.*, *Exceeding conversion efficiency of 26% by heterojunction interdigitated back contact solar cell with thin film si technology,* Solar Energy Materials and Solar Cells **173**, 37 (2017).

[111] M. Dahlinger, K. Carstens, E. Hoffmann, R. Zapf-Gottwick, and J. H. Werner, *23.2% laser processed back contact solar cell: fabrication, characterization and modeling,* Progress in Photovoltaics: Research and Applications **25**, 192 (2017).

[112] Y. Yang, *Recent progress at trinasolar in large area ibc cells with passivating contact,* in *nPV workshop, Lausanne* (2018).

[113] F. Haase, C. Hollemann, S. Schäfer, A. Merkle, M. Rienäcker, J. Krügener, R. Brendel, and R. Peibst, *Laser contact openings for local poly-si-metal contacts enabling 26.1%-efficient polo-ibc solar cells,* Solar Energy Materials and Solar Cells **186**, 184 (2018).

[114] G. Yang, P. Guo, P. Procel, G. Limodio, A. Weeber, O. Isabella, and M. Zeman, *High-efficiency black ibc c-si solar cells with poly-si as carrier-selective passivating contacts,* Solar Energy Materials and Solar Cells **186**, 9 (2018).

[115] T. C. Kho, K. C. Fong, M. Stocks, K. McIntosh, E. Franklin, S. P. Phang, W. Liang, and A. Blakers, *Excellent ono passivation on phosphorus and boron diffusion demonstrating a 25% efficient ibc solar cell,* Progress in Photovoltaics: Research and Applications **28**, 1034 (2020).

[116] A. Descoeudres, J. Horzel, B. Paviet-Salomon, L.-L. Senaud, G. Christmann, J. Geissbühler, P. Wyss, N. Badel, J.-W. Schüttauf, J. Zhao, *et al.*, *The versatility of passivating carrier-selective silicon thin films for diverse high-efficiency screen-printed heterojunction-based solar cells,* Progress in Photovoltaics: Research and Applications **28**, 569 (2020).

[117] B. Min, L. Nasebandt, C. Hollemann, D. Bredemeier, L. Thielmann, T. Brendemühl, R. Peibst, and R. Brendel, *23.1%-efficient polo back junction solar cell,* in *WCPEC-8, Milan, Italy* (2022).

[118] J. Linke, F. Buchholz, C. Peter, J. Hoß, J. Lossen, V. Mihailetchi, and R. Kopecek, *Fully passivating contact ibc solar cells using laser processing,* in *WCPEC-8, Milan, Italy* (2022).

[119] F. Buchholz, G. Galbiati, A. Edler, E. Wefringhaus, B. Ferstl, and M. Ross, *Comparison of wafer cleaning procedures for high efficiency n-type solar cells,* in *Proceedings of the 28th European Photovoltaic Solar Energy Conference and Exhibition* (2013).

[120] G. Galbiati, V. Mihailetchi, A. Halm, R. Roescu, and R. Kopecek, *Results on n-type ibc solar cells using industrial optimized techniques in the fabrication processing,* Energy Procedia **8**, 421 (2011).

[121] T. Dullweber, V. Mertens, M. Stöhr, J. Langlois, L. Mettner, U. Baumann, F. Haase, R. Brendel, J. Libal, A. Hähnel, A. Müller, V. Naumann, A. Vogt, N. Ambrosius, T. Pernau, and H. Haverkamp, *Towards cost-effective high-efficiency polo ibc solar cells with minimal conversion invest for existing perc+ production lines,* in *Proceedings of the 8th World Conference on Photovoltaic Energy Conversion* (Milano, Italy, 2022) pp. 35 – 39.

[122] P. Aschenbrenner, D. H. Rose, S. G. Daroczi, S. J. Coughlin, and C. F. Gay, *Interconnection of solar cells in a solar cell module,* (2008), uS Patent 7,390,961.

[123] LG, *Lg home energy solution,* (accessed on 10/02/2023).

[124] A. Faes, B. Paviet-Salomon, A. Tomasi, D. Lachenal, N. Badel, G. Christmann, L. Barraud, A. Descoeudres, J. Geissbühler, A. Lachowicz, *et al.*, *Multi-wire interconnection of back-contacted silicon heterojunction solar cells,* in *7th Workshop on Metallization & Interconnection for Crystalline Silicon Solar Cells, Konstanz, Germany* (2017) pp. 22–23.

[125] R. Van Dyck, T. Borgers, J. Govaerts, J. Poortmans, and A. W. Van Vuure, *Three-dimensional multi-ribbon interconnection for back-contact solar cells,* Progress in Photovoltaics: Research and Applications **29**, 507 (2021).

[126] M. Späth, B. Semmache, P. de Jong, I. Bennett, T. Visser, J. Bakker, and A. Verschoor, *First experiments on module assembly line using back-contact solar cells,* in *23rd European Photovoltaic Solar Energy Conference and Exhibition* (2008) pp. 2917–2921.

[127] K. Fisher, D. Levy, X. Meng, M. Woodhouse, J. Oh, T. Tamizhmani, M. Bertoni, D. Flood, and Z. Holman, *Method for fabrication of low-cost, back-contacted modules with aluminum conductive backsheets and double-glass encapsulation,* in *Poster presentation at 7th Workshop on Metallization and Interconnection for Crystalline Silicon Solar Cells* (2017).

[128] A. Halm, *Status of zebra cell and module development,* in *8th Back Contact Workshop, Freiburg* (2017).

[129] J. Walter, L. C. Rendler, A. Halm, V. Mihailetchi, A. Kraft, and U. Eitner, *Ribbon interconnection of 6" bc-bj solar cells,* Energy Procedia **124**, 504 (2017).

[130] A. Halm, *Achieving uniform module appearance while increasing module efficiency: the full gapless module concept for stringed ibc solar cells,* in *WCPEC-8, Milan, Italy* (2022).

[131] M. Assembly, *50 mw turnkey lines for pv module manufacturing,* (accessed on 13/03/2023).

[132] D. E. Carlson, *Laser processing of solar cells,* in *Laser Material Processing for Solar Energy*, Vol. 8473 (SPIE, 2012) pp. 3–11.

[133] B. Hallam, A. Urueña, R. Russell, M. Aleman, M. Abbott, C. Dang, S. Wenham, L. Tous, and J. Poortmans, *Efficiency enhancement of i-perc solar cells by implementation of a laser doped selective emitter,* Solar energy materials and solar cells **134**, 89 (2015).

[134] D. Kray, A. Fell, S. Hopman, K. Mayer, G. Willeke, and S. Glunz, *Laser chemical processing (lcp)—a versatile tool for microstructuring applications,* Applied Physics A **93**, 99 (2008).

[135] D. Kray, M. Aleman, A. Fell, S. Hopman, K. Mayer, M. Mesec, R. Muller, G. Willeke, S. Glunz, B. Bitnar, *et al.*, *Laser-doped silicon solar cells by laser chemical processing (lcp) exceeding 20% efficiency,* in *2008 33rd IEEE Photovoltaic Specialists Conference* (IEEE, 2008) pp. 1–3.

[136] J. Lossen, M. Matusovsky, A. Noy, C. Maier, and M. Bähr, *Pattern transfer printing (ptptm) for c-si solar cell metallization,* Energy Procedia **67**, 156 (2015).

[137] A. Adrian, D. Rudolph, N. Willenbacher, and J. Lossen, *Finger metallization using pattern transfer printing technology for c-si solar cell,* IEEE Journal of Photovoltaics **10**, 1290 (2020).

[138] D. Ourinson, G. Emanuel, K. Rahmanpour, F. Ogiewa, H. Müller, E. Krassowski, H. Höffler, F. Clement, and S. W. Glunz, *Laser-powered co-firing process for highly efficient si solar cells,* IEEE Journal of Photovoltaics **11**, 282 (2021).

[139] L. Song, A. Wenham, S. Wang, P. Hamer, M. S. Ahmmed, B. Hallam, L. Mai, M. Abbott, E. R. Hawkes, C. Chong, *et al.*, *Laser enhanced hydrogen passivation of silicon wafers,* International Journal of Photoenergy **2015** (2015).

[140] Clark-MXR, *Ultrafast laser micromachining handbook,* (accessed on 13/03/2023).

[141] H.-U. Zuhlke, *Thermal laser separation for wafer dicing,* Solid State Technology **52**, 24 (2009).

[142] S. Eiternick, F. Kaule, H.-U. Zühlke, T. Kießling, M. Grimm, S. Schoenfelder, and M. Turek, *High quality half-cell processing using thermal laser separation,* Energy Procedia **77**, 340 (2015).

[143] B. Martel, M. Albaric, S. Harrison, F. Dhainaut, and T. Desrues, *Addressing separation and edge passivation challenges for high efficiency shingle heterojunction solar cells,* Solar Energy Materials and Solar Cells **250**, 112095 (2023).

[144] F. Kaule, M. Pander, M. Turek, M. Grimm, E. Hofmueller, and S. Schoenfelder, *Mechanical damage of half-cell cutting technologies in solar cells and module laminates,* in *AIP Conference Proceedings*, Vol. 1999 (AIP Publishing LLC, 2018) p. 020013.

[145] C. Zhang, H. Shen, H. Liu, W. Zhang, J. Chen, and H. Li, *Influence of laser condition on the electrical and mechanical performance of bifacial half-cutting perc solar cell and module,* International Journal of Energy Research **46**, 15290 (2022).

[146] J. I. Biegeleisen, *The complete book of silk screen printing production* (Courier Corporation, 2012).

[147] L. Ney, S. Tepner, N. Wengenmeyr, M. Linse, A. Lorenz, S. Bechmann, R. Weber, M. Pospischil, and F. Clement, *Optimization of fine line screen printing using in-depth screen mesh analysis,* in *AIP Conference Proceedings*, Vol. 2156 (AIP Publishing LLC, 2019) p. 020006.

[148] Y. Zhang, L. Zhang, L. Jiang, L. Song, C. Guo, V. Dua, H. Yang, E. Kim, C. Chen, and H. P. M. N. A. Conshohocken, *Knotless screen printing for crystalline silicon solar cells,* in *Proceedings of 7th Workshop on Metallization; Konstanz* (2017).

[149] T. Wenzel, A. Lorenz, E. Lohmüller, S. Auerbach, K. Masuri, Y. C. Lau, S. Tepner, and F. Clement, *Progress with screen printed metallization of silicon solar cells - towards 20 μm line width and 20 mg silver laydown for perc front side contacts,* Solar Energy Materials and Solar Cells **244** (2022).

[150] E. Lohmüller, J. Weber, M. Demant, S. Lohmüller, S. Gutscher, P. Saint-Cast, and A. Wolf, *High-precision alignment procedures for patterning processes in solar cell production,* Progress in Photovoltaics: Research and Applications **28**, 189 (2020).

[151] K. Ramspeck, S. Schenk, L. Komp, A. Metz, and M. Meixner, *Accurate efficiency measurements on very high efficiency silicon solar cells using pulsed light sources,* in *29th European Photovoltaic Solar Energy Conference and Exhibition* (2014) pp. 1253–2356.

[152] A. C. Ronald A. Sinton, *A quasi-steady-state open-circuit voltage method for solar cell characterization,* in *16th European Photovoltaic Solar Energy Conference* (2000) p. 1152–1155.

[153] D. D. Tune, F. Buchholz, I. Ullman, and A. Halm, *Measuring and mitigating edge recombination in modules employing cut cells,* in *Proc. 37th Eur. Photovolt. Sol. Energy Conf.* (2020) pp. 322–328.

[154] H. Stolzenburg, A. Fell, F. Schindler, W. Kwapil, A. Richter, P. Baliozian, and M. C. Schubert, *Edge recombination analysis of silicon solar cells using photoluminescence measurements,* in *AIP Conference Proceedings*, Vol. 2147 (AIP Publishing LLC, 2019) p. 020017.

[155] K. C. Fong, M. Padilla, A. Fell, E. Franklin, K. R. McIntosh, T. C. Kho, A. W. Blakers, Y. Nebel-Jacobsen, and S. R. Surve, *Perimeter recombination characterization by luminescence imaging,* IEEE Journal of Photovoltaics **6**, 244 (2015).

[156] E. list of ISC Konstanz, *Emissions gap report 2022,* (accessed on 25/02/2023).

[157] S. Guo, J. Singh, I. Peters, A. Aberle, and T. Walsh, *A quantitative analysis of photovoltaic modules using halved cells,* International Journal of Photoenergy **2013** (2013).

[158] J. Müller, D. Hinken, S. Blankemeyer, H. Kohlenberg, U. Sonntag, K. Bothe, T. Dullweber, M. Köntges, and R. Brendel, *Resistive power loss analysis of pv modules made from halved 15.6× 15.6 cm 2 silicon perc solar cells with efficiencies up to 20.0%,* IEEE Journal of Photovoltaics **5**, 189 (2014).

[159] K. Brecl, M. Bokalič, and M. Topič, *Annual energy losses due to partial shading in pv modules with cut wafer-based si solar cells,* Renewable Energy **168**, 195 (2021).

[160] M. Mittag, A. Pfreundt, and J. Shahid, *Impact of solar cell dimensions on module power, efficiency and cell-to-module losses,* in *Proceedings of the 30th PV Solar Energy Conference (PVSEC-30), Jeju, Korea* (2020) pp. 1–6.

[161] D. Rudolph, J. Rabanal-Arabach, I. Ullmann, A. Halm, A. Schneider, and T. Fischer, *Cell design optimization for shingled modules,* Simulation **26**, 880 (2003).

[162] M. Oswald, M. Turek, J. Schneider, and S. Schoenfelder, *Evaluation of silicon solar cell separation techniques for advanced module concepts,* 28th European Photovoltaic Solar Energy Conference and Exhibition **29** (2013).

[163] J. Lelièvre, S. Harrison, M. Albaric, L. Carton, B. Portaluppi, and V. Barth, *Alternative cz ingot squaring and half-cell cutting methodology for low-temperature pv cell and module technologies,* in *Proc. 37th Eur. Photovolt. Sol. Energy Conf.* (2020) pp. 487–489.

[164] A. Münzer, P. Baliozian, A. Steinmetz, T. Geipel, S. Pingel, A. Richter, S. Roder, E. Lohmüller, A. Spribille, and R. Preu, *Post-separation processing for silicon heterojunction half solar cells with passivated edges,* IEEE Journal of Photovoltaics **11**, 1343 (2021).

[165] L. Xia, J. Chen, K. Liao, L. Huang, Q. Li, and X. Luo, *Influence of laser cutting conditions on electrical characteristics of half-size bifacial silicon solar cells,* Materials Science in Semiconductor Processing **105**, 104747 (2020).

[166] F. Gérenton, J. Eymard, S. Harrison, R. Clerc, and D. Munoz, *Analysis of edge losses on silicon heterojunction half solar cells,* Solar Energy Materials and Solar Cells **204**, 110213 (2020).

[167] P. Baliozian, A. Münzer, E. Lohmüller, A. Nair, T. Fellmeth, N. Wöhrle, H. Höffler, A. Spribille, and R. Preu, *Thermal laser separation of perc and shj solar cells,* IEEE Journal of Photovoltaics **11**, 259 (2021).

[168] P. Baliozian, M. Al-Akash, E. Lohmüller, A. Richter, T. Fellmeth, A. Münzer, N. Wöhrle, P. Saint-Cast, H. Stolzenburg, A. Spribille, *et al.*, *Postmetallization "passivated edge technology" for separated silicon solar cells,* IEEE Journal of Photovoltaics **10**, 390 (2020).

[169] S. Harrison, B. Portaluppi, P. Bertrand, V. Giglia, B. Martel, A. Sekkat, and D. Munoz-Rojas, *Low temperature post-process repassivation for heterojunction cut-cells,* in *Proc. 38th Eur. Photovolt. Sol. Energy Conf.* (2021) pp. 167–171.

[170] D. König and G. Ebest, *New contact frame design for minimizing losses due to edge recombination and grid-induced shading,* Solar energy materials and solar cells **75**, 381 (2003).

[171] S. Glunz, J. Dicker, M. Esterle, M. Hermle, J. Isenberg, F. Kamerewerd, J. Knobloch, D. Kray, A. Leimenstoll, F. Lutz, *et al.*, *High-efficiency silicon solar cells for low-illumination applications,* in *Conference Record of the Twenty-Ninth IEEE Photovoltaic Specialists Conference, 2002.* (IEEE, 2002) pp. 450–453.

[172] K. Rühle, M. K. Juhl, M. D. Abbott, L. M. Reindl, and M. Kasemann, *Impact of edge recombination in small-area solar cells with emitter windows,* IEEE Journal of Photovoltaics **5**, 1067 (2015).

[173] C. Chan, M. Abbott, B. Hallam, M. Juhl, D. Lin, Z. Li, Y. Li, J. Rodriguez, and S. Wenham, *Edge isolation of solar cells using laser doping,* Solar Energy Materials and Solar Cells **132**, 535 (2015).

[174] R. Kopecek, J. Libal, J. Lossen, V. D. Mihailetchi, H. Chu, C. Peter, F. Buchholz, E. Wefringhaus, A. Halm, J. Ma, *et al.*, *Zebra technology: low cost bifacial ibc solar cells in mass production with efficiency exceeding 23.5%,* in *2020 47th IEEE Photovoltaic Specialists Conference (PVSC)* (IEEE, 2020) pp. 1008–1012.

[175] G. Galbiati, H. Chu, V. D. Mihailetchi, J. Libal, and R. Kopecek, *Latest results in screen-printed ibc-zebra solar cells,* in *2018 IEEE 7th World Conference on Photovoltaic Energy Conversion (WCPEC)(A Joint Conference of 45th IEEE PVSC, 28th PVSEC & 34th EU PVSEC)* (IEEE, 2018) pp. 1540–1543.

[176] N. Chen, D. Tune, F. Buchholz, A. Halm, and V. Mihailetchi, *Impact of cut edge recombination in high efficiency solar cells–measurement and mitigation strategies,* in *Proc. 38th Eur. Photovolt. Sol. Energy Conf.* (2021) pp. 253–256.

[177] R. A. Sinton, A. Cuevas, *et al.*, *A quasi-steady-state open-circuit voltage method for solar cell characterization,* in *16th European photovoltaic solar energy conference,* Vol. 1152 (2000) p. 4.

[178] M. Hermle, J. Dicker, W. Warta, S. Glunz, and G. Willeke, *Analysis of edge recombination for high-efficiency solar cells at low illumination densities,* in *3rd World Conference onPhotovoltaic Energy Conversion, 2003. Proceedings of,* Vol. 2 (IEEE, 2003) pp. 1009–1012.

[179] P. Grunow, S. Lust, D. Sauter, V. Hoffmann, C. Beneking, B. Litzenburger, and L. Podlowski, *Weak light performance and annual yields of pv modules and systems as a result of the basic parameter set of industrial solar cells,* in *19th European Photovoltaic Solar Energy Conference,* June (sn, 2004) pp. 2190–2193.

[180] M. Abbott, J. Cotter, T. Trupke, and R. Bardos, *Investigation of edge recombination effects in silicon solar cell structures using photoluminescence,* Applied physics letters **88**, 114105 (2006).

[181] A. Fell, J. Schön, M. Müller, N. Wöhrle, M. C. Schubert, and S. W. Glunz, *Modeling edge recombination in silicon solar cells,* IEEE Journal of Photovoltaics **8**, 428 (2018).

[182] R. Kühn, A. Boueke, M. Wibral, C. Zechner, P. Fath, G. Willeke, and E. Bucher, *Investigation of the effect of p/n-junctions bordering on the surface of silicon solar cells,* in *Proc. 2nd WCPSEC* (1998) p. 1390.

[183] A. Münzer, P. Baliozian, K. Ahmed, A. Nair, E. Lohmüller, T. Fellmeth, A. Spribille, and R. Preu, *Laser assisted separation processes for bifacial pspeer shingle solar cells,* in *37th European PV Solar Energy Conference and Exhibition,* Vol. 7 (2020) p. 11.

[184] B. Hoex, J. Schmidt, P. Pohl, M. Van de Sanden, and W. Kessels, *Silicon surface passivation by atomic layer deposited al 2 o 3,* Journal of Applied Physics **104**, 044903 (2008).

[185] F. Feldmann, M. Bivour, C. Reichel, M. Hermle, and S. W. Glunz, *Passivated rear contacts for high-efficiency n-type si solar cells providing high interface passivation quality and excellent transport characteristics,* Solar energy materials and solar cells **120**, 270 (2014).

[186] S. De Wolf, A. Descoeudres, Z. C. Holman, and C. Ballif, *High-efficiency silicon heterojunction solar cells: A review,* green **2**, 7 (2012).

[187] J. Wong, R. Sridharan, and V. Shanmugam, *Quantifying edge and peripheral recombination losses in industrial silicon solar cells,* IEEE Transactions on Electron Devices **62**, 3750 (2015).

[188] A. Fell and P. P. Altermatt, *Detailed 3d full-cell modeling in quokka3: Quantifying edge and solder-pad losses in an industrial perc cell,* in *AIP Conference Proceedings,* Vol. 1999 (AIP Publishing LLC, 2018) p. 020007.

[189] V. Giglia, R. Varache, J. Veirman, and E. Fourmond, *Influence of cell edges on the performance of silicon heterojunction solar cells,* Solar Energy Materials and Solar Cells **238**, 111605 (2022).

[190] S. Schäfer, F. Haase, C. Hollemann, J. Hensen, J. Krügener, R. Brendel, and R. Peibst, *26%-efficient and 2 cm narrow interdigitated back contact silicon solar cells with passivated slits on two edges,* Solar Energy Materials and Solar Cells **200**, 110021 (2019).

[191] N. Chen, F. Buchholz, D. D. Tune, O. Isabella, and V. D. Mihailetchi, *Mitigating cut losses in interdigitated back contact solar cells,* IEEE Journal of Photovoltaics **12**, 1386 (2022).

[192] H. Han, X. Jia, C. Ma, and Y. Wu, *A novel laser scribing method combined with the thermal stress cleaving for the crystalline silicon solar cell separation in mass production,* Solar Energy Materials and Solar Cells **240**, 111714 (2022).

[193] D. Biro and W. Warta, *German patent,* (1998), dE198 57 064.3-33.

[194] D. Biro and W. Warta, *Low temperature passivation of silicon surfaces by polymer films,* Solar Energy Materials and Solar Cells **71**, 369 (2002).

[195] J. Bullock, D. Kiriya, N. Grant, A. Azcatl, M. Hettick, T. Kho, P. Phang, H. C. Sio, D. Yan, D. Macdonald, *et al.*, *Superacid passivation of crystalline silicon surfaces,* ACS Applied Materials & Interfaces **8**, 24205 (2016).

[196] J. Hossain, Q. Liu, T. Miura, K. Kasahara, D. Harada, R. Ishikawa, K. Ueno, and H. Shirai, *Nafion-modified pedot: Pss as a transparent hole-transporting layer for high-performance crystalline-si/organic heterojunction solar cells with improved light soaking stability,* ACS Applied Materials & Interfaces **8**, 31926 (2016).

[197] J. Chen, K. Ge, C. Zhang, J. Guo, L. Yang, D. Song, F. Li, Z. Xu, Y. Xu, and Y. Mai, *Vacuum-free, room-temperature organic passivation of silicon: Toward very low recombination of micro-/nanotextured surface structures,* ACS applied materials & interfaces **10**, 44890 (2018).

[198] I. Jeon, C. Delacou, H. Okada, G. E. Morse, T.-H. Han, Y. Sato, A. Anisimov, K. Suenaga, E. I. Kauppinen, S. Maruyama, *et al.*, *Polymeric acid-doped transparent carbon nanotube electrodes for organic solar cells with the longest doping durability,* Journal of Materials Chemistry A **6**, 14553 (2018).

[199] W. Ji, Y. Zhao, H. M. Fahad, J. Bullock, T. Allen, D.-H. Lien, S. De Wolf, and A. Javey, *Dip coating passivation of crystalline silicon by lewis acids,* ACS nano **13**, 3723 (2019).

[200] D. D. Tune, N. Mallik, H. Fornasier, and B. S. Flavel, *Breakthrough carbon nanotube–silicon heterojunction solar cells,* Advanced Energy Materials **10**, 1903261 (2020).

[201] J. Chen, D. D. Tune, K. Ge, H. Li, and B. S. Flavel, *Front and back-junction carbon nanotube-silicon solar cells with an industrial architecture,* Advanced Functional Materials **30**, 2000484 (2020).

[202] J. Chen, L. Wan, H. Li, J. Yan, J. Ma, B. Sun, F. Li, and B. S. Flavel, *A polymer/carbon-nanotube ink as a boron-dopant/inorganic-passivation free carrier selective contact for silicon solar cells with over 21% efficiency,* Advanced Functional Materials **30**, 2004476 (2020).

[203] W. Li, X. Wang, J. Guo, X. Zhang, B. Chen, J. Chen, Q. Gao, X. Yang, F. Li, J. Wang, *et al.*, *Compensating cutting losses by passivation solution for industry upgradation of topcon and shj solar cells,* Advanced Energy and Sustainability Research , 2200154 (2022).

[204] K. Chen, S. Agarwal, A. R. Meyer, H. Guthrey, W. Nemeth, S. Theingi, M. Page, D. L. Young, and P. Stradins, *Nafion Passivation of c-Si Surface and Edge for Electron Paramagnetic Resonance*, Tech. Rep. (National Renewable Energy Lab.(NREL), Golden, CO (United States), 2022).

[205] R. Kopecek, J. Libal, J. Lossen, V. D. Mihailetchi, H. Chu, C. Peter, F. Buchholz, E. Wefringhaus, A. Halm, J. Ma, L. Jianda, G. Yonggang, Q. Xiaoyong, W. Xiang, and D. Peng, *Zebra technology: low cost bifacial ibc solar cells in mass production with efficiency exceeding 23.5%,* (IEEE, 2020).

[206] T. Trupke, R. Bardos, M. Schubert, and W. Warta, *Photoluminescence imaging of silicon wafers,* Applied Physics Letters **89**, 044107 (2006).

[207] L. Tous, J. Govaert, S. Harrison, C. Carrière, V. Barth, V. Giglia, F. Buchholz, N. Chen, A. Halm, A. Faes, *et al.*, *Overview of key results achieved in h2020 highlite project helping to raise the eu pv industries' competitiveness,* Progress in Photovoltaics: Research and Applications (2023).

[208] pv magazine, *World has installed 1tw of solar capacity,* (accessed on 14/03/2023).

[209] pv magazine, *Global annual solar deployment to hit 1 tw by 2030,* (accessed on 14/03/2023).

[210] R. Kopecek and J. Libal, *bifipv2022 status and future: Entering the bifacial npv era,* Photovoltaics International **48**, 60 (2022).

[211] A. Adrian, D. Rudolph, N. Willenbacher, and J. Lossen, *Finger metallization using pattern transfer printing technology for c-si solar cell,* IEEE Journal of Photovoltaics **10**, 1290 (2020).

[212] A. Lorenz, M. Klawitter, M. Linse, L. Ney, S. Tepner, S. Pingel, M. S. Sabet, J. Reiner, K. Oehrle, R. Greutmann, J. Röth, M. Drews, K. Muramatsu, S.-i. Ikarashi, and F. Clement, *Rotary screen printed metallization of heterojunction solar cells: Toward high-throughput production with very low silver laydown,* Energy Technology **10** (2022).

[213] J. Schube, T. Fellmeth, M. Jahn, R. Keding, and S. W. Glunz, *Inkjet- and flextrail-printing with low silver consumption for silicon heterojunction solar cells,* physica status solidi (RRL) – Rapid Research Letters **13** (2019).

[214] M. Pospischil, T. Riebe, A. Jimenez, M. Kuchler, S. Tepner, T. Geipel, D. Ourinson, T. Fellmeth, M. Breitenbücher, T. Buck, M. Dhamrin, and F. Clement, *Applications of parallel dispensing in pv metallization,* AIP Conference Proceedings **2156**, 020005 (2019).

[215] K. Gensowski, M. Much, E. Bujnoch, S. Spahn, S. Tepner, and F. Clement, *Filament stretching during micro-extrusion of silver pastes enables an improved fine-line silicon solar cell metallization,* Sci Rep **12**, 12318 (2022).

[216] S. Whitepaper, *SunPower® Module 40-year Useful Life*, Report (SunPower Corporation, 2013).

[217] C. Han, G. Yang, P. Procel, D. O'Connor, Y. Zhao, A. Gopalakrishnan, X. Zhang, M. Zeman, L. Mazzarella, and O. Isabella, *Controllable simultaneous bifacial cu-plating for high-efficiency crystalline silicon solar cells,* Solar RRL **6** (2022).

[218] B. Grübel, G. Cimiotti, C. Schmiga, S. Schellinger, B. Steinhauser, A. A. Brand, M. Kamp, M. Sieber, D. Brunner, S. Fox, and S. Kluska, *Progress of plated metallization for industrial bifacial topcon silicon solar cells,* Progress in Photovoltaics: Research and Applications **30**, 615 (2021).

[219] pv magazine, *Sundrive achieves 26.41% efficiency with copper-based solar cell tech,* (accessed on 14/03/2023).

[220] J. Shin, H. Kim, K. H. Song, and J. Choe, *Synthesis of silver-coated copper particles with thermal oxidation stability for a solar cell conductive paste,* Chemistry Letters **44**, 1223 (2015).

[221] S. Yoshiba, M. Dhamrin, M. Yoshida, A. Uzum, , U. Itoh, H. Tokuhisa, S. Sekine, T. Saitoh, and K. Kamisako, *Cost-effective front contact metalization by copper paste for screen-printed crystalline silicon solar cells,* in *27th European Photovoltaic Solar Energy Conference and Exhibition* (2012) pp. 1730–1732.

[222] D. Wood, I. Kuzma-Filipek, R. Russell, F. Duerinckx, N. Powell, A. Zambova, B. Chislea, P. Chevalier, C. Boulord, A. Beucher, N. Zeghers, W. Deng, Z. Feng, P. Verlinden, J. Szlufcik, and G. Beaucarne, *Passivated busbars from screen-printed low-temperature copper paste,* Energy Procedia **55**, 724 (2014).

[223] T. Druffel, R. Dharmadasa, K. Ankireddy, K. Elmer, A. Ebong, and S. Huneycutt, *Copper based front side metalization contacts screen printed and fired in air demonstrating durability,* in *47th IEEE Photovoltaic Specialists Conference (PVSC)* (IEEE, 2020).

[224] K. Gawlinska-Necek, R. P. Socha, P. Balawender, M. K. Stodolny, B. B. Van Aken, Z. Starowicz, and P. Panek, *Silicon solar cells and modules with front contact paste containing copper-based component,* Progress in Photovoltaics: Research and Applications **29**, 1008 (2021).

[225] D. Rudolph, R. Farneda, T. Timofte, A. Halm, N. Chen, J. Libal, F. Buchholz, I. Rosen, M. Grouchko, and O. Shochet, *Screen printable, non-fire-through copper paste applied as busbar metallization for back contact solar cells,* AIP Conference Proceedings **2709**, 020006 (2022).

[226] A. Kraft, C. Wolf, J. Bartsch, M. Glatthaar, and S. Glunz, *Long term stability of copper front side contacts for crystalline silicon solar cells,* Solar Energy Materials and Solar Cells **136**, 25 (2015).

[227] V. D. Mihailetchi, H. Chu, J. Lossen, and R. Kopecek, *Surface passivation of boron-diffused junctions by a borosilicate glass and in situ grown silicon dioxide interface layer,* IEEE Journal of Photovoltaics **8**, 435 (2018).

[228] T. Meßmer, F. Demiralp, and A. Halm, *Low cost semi automated assembly unit for small size back contact modules and low cost interconnection approach,* Energy Procedia **98**, 98 (2016).

[229] IEC, *Crystalline silicon terrestrial photovoltaic (pv) modules: design qualification and type approval,* (2021).

[230] J. Tang, C. H. H. Mak, S. K. Tam, and K. M. Ng, *Formulation of a paste for copper thick film,* Journal of Nanoparticle Research **23** (2021).

[231] B. H. Teo, A. Khanna, V. Shanmugam, M. L. O. Aguilar, M. E. Delos Santos, D. J. W. Chua, W.-C. Chang, and T. Mueller, *Development of nanoparticle copper screen printing pastes for silicon heterojunction solar cells,* Solar Energy **189**, 179 (2019).

[232] C. R. Osterwald and T. J. McMahon, *History of accelerated and qualification testing of terrestrial photovoltaic modules: A literature review,* Progress in Photovoltaics: Research and Applications **17**, 11 (2009).

[233] J. Bartsch, A. Mondon, K. Bayer, C. Schetter, M. Hörteis, and S. Glunz, *Quick determination of copper-metallization long-term impact on silicon solar cells,* Journal of the electrochemical Society **157**, H942 (2010).

[234] N. Núñez, J. R. González, M. Vázquez, C. Algora, and P. Espinet, *Evaluation of the reliability of high concentrator gaas solar cells by means of temperature accelerated aging tests,* Progress in Photovoltaics: Research and Applications **21**, 1104 (2013).

[235] R. van Leest, G. Bauhuis, P. Mulder, R. van der Heijden, E. Bongers, E. Vlieg, and J. Schermer, *Effects of copper diffusion in gallium arsenide solar cells for space applications,* Solar Energy Materials and Solar Cells **140**, 45 (2015).

[236] ECSS, *Ecss-e-st-20-08c rev.1 – photovoltaic assemblies and components,* (2012).

[237] A. Kraft, C. Wolf, J. Bartsch, and M. Glatthaar, *Characterization of copper diffusion in silicon solar cells,* Energy Procedia **67**, 93 (2015).

[238] A. Ebong, S. Huneycutt, S. Grempels, K. Ankireddy, R. Dharmadasa, and T. Druffel, *Progress of atmospheric screen-printable cu paste for high efficiency perc solar cells,* in *2021 IEEE 48th Photovoltaic Specialists Conference (PVSC)* (2021) pp. 1417–1420.

[239] G. Cimiotti, J. Bartsch, A. Kraft, A. Mondon, and M. Glatthaar, *Design rules for solar cells with plated metallization,* Energy Procedia **67**, 84 (2015).

Acknowledgements

Starting a PhD after 11 years of working was one of the most memorable experiences of my life. It would not have been possible for me to complete my PhD without the help and support of many people. I would like to express my sincere gratitude to:

Prof. Dr. Olindo Isabella, and Prof. Dr. Miro Zeman for accepting my PhD application and being my promoters. I appreciate the supervision you provided, as well as your prompt responses to my questions. Also, I have gained a great deal of knowledge through the well-established online courses, summer school, and other courses. As a result of your efforts, the ESE department and PVMD group are leading on both research and education in the sustainable energy field, and I am proud to be a member of these teams.

Dr. Valentin D. Mihailetchi, for being my daily supervisor. Also, I would like to thank you for your advice and assistance in everyday life. Your deep understanding of both science and engineering in the photovoltaic area impressed me a lot, and you are an excellent role model for my future career.

Dr. Radovan Kopecek for providing me with the job, and help finding my PhD host university. You are a light guide to me with your working passion and vision.

The late Dr. Eckard Wefringhaus for his assistance at the beginning of my PhD, as well as for handling my PhD contract. We had such a pleasant time working with you, and were so sad when you passed away. The pleasant summer of 2019 left me with a lasting memory of your wisdom, perseverance and humor.

Thomas Buck for helping me and my family when we moved to Konstanz. I also appreciate the discussion on metallization you provided.

Dr. Florian Buchholz and Dr. Daniel Tune for supervising the experiments under HighLite project.

ZEBRA and n-type team: Dr. CHU Haifeng, Christoph Peter, Dr. Razvan Roescu, Mertcan Comak, Stephan Eisert, Lejo Joseph Koduvelikulathu, Vaibhav Venkat Kuruganti, Dr. Joris Libal, Jan Lossen, Rafael Marczak, and Dominik Rudolph, for the help with cell processing and characterization. It was also an unforgettable experience to work with you on the technology transfer project.

Andreas Halm and Prof. Dr. Andreas Schneider, for the discussion and meetings on module processing.

Colleagues from module team: Maria Ignacia Devoto Acevedo, Rüdiger Farneda, Tobias Meßmer, Dr. Tudor Lucian Timofte, Karl Wienands, for the help with module processing, and answering my questions on modules.

Admin team of ISC: Petra Hoffmann, Sabine Deck, Katja Gaffry, for helping with not only the admin affairs, but also personal suggestions.

My former SERIS colleagues, Dr. WANG Yan, and Dr. LUO Wei, for their suggestions on my PhD topics.

My parents and grandparents for their love, support, and encouragement over the past few years. We know the love of parents until we become parents ourselves (in Chinese: 养儿方知父母恩).

My wife GUO Na, for the love and companionship. Moving and living in different countries is no easy, and I consider myself fortunate to have you by my side throughout every step of my life's journey.

My daughter Youran for the joy you bring to baba and mama.

Finally, I would like to thank Valentin for proofreading this thesis, and Sebastian Veerman for translating the summary into Dutch.

Curriculum Vitæ

Ning Chen was born on April 22, 1985, in Yulin (Shaanxi), China. He obtained his Bachelor's degree from Xi'an Jiaotong University, China, and his Master's degree from Shanghai Jiao Tong University, China. Since 2008, Ning Chen has been working in the field of solar cell and module technologies research, and has gained experience working for various companies such as Solarfun Power Holdings Co. (now part of Hanwha Q CELLS Co., Ltd), RENA GmbH, Optitune International Pte. Ltd., etc.

Prior to pursuing his PhD, he worked as a researcher at the Solar Energy Research Institute of Singapore (SERIS), National University of Singapore. In 2019, he began his PhD program at TU Delft and ISC Konstanz, with Prof. Olindo Isabella and Prof. Miro Zeman as his promoters and Dr. Valentin D. Mihailetchi as his daily supervisor. His research interest lies in industrial high-efficiency solar cells and module technologies.

Ning Chen has extensive experience working on industrial production lines, as well as numerous public and industry-funded projects. He has a proven track record of successfully transferring innovative technology from lab to fab.

List of Publications

Peer-reviewed journal articles

1. **N. Chen**, F. Buchholz, D. D. Tune, O. Isabella, and V. D. Mihailetchi, *Mitigating Cut Losses in Interdigitated Back Contact Solar Cells*, IEEE Journal of Photovoltaics, 12(6), (2022). **(Chapter 4)**

2. **N. Chen**, D. D. Tune, F. Buchholz, R. Roescu, M. Zeman, O. Isabella, and V. D. Mihailetchi, *Stable Passivation of Cut Edges in Encapsulated n-type Silicon Solar Cells Using Nafion Polymer*, Solar Energy Materials and Solar Cells, 258, (2023). **(Chapter 5)**

3. **N. Chen**, D. Rudolph, C. Peter, M. Zeman, O. Isabella, Y. Rosen, M. Grouchko, O. Shochet, and V. D. Mihailetchi, *Thermal Stable High Efficiency Copper Screen Printed Back Contact Solar Cells*, Solar RRL, 7(2), (2023). **(Chapter 6)**

4. X. Yan, **N. Chen**, F. B. Suhaimi, X. Zhang, Q. Wang, H. Jin, V. Shanmugam, and S. Duttagupta, *Development of High Efficiency nFAB PERL Solar Cells Using APCVD PSG and Laser Processing*, physica status solidi (a), 217(11), (2020).

5. J. Gao, X. Qu, Y. Guo, X. Wu, **N. Chen**, X. Feng, B. Zhang, T. Zhang, and H. Liu, *Over 700 mV IBC Solar Cell by Optimizing Front Surface Field Passivation*, IEEE Journal of Photovoltaics, 13(1), (2023).

6. R. Kopecek, F. Buchholz, V. D. Mihailetchi, J. Libal, J. Lossen, **N. Chen**, H. Chu, C. Peter,T. Timofte, A. Halm, Y. Guo, X. Qu, X. Wu, J.Gao and P. Dong, *Interdigitated Back Contact Technology as Final Evolution for Industrial Crystalline Single-Junction Silicon Solar Cell*, Solar, 3(1), (2023).

7. L. Tous, J. Govaert, S. Harrison, C. Carrière, V. Barth, V. Giglia, F. Buchholz, **N. Chen**, A. Halm, et al., *Overview of Key Results Achieved in H2020 HighLite Project Helping to Raise the EU PV Industries' Competitiveness*, Progress in Photovoltaics: Research and Applications, (2023).

Contribution to conferences and workshops

1. **N. Chen**, D. D. Tune, F. Buchholz, A. Halm, and V. D. Mihailetchi, *Impact of Cut Edge Recombination in High Efficiency Solar Cells – Measurement and Mitigation Strategies*, in 38th European Photovoltaic Solar Energy Conference and Exhibition, online, (2021).

2. **N. Chen**, D. Rudolph, C. Peter, H. Chu, T. Buck, and V. D. Mihailetchi, *Screen Printed Copper Paste for Metallization of IBC Solar Cells*, in SiliconPV 2022, Konstanz, (2022).

3. **N. Chen**, F. Buchholz, D. D. Tune, A. Halm, O. Isabella, and V. D. Mihailetchi, *Reducing Cut Losses of Interdigitated Back Contact Solar Cells*, in WCPEC-8, Milan, (2022).

4. **N. Chen**, D. Rudolph, J. Lossen, C. Peter1, F. Buchholz, V. D. Mihailetchi, A. Halm, I. Rosen, *Screen printed Cu-pastes for high efficient backcontact silicon solar cells*, in 8th Solar Cell Paste and Metallization Forum (China), Changzhou, (2022).

5. V. D. Mihailetchi, **N. Chen**, C. Peter, F. Buchholz, J. Eickelmann, R. Roescu, T. Timofte, J. Libal, A. Halm, R. Kopecek , *Bifacial IBC technology: How will it evolve?*, in 2022 Ankara bifiPV Workshop, Ankara, (2022).

6. M. Grimm, **N. Chen**, S. Harrison, L. Tous, *Advanced Laser Cutting Equipment for n-Type Cells*, in nPV workshop 2022, Konstanz, (2022).

7. J. Lossen, D. Rudolph, **N. Chen**, F. Buchholz, A. Halm, and I. Rosen, *Screen printed Cu-pastes for high efficient backcontact silicon solar cells*, in Printed, Hybrid, InMold, and 3D Electronics, online, (2022).

8. D. Rudolph, R. Farneda, T. Timofte, A. Halm, **N. Chen**, J. Libal, F. Buchholz, I. Rosen, M. Grouchko, and O. Shochet, *Screen printable, non-fire-through copper paste applied as busbar metallization for back contact solar cells*, AIP Conference Proceedings 2709, 020006 (2022), in Metallization & Interconnection Workshop (2021).

9. X. Qu, X. Wu, Y. Guo, L. Miao, Z. Song, J. Lossen, V. D. Mihailetchi, J. Libal, H. Chu, **N. Chen**, C. Peter, F. Buchholz, and R. Kopecek, *IBC production at SPIC*, in 10th Workshop on Back Contact Solar Cell and Module Technology, Konstanz, (2022).

10. R. Kopecek, J. Libal, F. Buchholz, J. Lossen, V. D. Mihailetchi, D. Rudolph, H. Chu, **N. Chen**, C. Peter, T. Timofte, A. Halm, J. Liu, Y. Guo, X. Qu, X. Wu, J. Gao, P. Dong, *24% Efficient Interdigitated Back Contact Solar Cells in Mass Production without Passivating Contacts*, WCPEC-8, Milan, (2022).

Selected publications prior to the PhD study

1. **N. Chen**, E. C. Wang, X. Yan, V. Shanmugam, B. Nagarajan, L. Zhang, X. Gong, X. Zhang, Q. Wang, H. Jin, and S. Duttagupta., *Development of Bifacial N-Type Front-and-Back Contact Cells with Phosphorus Back Surface Field via Mask-Free Approaches*, physica status solidi (a), 216(22), (2019).

2. W. Luo, **N. Chen**, C. Ke, Y. Wang, A. G. Aberle, S. Ramakrishna, S. Duttagupta, and Y. S. Khoo, *Investigation of Polysilicon Passivated Contact's Resilience to Potential-Induced Degradation*, Solar Energy Materials and Solar Cells, 195, (2019).

3. X. Yan, **N. Chen**, F. B. Suhaimi, L. Zhang, X. Gong, X. Zhang, and S. Duttagupta, *Design, Fabrication, and Analysis of Double-Layer Antireflection Coatings (ARC) for Industrial Bifacial n-Type Crystalline Silicon Solar Cells*, Applied Optics, 58(15), (2020).

4. V. Shanmugam, **N. Chen**, X. Yan, A. Khanna, B. Nagarajan, J. Rodriguez, N. Nandakumar, H. Knauss, H. Haverkamp, A. G. Aberle, and S. Duttagupta., *Impact of the Manufacturing Process on the Reverse-Bias Characteristics of High-Efficiency n-Type Bifacial Silicon Wafer Solar Cells*, Solar Energy Materials and Solar Cells, 191, (2018).

5. J. Rodriguez, E. C. Wang, **N. Chen**, J. W. Ho, M. Li, J. K. Buatis, B. Nagarajan, L. Xu, W. L. Choy, V. Shanmugam, J. Wong, A. G. Aberle, and S. Duttagupta, *Towards 22% Efficient Screen-Printed Bifacial n-Type Silicon Solar Cells*, Solar Energy Materials and Solar Cells, 187, (2018).